

# **Gamma-Ray Emission from Neutron Stars and the Deutsch Field Pulsar**

by

**Mark Higgins**

**A thesis submitted to the Department of Physics  
in conformity with the requirements for  
the degree of Doctor of Philosophy**

**Queen's University  
Kingston, Ontario, Canada  
August 19, 1996**

**copyright ©Mark Higgins, 1996**



National Library  
of Canada

Acquisitions and  
Bibliographic Services

395 Wellington Street  
Ottawa ON K1A 0N4  
Canada

Bibliothèque nationale  
du Canada

Acquisitions et  
services bibliographiques

395, rue Wellington  
Ottawa ON K1A 0N4  
Canada

*Your file Votre référence*

*Our file Notre référence*

**The author has granted a non-exclusive licence allowing the National Library of Canada to reproduce, loan, distribute or sell copies of his/her thesis by any means and in any form or format, making this thesis available to interested persons.**

**The author retains ownership of the copyright in his/her thesis. Neither the thesis nor substantial extracts from it may be printed or otherwise reproduced with the author's permission.**

**L'auteur a accordé une licence non exclusive permettant à la Bibliothèque nationale du Canada de reproduire, prêter, distribuer ou vendre des copies de sa thèse de quelque manière et sous quelque forme que ce soit pour mettre des exemplaires de cette thèse à la disposition des personnes intéressées.**

**L'auteur conserve la propriété du droit d'auteur qui protège sa thèse. Ni la thèse ni des extraits substantiels de celle-ci ne doivent être imprimés ou autrement reproduits sans son autorisation.**

0-612-20564-9


QUEEN'S UNIVERSITY AT KINGSTON  
SCHOOL OF GRADUATE STUDIES AND RESEARCH  
PERMISSION OF CO-AUTHOR(S)

I/we, the undersigned, hereby grant permission to microfilm any material designated as being co-authored by me/us in the thesis copyrighted to the person named below:

MARK HIGGINS  
Name of Copyrighted Author

  
Signature of copyrighted author

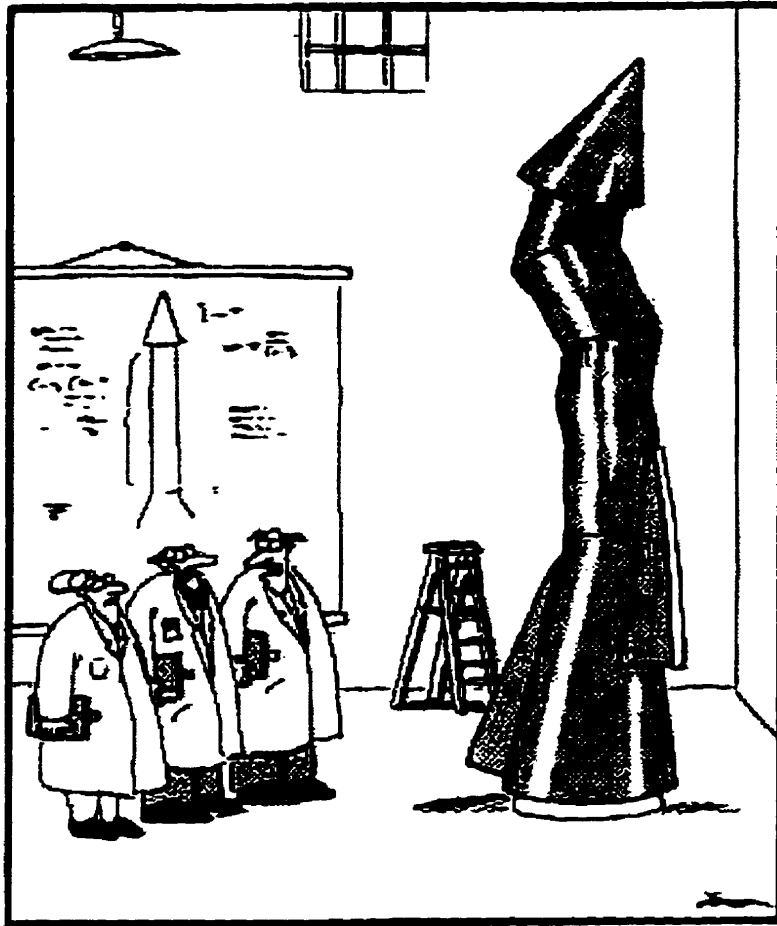
Name(s) of co-author(s)  
R.N. Henriksen

Signature(s) of co-author(s)  


\_\_\_\_\_  
\_\_\_\_\_  
\_\_\_\_\_

\_\_\_\_\_  
\_\_\_\_\_  
\_\_\_\_\_

DATE: Feb 10/97



**"It's time we face reality, my friends. ...  
We're not exactly rocket scientists."**



## *Abstract*

Gamma-ray emission from neutron stars is considered in two contexts. A new model for gamma-radiation from pulsars is presented which uses the Deutsch fields to model the electromagnetic fields around the star; the structure of and charge motion in these fields is discussed in detail. A widely applicable approximation to charged particle motion in powerful electromagnetic fields is developed and exploited in the numerical simulation of particle motion in our model.

An exploration of the distribution of gamma-ray bursts is also presented, assuming that these objects are the result of interactions between neutron stars located in an extended Galactic halo and stray comets ejected from stellar systems in globular clusters and disk stars.

### *Statement of co-authorship*

The work presented here is the work of the author in conjunction with the supervising professor Dr. R.N. Henriksen.

## *Acknowledgments*

I'd like to thank Dr. Henriksen for his faith and assistance over the last four years, and the other folks around the office for helping me blow off steam when I needed it.

I also want to thank Natasha Hilfer for always keeping life interesting (even in those times when I was content to be a little less interested).

# CONTENTS

Abstract . . . . .	i
Statement of co-authorship . . . . .	ii
Acknowledgments . . . . .	iii
List of Figures . . . . .	ix
1. <i>Introduction</i> . . . . .	1
1.1 The Pulsar Environment . . . . .	2
1.1.1 Periods . . . . .	3
1.1.2 Magnetic Field . . . . .	5
1.1.3 The Characteristic Age . . . . .	6
1.1.4 The Goldreich-Julian Charge Density . . . . .	8
1.2 The Pulsar Problem . . . . .	8
1.3 Gamma-Ray Bursts . . . . .	10
1.3.1 Galactic Models . . . . .	11
1.3.2 Cosmological Models . . . . .	12
1.3.3 Solar Models . . . . .	12
1.3.4 Basic Observational Features . . . . .	12
2. <i>Gamma-Ray Burst Observations</i> . . . . .	14
2.1 Burst Timescales and Light Curves . . . . .	14
2.2 Isotropy . . . . .	17
2.2.1 Dipole and Quadropole Moments . . . . .	17
2.2.2 The Angular Autocovariance Function . . . . .	23
2.3 Distribution in Flux . . . . .	25
2.4 Counterparts at Other Frequencies . . . . .	28
2.4.1 Quiescent Counterparts . . . . .	29
2.4.2 Bursting Counterparts . . . . .	32
2.5 Line Features in GRBs . . . . .	33
3. <i>Pulsar Observations</i> . . . . .	36
3.1 Basic Observational Characteristics . . . . .	36
3.2 Radio Emission . . . . .	37
3.3 The Gamma-Ray Pulsars . . . . .	38
3.3.1 Gamma-Ray Light Curves . . . . .	39
3.3.2 Gamma-Ray Spectra . . . . .	43
3.3.3 Gamma-Ray Power Output and Efficiency . . . . .	44

4.	<i>Neutron Star-Comet Gamma-Ray Burst Models</i>	48
4.1	A Galactic Origin for GRBs	48
4.1.1	Matching the Distribution on the Sky	49
4.1.2	Factors in Favour of a Neutron Star Origin	52
4.2	Comet-Neutron Star Models	56
5.	<i>Existing Models of Pulsar Gamma-Ray Emission</i>	58
5.1	Radiation Processes in Ultra-High Fields	58
5.1.1	Synchrotron Radiation	58
5.1.2	Curvature Radiation	60
5.1.3	Inverse-Compton Radiation	61
5.2	Scattering in Pulsar Magnetospheres	64
5.2.1	$\gamma$ -B Pair Creation	64
5.2.2	$\gamma$ - $\gamma$ Pair Creation	65
5.2.3	Photon Splitting	65
5.2.4	Triplet Pair Production	66
5.3	Pulsar Gamma-Radiation Models	66
5.3.1	Vacuum Birefringence as a Model Test	67
5.3.2	Polar Cap Models	68
5.3.3	Outer Gap Models	71
6.	<i>Distribution of Gamma-Ray Bursts in Halo Neutron Star-Comet Models</i>	75
6.1	Introduction	75
6.2	The Model of Galactic Potential	75
6.3	The Three Populations	76
6.4	Estimating the Interaction Probability	80
6.5	Simulated Gamma-Ray Burst Distribution	82
6.6	Conclusions	85
7.	<i>The Deutsch Fields</i>	88
7.1	Definition of Vacuum	88
7.2	The Point Dipole Fields	90
7.2.1	Inside the Light Cylinder	90
7.2.2	Outside the Light Cylinder	93
7.2.3	Near the Light Cylinder	94
7.3	The Effect of the Star	94
7.4	Null Surfaces	96
7.4.1	Wired Null Surfaces	97
7.4.2	Pierced Null Surfaces	97
7.4.3	Null Surface Structure in the Deutsch Fields	98
7.5	Symmetries in the Deutsch Fields	98

8.	<i>The Dynamics of Charges in the Deutsch Fields</i>	101
8.1	The Radiation Reaction Force	101
8.2	Numerical Integration of Charge Motion - the Complete Simulation	103
8.3	The Drift-Frame Bead on a Wire Approximation	105
8.3.1	The Approximation	105
8.3.2	Comparison with the Complete Simulation	108
8.4	Charge Motion on the Null Surface	113
8.4.1	Charge Motion on Wired Surfaces	113
8.4.2	Charge Motion Near a Wired Null Surface	114
8.4.3	Charge Motion on Pierced Surfaces	115
8.5	Types of Charge Motion in the Deutsch Fields	117
8.6	The Inner and Outer Magnetospheres	117
8.7	Charge Energetics	118
9.	<i>The Deutsch Field Pulsar Model</i>	121
9.1	Radiation Processes in the Deutsch Fields	122
9.1.1	Particle-Photon and Photon-Photon Interactions	122
9.1.2	Synchrotron Radiation	125
9.2	Outline of the Model	125
9.3	Light Curve Generation	126
9.4	Light Curve Structure	129
9.5	Total Emitted Power	130
9.5.1	The Required Number Density	130
9.5.2	The Gamma-Ray Efficiency	135
9.5.3	The Distribution in Viewing Angle	137
9.6	Spectra of Emitted Radiation	138
9.7	Aging the Model Pulsar	142
9.7.1	The Total Power	142
9.7.2	The Evolution of the Spectrum	143
9.8	Candidates for Future Searches	146
9.8.1	The INTEGRAL Telescope	149
9.8.2	The GLAST Telescope	149
9.8.3	The CELESTE Telescope	149
9.9	Millisecond Pulsars	149
9.9.1	Gamma-ray Luminosity of Globular Clusters	150
9.10	The Seven Known Gamma-Ray Pulsars	151
9.10.1	PSR1055-52	152
9.10.2	The Geminga Pulsar	152
9.10.3	PSR1951+32	154
9.10.4	PSR1706-44	154
9.10.5	The Crab Pulsar	156
9.10.6	The Vela Pulsar	157
9.10.7	PSR1509-58	157

<i>10. Future Work</i> . . . . .	158
10.1 The Source for the Charge . . . . .	158
10.2 Synchrotron Radiation . . . . .	160
10.3 Refinements of the Numerical Modelling . . . . .	161
10.4 Iterating the Solution to a Self-Consistent Magnetosphere . . . . .	161
10.5 Applying the DFB Approximation to Global Modelling . . . . .	162
10.6 The Inner Magnetosphere . . . . .	162
<i>11. Conclusions</i> . . . . .	164
11.1 Distribution of GRBs in Halo Neutron Star-Comet Interactions . . . . .	164
11.2 The Deutsch Field Gamma-Ray Pulsar Model . . . . .	166
<i>A. The Deutsch Fields</i> . . . . .	172
<i>Appendix</i>	172

## LIST OF FIGURES

1.1	Simplified diagram of the pulsar magnetosphere . . . . .	2
1.2	Histogram of normal pulsar periods . . . . .	4
1.3	Histogram of pulsar surface field strengths . . . . .	6
1.4	Histogram of pulsar characteristic ages . . . . .	7
2.1	Distribution of $T_{90}$ in the BATSE 3B catalog . . . . .	15
2.2	Typical GRB light curve . . . . .	16
2.3	Sky map of BATSE 3B catalog of gamma-ray bursts . . . . .	18
2.4	Plot of the angular autocovariance function against angle for the BATSE 3B catalog of sources . . . . .	24
2.5	The integrated distribution of source flux for the BATSE 3B catalog . . . . .	27
3.1	Multi-Frequency Light Curves for Six of the Seven Known Gamma-Ray Pulsars	41
3.2	Light curve above 100 MeV for PSR 1951+32 . . . . .	42
3.3	Spectra for the six pulsars observed by EGRET . . . . .	45
3.4	High energy spectrum for PSR 1509-58 . . . . .	46
3.5	Gamma-ray efficiencies for the known high-energy gamma-ray pulsars versus characteristic age . . . . .	47
4.1	False-colour radio map of the “duck” SNR and PSR 1757-24 . . . . .	51
5.1	Illustration of the inverse Compton scattering process . . . . .	63
5.2	Current structure in the Cheng, Ho, & Ruderman (1988a) outer gap model . . . . .	72
6.1	Ejection velocity distribution of comets from GCs . . . . .	77
6.2	Radial distribution of halo comets after five billion years of integration . . . . .	79
6.3	Radial distribution of neutron stars after five billion years of integration . . . . .	81
6.4	Distributions of simulated GRBs on the sky and in flux . . . . .	83
6.5	Plot of GRBs inside $r_{\max}$ for NSs with a birth velocity of 2000 km/s . . . . .	86
7.1	Magnetic and electric field lines for the point dipole fields when $r \ll R_{\text{lc}}$ . . . . .	91
7.2	Drift velocity on the null surface for the point dipole fields when $r \ll R_{\text{lc}}$ . . . . .	92
7.3	Point dipole field lines near the light cylinder . . . . .	95
7.4	Null surface structure near the star for the orthogonal Deutsch fields . . . . .	99
8.1	Coordinate System for the DFB Approximation Analysis . . . . .	106
8.2	Comparison of the Complete to DFB Simulation Results 1 . . . . .	110
8.3	Comparison of the Complete to DFB Simulation Results 2 . . . . .	111
8.4	Comparison of the Complete to DFB Simulation Results 3 . . . . .	112



9.1	Representative light curves in the Deutsch field gamma-ray pulsar model . . .	127
9.2	Likelihood plot for required number density fit parameters . . . . .	134
9.3	Poloidal distribution of average emitted power for two Vela-like pulsars . . .	136
9.4	Variation of $\Omega_p$ with frequency for a Geminga-like pulsar . . . . .	136
9.5	The curvature spectrum for a single particle in instantaneously circular motion	138
9.6	Representative spectra for three model pulsars . . . . .	139
9.7	The spectra for different parts of the light curve for a model pulsar . . . . .	141
9.8	Evolution of the spectrum of a model pulsar with $\mu = 10^{30}$ G cm <sup>3</sup> . . . . .	144
9.9	Evolution of the spectrum for a model pulsar with $\mu = 10^{31}$ G cm <sup>3</sup> . . . . .	145
9.10	Model spectrum for PSR 0656+14 comparison with the model spectrum for Geminga . . . . .	148
9.11	Time-averaged model spectrum of PSR 1055-52 with the EGRET observations	153
9.12	Time-averaged model spectrum of Geminga with the EGRET observations .	153
9.13	Time-averaged model spectrum of PSR 1951+32 with the EGRET observations	154
9.14	Time-averaged model spectrum of PSR 1706-44 with the EGRET observations	155
9.15	Time-averaged model spectrum of the Crab pulsar with the EGRET observa- tions . . . . .	155
9.16	Time-averaged model spectrum of the Vela pulsar with the EGRET observations	156

## LIST OF TABLES

3.1	Observed parameters for the seven known gamma-ray pulsars . . . . .	39
6.1	Results of the tests for isotropy and homogeneity for simulated GRB distributions . . . . .	84
9.1	Required number densities at the starting sphere for the seven known gamma-ray pulsars . . . . .	132
9.2	The top twenty brightest pulsars as predicted by the Deutsch field gamma-ray pulsar model . . . . .	147

## 1. INTRODUCTION

Though they have been studied for over twenty-five years, pulsars have remained a challenging theoretical problem for astrophysicists. No fully consistent and physically reasonable model of the global properties of the pulsar magnetosphere has been developed, and the basic physics of the emission processes are still uncertain.

The processes which generate the radio emission observed from these objects are generally thought to be distinct from those that produce the x- and gamma-ray emission seen from the very youngest members of the population. Once a global model for the magnetosphere of a pulsar is developed, these two processes should be linked.

Gamma-ray bursts (GRBs) are one of the more mysterious of astrophysical objects. No counterpart at any other frequency has been reliably observed, and the distribution on the sky and in flux is nominally consistent with either a Galactic population of sources located in an enormous halo or objects at cosmological distances.

This thesis deals with gamma-ray emission from neutron stars in two different contexts: a model for the gamma-ray emission from young pulsars and an investigation of the distribution of gamma-ray bursts if these objects are the result of collisions between neutron stars in a Galactic halo and comets.

This work is organised into roughly six sections: this introduction, two chapters on the observational data, another two on present models for gamma-ray bursts and gamma-ray emission from pulsars, a chapter which presents the research on our model of the distribution of gamma-ray bursts, three chapters on our gamma-ray pulsar model, and finally two chapters to discuss futures avenues of research and conclusions.

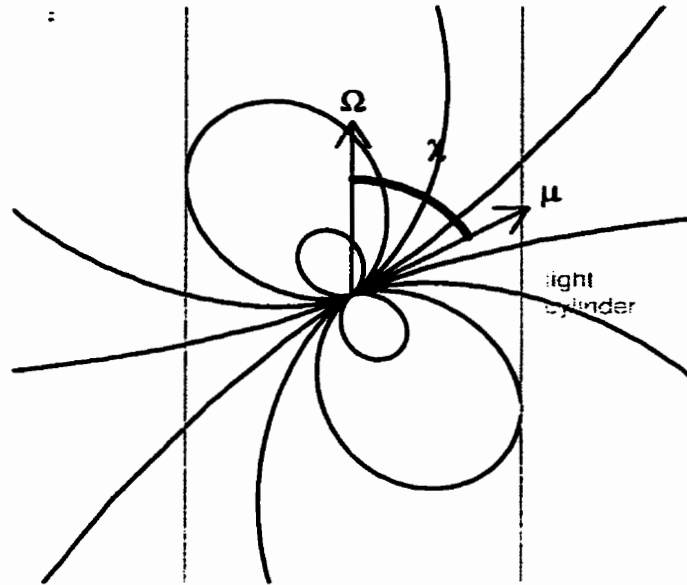


Fig. 1.1: A simplified picture of the space around a pulsar, showing dipole field lines (in black) and the main physical parameters:  $\tilde{\Omega}$ , the angular velocity of the star,  $m\tilde{\mu}$ , the magnetic dipole moment,  $\chi$ , the inclination angle of the dipole moment, and the light cylinder radius, which sets the length scale for the magnetosphere (the radius of the light cylinder  $R_{lc} = c/\Omega$ ).

## 1.1 The Pulsar Environment

Pulsars are widely believed to be highly magnetised and rapidly rotating neutron stars, remnants of supernova explosions. The general population is seen as radio sources, which these objects emit for a relatively short time astrophysically - only ten million years or less - and then become “dark matter” (though not a significant contribution to the total Galactic mass). The very youngest of these stars, only seven known to date, all younger than a few hundred thousand years, also emit in gamma-rays and occasionally in x-rays.

Figure 1.1 shows a typical simplified picture of the space around a pulsar and the magnetic field lines (shown in black). Here, the pulsar is a point at  $r = 0$ , and the magnetic field is a dipole determined by the magnetic dipole moment  $\tilde{\mu}$ . The rotational frequency of the star is

$\vec{\Omega}$  (shown vertical in this plot), and the angle between  $\vec{\Omega}$  and  $\vec{\mu}$  is labelled  $\chi$ , the inclination angle.  $\Omega$  sets the length scale for the pulsar magnetosphere, called the light cylinder radius  $R_{lc} = c/\Omega$ . Field lines which close inside the magnetosphere are called “closed” field lines, and those which close outside are generally called “open”. This simple picture ignores the effects of current or light travel time effects on the field structure.

The observable parameters of these stars are relatively few. The period of stellar rotation can be calculated with extraordinary accuracy, and for almost all the known pulsars, is found to be slowly decreasing with time; this period time derivative is another fundamental observable of the pulsar. Second derivatives of the period, as well as occasionally third derivatives, have been measured for some pulsars, and further constrain the basic physics (Taylor, Manchester, & Lyne 1993).

There are two broad categories of pulsars observed: the very short period millisecond pulsars, which typically have surface magnetic field strengths on the order of  $10^9$  G, and the longer-period normal population of pulsars, which have much stronger surface fields, on the order of  $10^{12-13}$  G.

A third category of pulsar which is quite different than the radio pulsars is that of the x-ray pulsars. These objects are neutron stars in close binaries which accrete matter from their companion star; the accreting matter is heating to x-ray temperatures, and an x-ray pulse is emitted. As they are quite different physically from the radio pulsars, there will be little discussion of this sort of pulsar in this thesis.

### 1.1.1 Periods

Pulsars are extremely accurate clocks due to the regular nature of their pulsation. An integrated light curve (averaged over a few thousand periods) remains constant in shape over long periods of time in most cases, making period determination particularly accessible.

Figure 1.2 shows a histogram of pulsar period for the known normal pulsars. The average period is approximately half a second, with no pulsars currently observed with periods longer



Fig. 1.2: A histogram of the periods of the normal population of pulsars (excluding the millisecond pulsars) for the known pulsars. The distribution shows a peak near 0.5 s. Data were taken from the Princeton pulsar catalog, maintained by J. Taylor.

than 4.3 seconds.

This plot does not show the so-called millisecond pulsars, which form a separate population to the regular pulsars. These objects typically have periods of tens of milliseconds, with the fastest spinning with a period of only 1.6 milliseconds.

The angular velocity of the star  $\Omega = 2\pi/T$  (where  $T$  is the pulsar period) defines a characteristic length scale for the physics around the pulsar, called the light cylinder radius:

$$R_{lc} = \frac{c}{\Omega} \tag{1.1}$$

Any object corotating with the star would be moving at the speed of light on the light cylinder. This length scale roughly sets the size of the magnetosphere around the pulsar.

A common feature of most pulsars, including the millisecond pulsars, is a gradual increase of the period with time. This period derivative is another important observable of the object which constrains the physics.

### 1.1.2 Magnetic Field

The normal population of pulsars have magnetic fields among the highest known in the universe. As the progenitor star collapses, magnetic flux is conserved, and the flux density scales like the square of the stellar radius. The field amplification can be a factor of  $10^{10}$  or  $10^{11}$ , converting the gauss-scale stellar fields to gargantuan proportions. Thermal effects in the young neutron star can increase the field even further (Geppert & Wiebicke 1991). The electromagnetic forces are large enough to entirely dominate the dynamics of charges in the space around the star, labelled the **magnetosphere** to emphasize this fact.

The evidence for fields on the order of  $10^{12-13}$  G is fairly unambiguous now. The primary, though indirect, indicator is the pulsar slowdown, which is thought to occur by long-wavelength magnetodipole radiation - a spinning dipole radiates away electromagnetic energy in the form of a spherical, outgoing electromagnetic wave with frequency equal to the rotation frequency. The energy lost through this process is dependent on the strength of the star's magnetic dipole moment and its rotation speed; therefore, knowledge of the period and its derivative can be used to estimate the magnetic fields. For a point dipole field, the relationship between the surface field, period, and period derivative is (see section 7.2.2 for a derivation):

$$B_s \simeq 2 \times 10^{12} \text{G} \left( \frac{P\dot{P}}{5 \times 10^{-15} \text{s}} \right)^{1/2} \quad (1.2)$$

A more direct indication of these strong magnetic fields is found through the presence of cyclotron absorption lines in x-ray pulsar spectra (e.g., Clark *et al* 1990), which is consistent with field strengths of this magnitude. X-ray pulsars are neutron stars accreting matter from a companion star in a binary, but presumably are similar to neutron stars which act as regular radio pulsars.

Figure 1.3 shows a histogram of surface magnetic field strengths inferred from equation 1.2 for the known normal pulsars. The two populations can be seen in the large peak near  $10^{12}$  G and the smaller peak near  $10^{8.5}$  G comprising the millisecond pulsars.

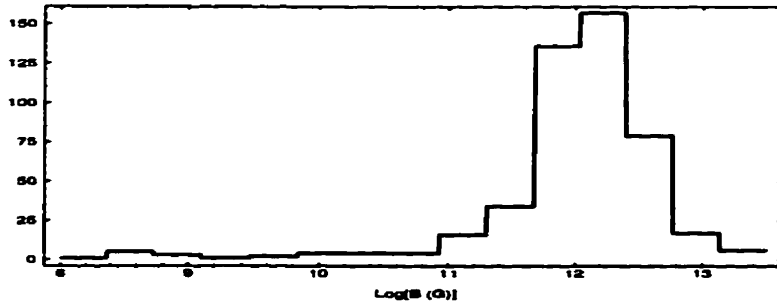


Fig. 1.3: A histogram of the surface fields of both populations of pulsars (normal and millisecond pulsars) for the known pulsars. The distribution shows two peaks: a large one near  $10^{12}$  G representing the normal population of pulsars, and a smaller one near  $10^{8.5}$  G comprising the millisecond pulsars. Data were taken from the Princeton pulsar catalog, maintained by J. Taylor.

This sort of analysis was the first evidence that two distinct populations of pulsars exist. The so-called millisecond pulsars, while spinning extremely rapidly, have surface fields several orders of magnitude lower than the regular population of pulsars. These objects are likely the result of binary interactions, where material accreted onto an old neutron star spins it up to high angular velocity.

### 1.1.3 The Characteristic Age

If a pulsar loses the majority of its angular momentum through magneto-dipole radiation, then its angular velocity obeys a particularly simple differential equation:

$$\dot{\Omega} = -k\Omega^3 \tag{1.3}$$

where  $\Omega$  is the star's angular velocity and  $k$  is a constant which depends on the surface magnetic field and the stellar moment of inertia. This solves to



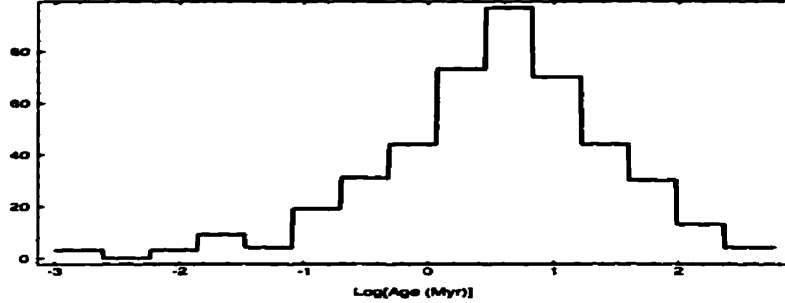


Fig. 1.4: A histogram of the characteristic ages of the known normal pulsars. The distribution shows a peak near five million years, and a smaller one near a thousand years (which is due to these very young pulsars being exceptionally bright). Data were taken from the Princeton pulsar catalog, maintained by J. Taylor.

$$k\tau = \frac{\Omega^{-2} - \Omega_0^{-2}}{2} \quad (1.4)$$

where  $\tau$  is the pulsar age. For long times (when  $\Omega$  is much less than its initial value  $\Omega_0$ ), and substituting for  $k$  in terms of  $\Omega$  and  $\dot{\Omega}$ , the age of the star can be estimated as:

$$\tau = -\frac{\Omega}{2\dot{\Omega}} = \frac{P}{2\dot{P}} \quad (1.5)$$

This time is known as the **characteristic age**, and agrees to at least order-of-magnitude accuracy with other estimates of the pulsar age.

Figure 1.4 shows a histogram of the characteristic ages of the regular population of pulsars. The millisecond pulsars are not included, since this simple model does not apply.

Pulsar ages run from approximately one thousand years for the Crab pulsar to approximately ten million years for the oldest of the population. This is somewhat striking, as it means that pulsars are very young objects in an astronomical sense. A neutron star spends only a small fraction of its life as a visible pulsar.

### 1.1.4 The Goldreich-Julian Charge Density

Very early on in the work on pulsars, Goldreich & Julian (1969) showed that the space around a star would almost certainly be filled with charge, since the electromagnetic forces on a charge near the stellar surface are so much larger than the gravitational force, and non-zero at the stellar surface. The charges would adjust themselves as to short out the component of electric field parallel to the magnetic field line everywhere in space, but forcing the magnetosphere to co-rotate due to the need to match boundary conditions at the stellar surface (this obviously must break down at some point inside the light cylinder, beyond which a corotating charge would be moving faster than light) - a tangential component of the electric field is required to match the boundary condition at the surface of the star. This implies a charge density everywhere in the space around the star of

$$\rho_{\text{GJ}} \simeq \frac{\vec{\Omega} \cdot \vec{B}}{2\pi c} \quad (1.6)$$

where  $\vec{B}$  is the magnetic field at the point in question (see section 7.1 for a derivation).

If the charge density in the space around the star is everywhere much less than the Goldreich-Julian charge density, the electromagnetic fields are not affected significantly. This defines “vacuum” around the star. Therefore, if the charge number density is much less than the Goldreich-Julian number density, the fields will be well-described by vacuum fields. The Goldreich-Julian number density (equal to  $\rho_{\text{GJ}}/e$ ) is approximately

$$n_{\text{GJ}} \simeq 4 \times 10^4 \text{cm}^{-3} \left( \frac{\mu}{10^{30} \text{Gcm}^3} \right) \left( \frac{\Omega}{100 \text{rad/s}} \right)^4 \left( \frac{R_{\text{lc}}}{r} \right)^3 \quad (1.7)$$

## 1.2 The Pulsar Problem

The most serious problem in modelling any sort of pulsar electromagnetic radiation is the lack of a consistent and physical global model for the electromagnetic fields and charged particle currents and densities. Theoretical efforts have concentrated on relatively unphysical toy

models, or have focussed on particular regions in the magnetosphere, assuming properties for the global system. This is not, of course, due to a dearth of effort, but the result of the complexity of the physical system.

Any global solution must take many factors into account to generate a physically reasonable model, all of which affect each other in complex ways. The equations governing the problem are Maxwell's equations (in CGS units, as used throughout this thesis):

$$\vec{\nabla} \cdot \vec{E} = 4\pi\rho \quad \vec{\nabla} \cdot \vec{B} = 0 \quad (1.8)$$

$$\vec{\nabla} \times \vec{E} = -\frac{1}{c} \frac{\partial \vec{B}}{\partial t} \quad \vec{\nabla} \times \vec{B} = \frac{4\pi}{c} \vec{J} + \frac{1}{c} \frac{\partial \vec{E}}{\partial t} \quad (1.9)$$

and the Vlasov equation for the phase-space distribution of charges:

$$\frac{\partial f_i}{\partial t} + \vec{\nabla} f_i \cdot \vec{v}_i + \vec{\nabla}_p f_i \cdot \vec{F}_i = \dot{f}_{in-i} \quad (1.10)$$

where the force on species  $i$  is given by

$$\vec{F}_i = q_i(\vec{E} + \vec{v}_i \times \vec{B}) + \vec{F}_{rad-i} \quad (1.11)$$

and  $\dot{f}_{in-i}$  is a term representing an increase in the charge density due to pair creation; this will be discussed in more detail in section 5.2. There are several important pair creation processes which depend non-linearly on charge and photon energies.

The distribution function of the photons must also be considered, as the interaction between the fields and the matter is important for pair creation processes. This obeys

$$\frac{\partial f_\gamma}{\partial t} + \vec{\nabla} f_\gamma \cdot \vec{v}_\gamma = \dot{f}_{in-\gamma} - \dot{f}_{out-\gamma} \quad (1.12)$$

where  $|v_\gamma| = c$ ,  $\dot{f}_{in-\gamma}$  is a term describing the photon creation from the various sources of radiation, and  $\dot{f}_{out-\gamma}$  represents the loss due to pair creation.

These equations must all be solved self-consistently to satisfy the criteria for a global model. Even these equations involve a number of simplifying assumptions; the plasma is

assumed to be cold (i.e., zero pressure), and the effects of general relativity have been ignored. Special relativity, of course, is considered: the charges are generally moving very close to the speed of light.

The boundary conditions at the star must be included to generate a solution, and are also non-trivial. The binding energy of charges to the surface of the star is unknown due to uncertainties in the properties of atoms in powerful gravitational and electromagnetic fields. However, assuming that the star is a perfect conductor, and that the electric fields inside the star are therefore “frozen-in”, is a very good approximation, allowing a precise determination of the boundary condition for the fields.

A discussion of the array of models developed to approximate this physical system is beyond the scope of this thesis, but suffice it to say that the problem is still far from solved. Numerical techniques and computing power are developing to the point where a fully numerical solution may be conceivable, but this is still impossible at the present.

### *1.3 Gamma-Ray Bursts*

Gamma-ray bursts (GRBs) were first observed by US military satellites which were designed to search for evidence of Soviet nuclear testing in the late 1960s. Fortunately, the military explanation for these objects was ruled out when it was realised that these flashes of gamma-rays originated in space rather than terrestrially.

Presently, about one GRB a day is registered by the BATSE detector aboard the Compton Gamma-Ray Observatory (CGRO). The flash of gamma-rays comes from a random direction, dominating the gamma-ray sky while it happens. They typically last from tens of milliseconds to hundreds of seconds, though there is a fairly wide variety of light curves observed.

The GRBs have been separated into two classes: the “classical” GRBs, which radiate at energies of tens to hundreds of keV and have never reliably been known to repeat, and the soft gamma-ray repeaters (SGRs), which have been observed to repeat and emit mainly in the hard x-ray/soft gamma-ray region of the electromagnetic spectrum.

The SGRs are interesting in that they have been identified fairly conclusively with supernova remnants, suggesting that these objects are related to young, high-velocity neutron stars. However, they are much rarer than the classical GRBs (only three have been observed). There is some suggestion (Fenimore *et al* 1996) that the original SGR, which happened on March 5th, 1979, would actually have been classified as a classical GRB if the photon energies in the initial, rapid burst had been able to be properly analysed (due to deadtime effects and photon pileup, it was only possible to get a valid spectrum very recently). The weak afterglow, which showed an 8-second periodicity, is unique, however; no other classical GRBs show any pulsation or weak, low-energy afterglows.

The work in this thesis will mainly deal with classical GRBs, as our model (chapter 6) examines a possible source for these objects, which are seen to have a different origin than the SGRs.

Though they have been studied for twenty years, there is no widely-accepted explanation for classical GRBs. The models in the literature can be roughly sorted into three categories:

### 1.3.1 Galactic Models

Early efforts almost exclusively identified GRBs with neutron stars in the Galactic disk or Galactic halo, due in large part to the observation of line features in some of the spectra that were readily attributed to radiation physics in the ultra-high magnetic fields associated with pulsars. The first year of data from the BATSE telescope, however, threw these models into question. No line features were seen in any of the spectra, and the bursts were distributed isotropically on the sky, inconsistent with the predictions of a disk or halo population of neutron stars. In fact, after four years of operation, the roughly 1200 observed bursts show no evidence for any anisotropy. To resolve this fact, any neutron star models require a halo with radius of several hundred kpc, larger even than any postulated dark matter halo.

### 1.3.2 *Cosmological Models*

Cosmological models were suggested early on, but gained a wider acceptance with the BATSE data. These models generally involve catastrophic encounters between neutron stars or neutron stars and black holes, though there is a huge number of different models. Paczyński (1986) attempted to unify some of these theories by developing a general model of a gamma-ray burst fireball without analysing the details of the source, and most of the modern predictions use this model or extensions of it. The total energy required in a burst at this distance is huge, on the order of  $10^{52}$  ergs. This is roughly equal to the energy released in a supernova explosion, or the gravitational binding energy of a star.

### 1.3.3 *Solar Models*

These models generally placed the bursts in a shell around the Solar System, most commonly in the Oort cloud of comets. They are generally ruled out, however, since the mechanism for generating gamma-rays (with negligible emission in other parts of the spectrum) is unclear, and the total energy released from a comet would have to be a significant portion of its rest mass energy, which is difficult to justify. It is also difficult to match the distribution in flux (in particular, the observed  $\langle V/V_{\max} \rangle$  statistic - see chapter 2), as was demonstrated by Maoz (1993).

In addition, the Oort cloud of comets cannot be completely spherical, due to tidal disturbances from the Galaxy (Clarke *et al* 1994). If the bursts were from the Oort cloud, this anisotropy would have been detected with the relatively large number of bursts now catalogued.

### 1.3.4 *Basic Observational Features*

The two most commonly-quoted observables of classical GRBs are their isotropy on the sky and their distribution in flux (Briggs *et al* 1996). While isotropically distributed on the sky, their distribution in flux shows an interesting feature. Bursts at large flux (presumably the

closer bursts) follow the  $F^{-3/2}$  distribution of a homogeneously distributed population, but the weaker bursts show less than would be expected. This has been used to suggest an edge to the population radially, or evidence for the curvature of the universe for cosmological sources.

The spectrum of these objects is also important in determining their properties; the classical GRB spectrum is not thermal, which eliminates many simple models for their production (Paczynski's (1986) fireball model predicts a thermal spectrum). The light curves of classical GRBs can be quite varied, and therefore make theoretical modelling somewhat challenging.

## 2. GAMMA-RAY BURST OBSERVATIONS

The literature dedicated to the observations of gamma-ray bursts is enormous. In this thesis, only the data pertinent to the distribution of the bursts in space and flux is presented. The evidence for line features in GRB spectra is presented as it strongly suggests a Galactic neutron star origin for these objects, but spectra, possible repetition of bursts, and other analyses are ignored, as they generally apply to the development of the burst physics rather than the overall distribution of bursts. The model presented in chapter 6 is independent of burst physics, and avoids the question altogether.

This thesis discusses the “classical” GRBs and does not discuss in detail the soft, repeating GRBs which are generally thought to be a separate class of objects. There is some evidence that these SGRs can show classical GRB-like properties; this is discussed in more detail in section 4.1.2.

The BATSE 3B catalog of gamma-ray bursts is the most up-to-date catalog available to the public. It contains 1122 gamma-ray bursts with positions on the sky; 867 of those have with measured flux. The uncertainties on the burst locations are quite large, up to several degrees on the sky, though in some cases interplanetary networks of satellites have been able to place the sources quite accurately.

### *2.1 Burst Timescales and Light Curves*

Times for bursts run over a relatively large range, from tens of milliseconds (or even shorter, as millisecond bursts would be difficult to detect) to hundreds of seconds. The distribution of burst times in the BATSE 3B catalog is shown in figure 2.1; the time shown is  $T_{90}$ , the time during which 90 % of the received counts are recorded. There is some difficulty using



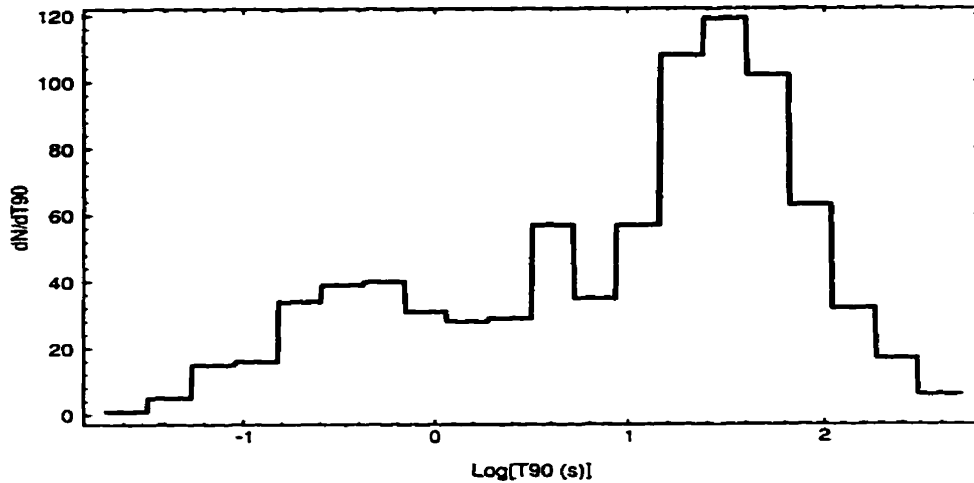


Fig. 2.1: The distribution of  $T_{90}$ , the time during which 90 % of the received counts are recorded, for the BATSE 3B catalog. The distribution shows two peaks, one near 0.5 seconds and the other near 30 seconds.

this standard to determine burst times, as occasionally the light curves show a weak leading or following pulse separated from the bulk of the burst, which, if included in the burst time, would extend it significantly. However, it is something of a representative indicator.

The distribution shows evidence for two peaks, one near 0.5 seconds and the other near 30 seconds. This suggests that there may be two distinct populations of GRBs, although there is no clear evidence of this in the rest of the GRB data.

A typical burst can have a fairly complex light curve; BATSE trigger 1321 is shown in figure 2.2.

There is only one case of a GRB showing pulsation - the March 5, 1979 event had a weak

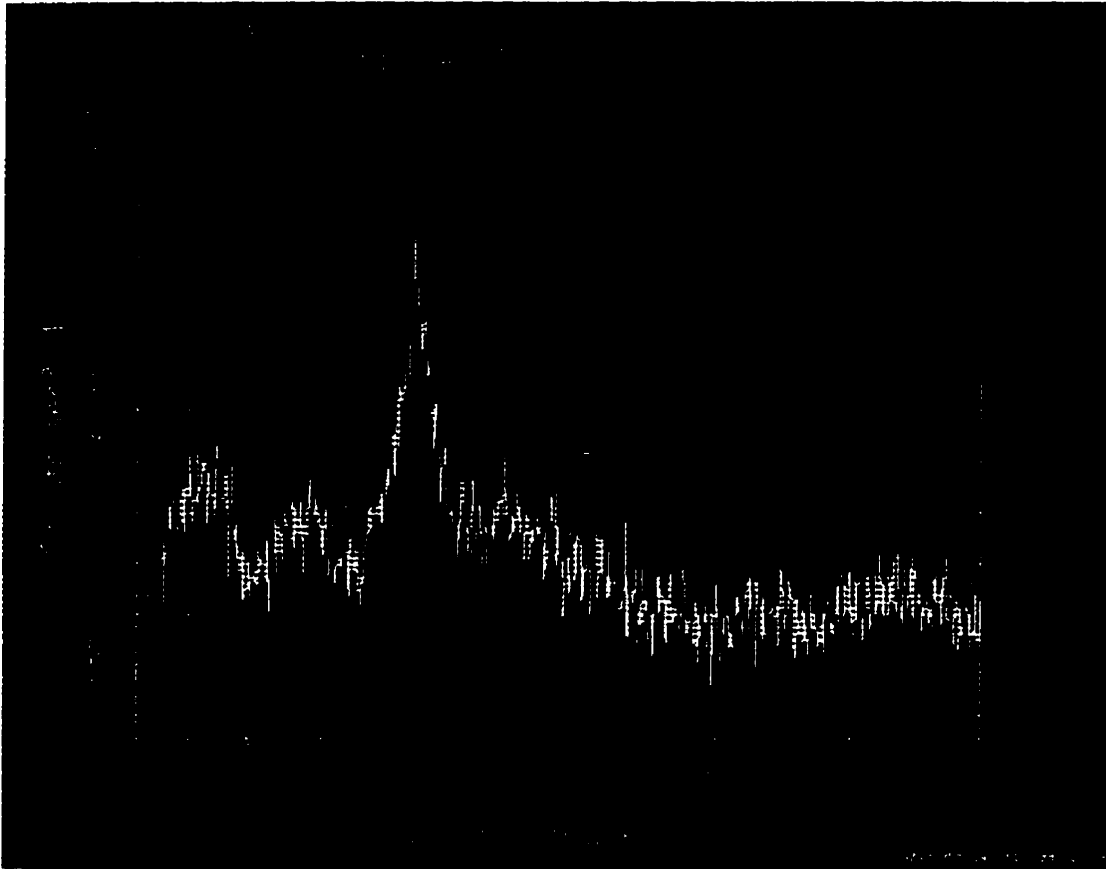


**Fig. 2.2: A typical GRB light curve, BATSE trigger 1321. The light curves can be quite complex.**

( $\simeq 1\%$  level), low-frequency afterglow trailing the main peak with an 8 second periodicity (Barat *et al* 1979). This burst has been classified as a soft gamma-ray burst due to difficulties in estimating the photon energies in the initial, rapid burst, but recent results have suggested that the initial burst looks very similar to a classical GRB in spectral properties. This was a particularly strong burst, and it was initially suspected that all bursts would show such afterglow structure with more sensitive observations. This has not occurred, however, so it seems the March 5 event was somewhat unique.

## 2.2 Isotropy

The sky map of the BATSE 3B catalog bursts is shown in figure 2.3. There is no anisotropy in the data visible to the naked eye, even with over 1100 points. Since the distribution on the sky can be an important clue to the identity of the GRB sources, finding anisotropies in the spatial distribution is particularly important.

### 2.2.1 Dipole and Quadropole Moments

The isotropy of sources on the sky can be investigated using several different statistical techniques. The two most common tests search for evidence of a dipole or quadropole moment to the burst distribution. The statistical methods used in this search are discussed in Briggs (1993), and are summarised here.

Testing for the dipole and quadropole moments of a distribution on the sky are useful for determining a large-scale anisotropy to the distribution, and are relatively insensitive to the reasonably large errors on the BATSE positions. They cannot, however, distinguish small-scale anisotropies which average to isotropy on the large scale (such as grouping of bursts) - this behaviour is best observed by examining the two-point correlation function, discussed later.

There are two quite different types of tests for dipole or quadropole moments: coordinate-system dependent and independent. The first is more efficient at detecting anisotropies

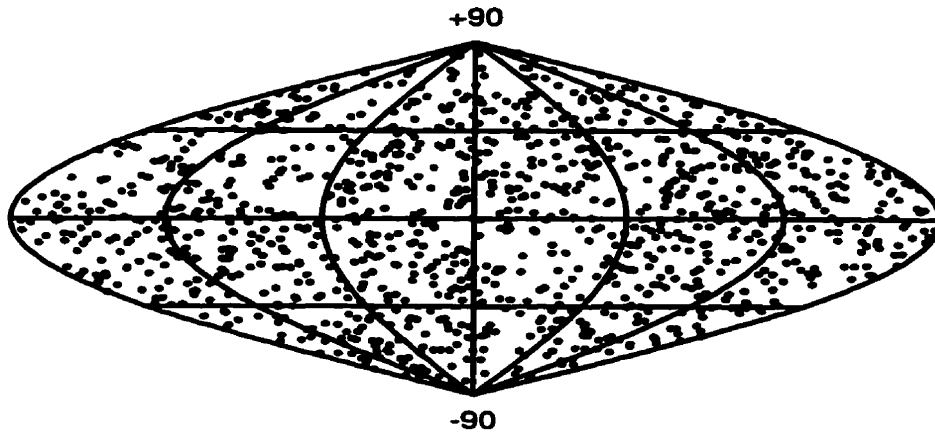


Fig. 2.3: The BATSE 3B catalog of gamma-ray burst positions projected onto the sky, courtesy of the Compton Gamma-Ray Observatory. The deviation from isotropy of the position distribution is not statistically significant.

centred around the given coordinate system, but the second is much better at detecting general anisotropies. For example, if GRBs are Galactic objects, a test to see a dipole moment toward the Galactic centre and a quadropole moment around the Galactic plane are presumably the most important.

The two coordinate-based tests most used are  $\langle \cos \theta \rangle$  and  $\langle \sin^2 b - 1/3 \rangle$ .  $\langle \cos \theta \rangle$  is the mean of  $\cos \theta_i$ , where  $\theta_i$  is the angle between the vector pointing toward the  $i$ -th burst and one pointing toward the Galactic centre. This statistic gives 0 if the distribution is isotropic; a positive value signifies clumping toward or away from the Galactic centre.  $\langle \sin^2 b - 1/3 \rangle$ , where  $b$  is the Galactic latitude, also equals 0 if the distribution is isotropic; a positive value signifies clumping toward the poles, and a negative value shows clumping of the distribution toward the Galactic plane.

Of course, these statistics applied to  $N$  points sampled from an isotropic distribution have uncertainties associated with them, or, more accurately, a width to the distribution of values  $\langle \cos \theta \rangle$  and  $\langle \sin^2 b - 1/3 \rangle$  will take. The width of the distribution can be found by recognising that  $\cos \theta_i$  and  $\sin b_i$  are both uniformly distributed on  $[-1, 1]$  for a random distribution. Therefore, defining the variance for a variable  $x$  as per usual as

$$\sigma^2 = \langle x^2 \rangle - \langle x \rangle^2$$

the variance of  $\cos \theta_i$  is  $1/3$  and that of  $(\sin^2 b_i - 1/3)$  is  $4/45$ . If a large number of independent points are sampled from this distribution, the central limit theorem necessitates that the overall distribution of the means approach a Gaussian, with mean 0 for both, and variances of  $1/(3N)$  and  $4/(45N)$  respectively.

Due to the incomplete sky exposure of BATSE, the distribution of the dataset for an isotropic distribution on the sky will be slightly anisotropic. Briggs *et al* (1996) have calculated the effects of this uneven exposure: for a truly isotropic distribution on the sky, the BATSE distribution should have  $\langle \cos \theta \rangle = -0.013$  and  $\langle \sin^2 b - 1/3 \rangle = -0.005$  (the expected variances are affected insignificantly).

These tests can be performed on the BATSE 3B catalog sources; the values for the two statistics are

$$\langle \cos \theta \rangle = -0.0025 \quad \langle \sin^2 b - 1/3 \rangle = -0.0027 \quad (2.1)$$

The  $\langle \cos \theta \rangle$  statistic varies by  $0.6\sigma$  from the expected value, and  $\langle \sin^2 b - 1/3 \rangle$  by  $0.26\sigma$ , and the BATSE distribution is therefore statistically indistinguishable from an isotropic distribution with the present data. Briggs *et al* (1996) performed a detailed analysis on the distribution using subsets of the total distribution and tested various Galactic models against the distribution. They found that these techniques would have detected a statistically significant deviation if one-half of the locations were within  $86^\circ$  of the Galactic centre (as opposed to  $90^\circ$  for an isotropic distribution), or within  $28^\circ$  of the Galactic plane (as opposed to  $30^\circ$  for an isotropic distribution). They find no evidence in any of the subsets for significant variation from isotropy.

The coordinate-independent tests are somewhat more complicated. The first two considered characterise the dipole moment of the data.

The Rayleigh statistic  $\mathcal{R}$  is defined as

$$\mathcal{R} = \left| \sum_{i=1}^N \vec{r}_i \right| \quad (2.2)$$

which can be thought of as the distance from the origin of a series of random walks, where each step is  $\vec{r}_i$ , the vector displacement to each point  $i$  on the sphere. For an isotropic distribution, this sum should approach zero. As is well-known from random walk theory,  $\langle \mathcal{R}^2 \rangle = N$ .

This statistic can be used as a test of isotropy by calculating the probability  $\alpha_{\mathcal{R}}$  of finding a value of  $\mathcal{R}$  greater than the observed value  $\mathcal{R}_{\text{obs}}$  assuming that the data are drawn from a random distribution. However, this probability is difficult to calculate; a more convenient version of this statistic, which is only valid for large  $N$ , can be applied. Watson (1956, 1983) introduced the statistic

$$\mathcal{W} = \frac{3}{N} \mathcal{R}^2 \quad (2.3)$$

which is asymptotically distributed as  $\chi_3^2$  ( $\chi_\nu^2$  is the distribution of the quantity  $\sum_{i=1}^\nu x_i^2$ , where the  $x_i$  are sampled from the standardised normal distribution). The probability that a  $\mathcal{W}$  randomly chosen from an isotropic distribution is greater than  $\mathcal{W}_{\text{obs}}$  is

$$\alpha_{\mathcal{W}} = \int_{\mathcal{W}_{\text{obs}}}^{\infty} f_{\chi_3^2}(x) dx = F_{\chi_3^2}(\mathcal{W}_{\text{obs}}) \quad (2.4)$$

where  $f_{\chi_3^2}$  is the probability density function of  $\chi_3^2$  and  $F_{\chi_3^2}$  is the upper cumulative probability distribution function of  $\chi_3^2$ . Both of these functions are known analytically, which makes this statistic more easily computable than the Rayleigh statistic. The expected value of  $\mathcal{W}$  is equal to the expected value of  $\chi_3^2$ ; the expectation value of  $\chi_\nu^2 = \nu$ , so  $\langle \mathcal{W} \rangle = 3$ . The distribution is independent of  $N$ , and the variance on the mean of the  $\chi_\nu^2$  distribution is  $2\nu$ . Therefore, the standard deviation of  $\mathcal{W}$  is  $\sigma_{\mathcal{W}} \simeq 2.45$ . This approximation is valid for  $N$  larger than approximately 50, and is therefore well-suited to the study of the GRB distribution.

A statistical test for a quadrupole moment to the distribution which is coordinate-independent is based on the ‘‘orientation’’ matrix

$$M_N = \frac{1}{N} \sum_{i=1}^N \begin{bmatrix} x_i x_i & x_i y_i & x_i z_i \\ y_i x_i & y_i y_i & y_i z_i \\ z_i x_i & z_i y_i & z_i z_i \end{bmatrix} \quad (2.5)$$

which is similar to the usual dipole matrix

$$Q = \frac{1}{N} \sum_{i=1}^N \begin{bmatrix} x_i x_i - 1 & x_i y_i & x_i z_i \\ y_i x_i & y_i y_i - 1 & y_i z_i \\ z_i x_i & z_i y_i & z_i z_i - 1 \end{bmatrix} \quad (2.6)$$

except that  $Q$  is traceless (since, as the points lie on the unit sphere,  $x_i^2 + y_i^2 + z_i^2 = 1$ ) while  $M_N$  has a trace of unity.

Since  $M_N$  is real and symmetric, it has three real eigenvalues  $\lambda_k$ , which must add to one (since  $M_N$  has unit trace). In a coordinate system where  $M_N$  is diagonal, the diagonal

elements are the eigenvalues; since the diagonal elements are the sum of squares, each element must be positive. Therefore, if the data are sampled from an isotropic distribution, each of the  $\lambda_k$  should be equal, and must equal  $1/3$ .

The deviation from isotropy in this case is measured by the Bingham statistic

$$\mathcal{B} = \frac{15N}{2} \sum_{k=1}^3 \left(\lambda_k - \frac{1}{3}\right)^2 \quad (2.7)$$

It can be shown (Watson 1983) that

$$\text{Trace}(M_N^2) = \sum_{k=1}^3 \lambda_k^2 \quad (2.8)$$

so that the calculation of  $\mathcal{B}$  does not require the calculation of the eigenvalues explicitly.  $\mathcal{B}$  is asymptotically distributed as  $\chi_5^2$ , so the probability that a random sample will give a value of  $\mathcal{B}$  greater than the observed  $\mathcal{B}_{\text{obs}}$  is

$$\alpha_{\mathcal{B}} = \int_{\mathcal{B}_{\text{obs}}}^{\infty} f_{\chi_5^2}(x) dx = F_{\chi_5^2}(\mathcal{B}_{\text{obs}}) \quad (2.9)$$

where  $f_{\chi_5^2}$  and  $F_{\chi_5^2}$  are the probability density function and upper cumulative probability function for  $\chi_5^2$ , which are known analytically. The expectation value for  $\mathcal{B}$  is 5 and the standard deviation of the result is  $\sigma_{\mathcal{B}} \simeq 3.16$  by the properties of the  $\chi_5^2$  distribution.

The effect of BATSE's uneven sky exposure changes the expected results for a truly isotropic distribution quite significantly for greater than 1000 bursts; the BATSE exposure gives  $\mathcal{W} = 3 + 0.0020N$  and  $\mathcal{B} = 5 + 0.0077N$ . For the 1122 bursts of the 3C catalog, the expected values for an isotropic distribution on the sky are  $\mathcal{W} = 5.24$  and  $\mathcal{B} = 13.64$ . The standard deviations are affected in a complicated way, increasing with  $N$ . At approximately 1000 bursts,  $\sigma_{\mathcal{W}} \simeq 5$  and  $\sigma_{\mathcal{B}} \simeq 8.5$ .

These analyses have been performed on the BATSE 3B catalog; the results are

$$\mathcal{W} = 0.53 \qquad \mathcal{B} = 5.8 \quad (2.10)$$



The value for  $\mathcal{W}$  deviates from its expected mean by approximately  $0.94\sigma_{\mathcal{W}}$  and  $\mathcal{B}$  by  $0.92\sigma_{\mathcal{B}}$ . Therefore, the deviation from isotropy is not statistically significant for this distribution.

### 2.2.2 The Angular Autocovariance Function

The dipole and quadrupole moments of the distribution are efficient at detecting large-scale anisotropies; however, they are quite insensitive to small-scale variations such as clustering of sources. A better statistical test to examine this effect, familiar from the study of galaxy distributions (e.g., Peebles 1993), is the angular autocovariance function, which examines the excess number of sources over the predicted isotropic value in some small area on the sky.

The precise definition (see, for example, Hartmann & Blumenthal 1989) starts at any given point on the sky, and then examines the probability of finding a second point at an angular separation  $\theta$  and within the solid angle  $d\Omega$ ; this is given by

$$dP = n[1 + w(\theta)]d\Omega \quad (2.11)$$

Since the probability of finding one source in a differential angle is infinitesimal, but the number of sources is large, the distribution is given by the Poisson distribution. Equation 2.11 is often written

$$1 + w(\theta) = \frac{N_p}{N_{pp}} \quad (2.12)$$

where  $N_p$  is the number of pairs with a separation in the interval  $(\theta, \theta + d\theta)$ , and  $N_{pp}$  is the expected number from the Poisson distribution. For  $N \gg 1$  points on the sky, isotropically distributed, this value is

$$N_{pp} = \frac{N^2 \sin \theta d\theta}{4} \quad (2.13)$$

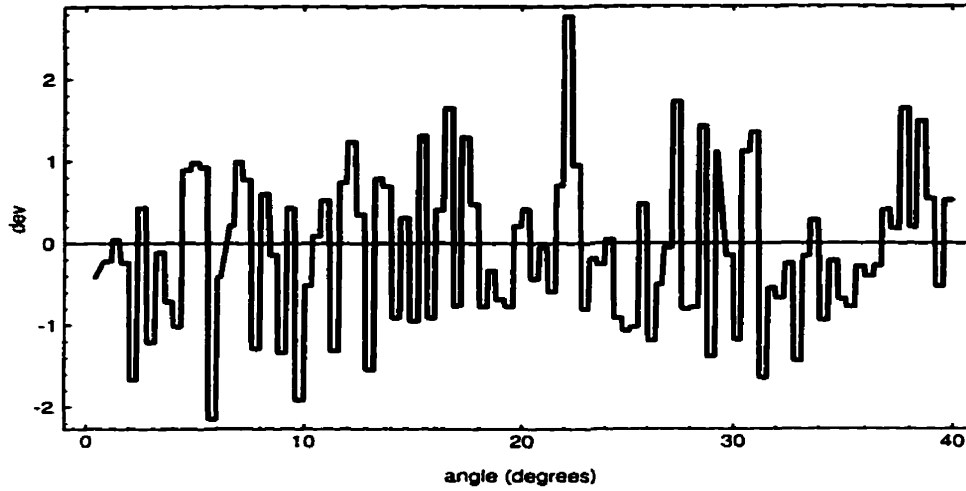


Fig. 2.4: The angular autocovariance function plotted against angle for the BATSE 3B catalog. The  $y$ -axis shows the deviation from the expected value due to an isotropic distribution of sources in units of standard deviations; there is no statistically significant deviation from isotropy in the sample. The one deviation of  $2.8\sigma$  is not unexpected with 100 bins.

This assumes implicitly that the distribution is, on the large scale, isotropic, which is true of the GRB distribution.

The angular autocovariance function for the 3B catalog is shown in figure 2.4 for pair separation angles up to  $40^\circ$ . The deviation from the expected value is shown on the  $y$ -axis in units of standard deviations (just  $1/\sqrt{N_{pp}}$  when  $N_{pp} \gg 1$ ), and no significant deviations from an isotropic sample are seen.

### 2.3 Distribution in Flux

While the distribution in position on the sky of the observed GRBs appears to be completely random, the same does not hold for the distribution in flux. The data seem to suggest that we are currently viewing out to near the edge of the distribution of the bursts radially, or, if they are cosmological objects, we might be viewing effects of the curvature of the universe.

This evidence came out of examining how the number of sources with flux greater than  $F$  varies with  $F$ . For a isotropic and homogeneous distribution in a Euclidean space, the number of sources between  $r$  and  $r + dr$  is

$$dN = 4\pi r^2 \rho dr \quad (2.14)$$

where  $\rho$  is the number density of sources.

For standard candles, the flux received from a source at distance  $r$  is

$$F = \frac{A}{r^2} \quad (2.15)$$

where  $A$  is a constant related to the standard candle luminosity.

From these equations, the distribution in flux of the standard candles can be found:

$$\frac{dN}{dF} = 2\pi\rho A^{3/2} F^{-5/2} \quad (2.16)$$

and the integrated distribution is

$$N(> F) = \frac{4}{3}\pi\rho A^{3/2} F^{-3/2} \quad (2.17)$$

Therefore, a homogeneous and isotropic distribution of standard candles has an integrated distribution in flux which falls off like  $F^{-3/2}$ .

The GRB distribution in flux follows this power law for the brightest bursts, but shows a deficit in the dimmer bursts, suggesting that the observations are probing to the edge of the distribution.

The peak photon flux distribution for the BATSE 3B catalog is shown in figure 2.5. The dashed line has a slope of  $-3/2$  for comparison, which matches the bright bursts well. The dim bursts are fewer in number than would be predicted from a uniform distribution of standard candles in a Euclidean spacetime.

Another statistical test to determine the uniformity of a radial distribution of sources is the  $\langle V/V_{\max} \rangle$  test, developed by Schmidt (1968) and applied to gamma-ray bursters somewhat later (Schmidt, Higdon, & Hueter, 1988). The test is based on sampling the volume enclosed by a particular source and averaging - if the sample is uniform and the sources are standard candles, the values should be uniformly distributed between 0 and the volume corresponding to the largest radius at which a source could be seen ( $V_{\max}$ , which is determined by the detector sensitivity). Therefore, the ratio  $V/V_{\max}$  would be uniformly distributed between 0 and 1, and the average should be  $1/2$ . The variance for a single measurement is  $1/12$ , and by the central limit theorem, the standard deviation of the mean for a sample of  $n$  sources should be  $1/\sqrt{12n}$ .

If the peak count of the burst is  $F_p$  and the minimum detectable flux is  $F_{\min}$ , then the ratio of the burst distance to the maximum distance is

$$\frac{r}{r_{\max}} = \left( \frac{F_p}{F_{\min}} \right)^{-1/2} \quad (2.18)$$

and the ratio of the volumes is

$$\frac{V}{V_{\max}} = \left( \frac{F_p}{F_{\min}} \right)^{-3/2} \quad (2.19)$$

Note that this analysis assumes that the flux drops off like  $r^{-2}$ , which is the result for Euclidean space. The same does not hold true for a curved spacetime.

Since the actual distance  $r$  does not appear in the above equation, the test can be conducted without knowledge of the distance scale of the bursts. This has been done for the BATSE 3B catalog; the value is

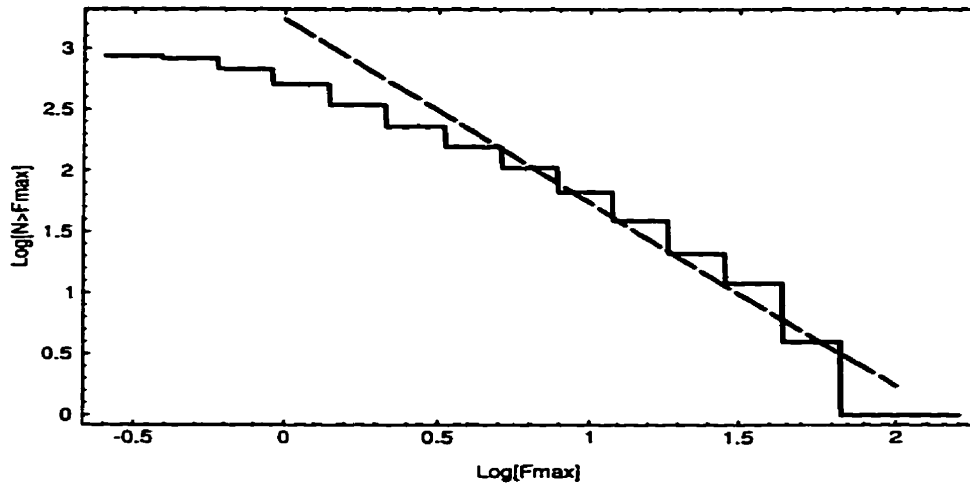


Fig. 2.5: Plot of  $\log N(> F_{\max})$  vs  $\log F_{\max}$  for the BATSE 3B catalog, where  $F_{\max}$  is the maximum flux of a burst in photons/cm<sup>2</sup>/s on the 256ms timescale and  $N(> F_{\max})$  is the number of bursts with flux  $> F_{\max}$ . The dashed line has a slope of  $-3/2$ , which would be observed from a uniform distribution of standard candles in a Euclidean spacetime. The deficit of dim bursts suggests we are probing near the edge of the distribution, or evolutionary or cosmological effects are at work. Using maximum flux on a different timescale does not change the shape of the plot.

$$\frac{V}{V_{\max}} = 0.33 \pm 0.01 \quad (2.20)$$

This does not agree with the value of 0.5 which would result from a uniformly distributed set of bursts; it suggests that there are more bursts closer to us than would be the case for a homogeneous sample. This again points to a more complex model than homogeneously distributed standard candles in a Euclidean spacetime.

Both these tests use the peak photon flux as the “standard candle” measure - that is, it is assumed that the peak photon number luminosity emitted by a burst is constant from burst to burst. It is unclear whether this is the best datum to use; Petrosian & Lee (1996) suggest that the fluence (flux integrated over the whole burst) might be a better standard candle, as suggested by some of the more model-independent predictions of the burst physics. However, the results obtained either way are qualitatively similar, suggesting that the widths in the distributions of source fluence and source peak number luminosity are similar or much less than the observed variation in flux (so that most of the variation seen in burst flux comes from varying distance rather than varying source luminosities).

The most obvious interpretation of these data is a scenario where the GRBs are produced at cosmological distances: the isotropy on the sky is natural, and the edge of the distribution is due to evolutionary or spacetime-curvature effects (for a discussion of these factors see, for example, Meszaros & Meszaros 1995). However, GRBs located in a very extended Galactic halo can be accommodated if the halo is large enough, and the concentration of bursters toward the Galactic centre is somehow suppressed (by, for example, requiring a turn-on time before which the objects cannot burst, or by beaming of the emission). These models are discussed in more detail in chapter 4.

## 2.4 Counterparts at Other Frequencies

The discovery of a counterpart to a classical GRB at another frequency would be an important clue as to their origin. However, despite extensive efforts, only a single marginally

significant coincidence has been found in x-rays.

Observing a GRB counterpart is a difficult task at best. The error boxes on the BATSE burst positions are rather large, and a deep survey which covers the entire region of sky would be prohibitively time-consuming, and possibly futile if the counterpart is also a bursting source. However, many GRBs have positions which are much better defined than the BATSE error boxes due to multiple observations by different instruments.

The most accurate positions are found by networks of interplanetary telescopes, where the separation between the telescopes in light travel time is much greater than the burst rise time (see, e.g., Lund 1995). Such networks have been arranged three times over the last two decades (called InterPlanetary Networks). The first such network (IPN-1) was in operation between November 1978 and February 1980, and included the Pioneer-Venus Orbiter (PVO), HELIOS-2, VENERA 11 and 12, as well as many near-Earth satellites. IPN-2 operated between 1981 and 1983, and IPN-3 was active between 1990 and 1992. In total, roughly 40 positions with accuracies better than  $50 \text{ arcmin}^2$  have been analysed with data from these networks. Parts of IPN-3 are still in operation, and additional satellites are being added.

#### *2.4.1 Quiescent Counterparts*

Many models of GRBs imply steady emission in various parts of the electromagnetic spectrum. Detailed observations at different frequencies of the GRB error boxes after (or before, by analysing archival records) can at worst constrain the different models, or at best find a counterpart which is a known source. This sort of find would provide powerful evidence for the distance scale to these objects.

#### *Radio emission*

Despite several attempts to discover steady emission in the radio, no incontrovertible detections have been made. COBE has observed several GRB error boxes at 31, 53, and 90

GHz (Bontekoe *et al* 1995), the Cambridge Low Frequency Synthesis Telescope (CLFST) observed the GB 920711 error box at 151 MHz (Koranyi *et al* 1994), the GB 940301 error box (the brightest yet-observed GRB) was observed at 1.4 GHz and 0.4 GHz at the Dominion Radio Astrophysical Observatory (DRAO) (Frail *et al* 1994), and deep VLA observations at 20 cm of three BATSE GRB error boxes have been performed over two years (Palmer *et al* 1995); none of these surveys found any detectable, statistically significant sources which were viable candidates. The VLA observations provided the most stringent upper limits on the emission, on the order of  $100\mu\text{Jy}$ .

### *Infrared emission*

The only major search for GRB counterparts in the infrared was performed by analysing the IRAS database for sources in error boxes of 23 well-localised GRBs (Schaefer *et al* 1987). Three sources were discovered, but were all shown to be unrelated to the GRBs.

### *Soft x-ray emission*

Many models which invoke neutron stars as the sources of GRBs imply thermal emission from the star's surface in the soft x-ray range due to accretion onto the star from the interstellar medium. The spectrum radiated from this process is not expected to be precisely thermal; however, it should be fairly close (see, for example, Zampieri *et al* 1995). A quiescent counterpart in the soft x-ray range would argue quite strongly for a neutron star origin.

The most powerful soft x-ray searches in GRB error boxes have been performed by the ROSAT telescope using the ROSAT all-sky survey data. 30 error boxes of the 2nd IPN catalog (Greiner *et al* 1995) and 15 error boxes of the 3rd IPN catalog (Greiner *et al* 1996) have been analysed. 27 sources have been found, which is within statistical estimates of the expected number due to mean source density. These sources have all been identified in the optical, and show no evidence of being GRB quiescent counterparts. This survey puts an upper limit on the flux of roughly  $10^{-13}$  erg/cm<sup>2</sup>/s in the 0.1 - 2.4 keV energy range.



All but one deep ROSAT observations of a few small GRB error boxes have also failed to find any significant emission, placing upper limits of roughly  $10^{-14}$  to  $10^{-15}$  ergs/cm<sup>2</sup>/s (Boër *et al* 1993).

The single positive marginally significant detection (chance probability  $10^{-2}$  to  $10^{-3}$ ) was recently made by Hurley *et al* (1996) using ROSAT. They examined the GB 920501 error box 18 days after the burst for 2000s of integration time and found a weak x-ray source. A longer 30ks observation detected 118 net photons in the energy range 0.07-2.4 keV, with a spectrum consistent with thermal bremsstrahlung from a  $7.7 \times 10^6$  K plasma with about  $10^{22}$  cm<sup>-2</sup> HI column density. The unabsorbed photon flux was approximately  $9.4 \times 10^{-13}$  ergs/cm<sup>2</sup>/s. The column density sets a minimum distance of several kpc, though an extragalactic source could not be ruled out. However, since roughly 50 errors boxes have been examined, the probability of this detection being purely random is somewhat high.

The Extreme Ultraviolet Explorer (EUVE) performed a deep observation of the GB 920325 error box and failed to detect a counterpart (Hurley *et al* 1995). The upper limits are roughly  $10^{-12}$  to  $10^{-13}$  ergs/cm<sup>2</sup>/s in the 40-760 Å range.

### *High-energy gamma-ray emission*

If GRBs are cosmological, there will be almost no ultra-high-energy (UHE) gamma-ray emission (in the  $> 10$  TeV range) received at the Earth, as the gamma-ray photons will pair-produce on intergalactic infrared photons (see, for example, Stecker & De Jager 1992). Therefore, a detection of UHE gamma-rays would suggest a Galactic origin of these objects.

The data from the Whipple Observatory Reflector, which is sensitive to 0.4-4 TeV photons, were found to be uncorrelated with BATSE bursts (Connaughton *et al* 1994). The CYGNUS-I air shower array, which can see photons of energies  $> 50$  TeV, has found no UHE emission from the examined GRB error boxes (Alexandreas *et al* 1994). The data from the Thebarton air shower array, sensitive to above 100 TeV (Smith *et al* 1995), also show no excess emission.

### *Neutrino emission*

An interesting consequence of many GRB models is a flux of neutrinos with a luminosity of similar magnitude to that of photons. These generally are a product of cosmological rather than Galactic models, and a significant neutrino detection would be important. However, it has been shown (Ostrowski & Zdziarski 1995) that this expected flux is many orders of magnitude too low to be detected by the current or planned neutrino detectors. Their estimate is relatively model-independent, and independent of the distance scale, as its only assumption is that the photon and neutrino luminosities are of similar magnitude.

Several neutrino experiments have attempted to find neutrino events associated with GRBs. The Irvine-Michigan-Brookhaven (IMB) detector (LoSecco 1994), the Soudan 2 detector (DeMuth *et al* 1994), and the Mont Blanc Neutrino Telescope (Vernetto *et al* 1995) have shown no neutrino flux greater than is expected from atmospheric events. The flux limit from these experiments for the 183 Venera and Ginga GRBs is roughly  $2 \times 10^7$  neutrinos/cm<sup>2</sup> over a burst.

#### *2.4.2 Bursting Counterparts*

The search for a bursting counterpart requires more than just an accurate burst location, as a delayed search may not catch the emission. The need for a high-speed network to disseminate GRB location information to telescopes searching for counterparts was recognised early in the development of the CRGO, and the BACODINE network was established (for a review, see Barthelmy *et al* 1995). BACODINE uses BATSE position data, which it calculates and disseminates over the Internet with time delays of often less than four seconds, though occasionally as long as seven seconds or more. This is shorter than the typical burst time, and allows rapid observation.

The Rapid Response Network (RRN) is one of the collaborations using the BACODINE data (McNamara *et al* 1995), as well as IPN network positions. The RRN consists of 18 optical and four radio observatories located around the world, including the U.S. Air Force

GEODSS system. GEODSS consists of three sites that employ large-aperture optical telescopes with wide fields of view that can reach  $m_V \simeq 17$  with a 0.6 second integration. The system has been in operation since 1993, but has not found a single counterpart at optical or radio frequencies.

The Explosive Transient Camera (ETC - see Vanderspek, Krimm, & Ricker 1995 for a review) is another optical instrument which is triggered by BACODINE. It is a fully automated, wide-field telescope which can see to an  $m_V$  of 6.5 to 10 (depending on sky conditions) with a one-second exposure. The ETC has been operating since 1990 and has failed to discover any statistically significant optical transients.

## 2.5 *Line Features in GRBs*

The early observations of GRBs with early telescopes found evidence for line features in the spectra which were readily attributable to radiation processes in the  $10^{12}$  G surface fields of neutron stars (see section 4.1.2), which favour a Galactic model (it is possible, though difficult, to generate lines in a cosmological model via gravitational femtolensing of the radiation as it travels from the source to the Earth). However, none have been observed with any statistical significance in the 52 BATSE bursts with sufficient intensity, which suggests that perhaps the earlier measurements were artifacts of fitting schemes or background processes.

The evidence from the pre-BATSE observations strongly favoured the existence of these lines. The first observations were from the KONUS experiments on the Venera 11 and Venera 12 spacecraft (Mazets *et al* 1981), where both absorption and emission lines were seen in the hard x-ray region of the spectrum. Their analysis suggested that the existence of absorption lines in the 30-70 keV range were characteristic for GRBs rather than the exception, and also found many examples of emission lines near 400-450 keV. However, the telescope was sensitive to the energy range of 30 keV to 2 MeV, so the absorption lines features occurred near the lower edge of the detector range.

The most likely explanation for these lines is cyclotron scattering in  $10^{12}$  G magnetic fields for the 30–70 keV absorption lines, and redshifted electron-positron pair annihilation lines for the 400–450 keV lines.

The Ginga telescope covered a range of 1.5 keV to 375 keV, making it much more sensitive to features in the 30–70 keV range. Three bursts were observed with well-defined absorption features, GB870303 and GB880205 initially (Murakami *et al* 1988), and later GB890929 (Yoshida *et al* 1991). The probability that the observed variations were statistical variations from a continuous spectrum were small, on the order of  $10^{-3}$  to  $10^{-5}$ .

The Franco-Soviet LILAS experiment on the Phobos 2 spacecraft also detected line features in the August 6, 1988 event (Barat *et al* 1991). The LILAS energy range was roughly 3 keV to 1 MeV; line features were seen at 14 and 28 keV, relatively far from the energy thresholds.

The observed absorption lines occurred at energies separated by a factor of roughly 2, suggesting that these are first and second harmonics of some absorption process (most likely cyclotron scattering).

Until BATSE, these observations had essentially established the existence of these absorption and emission lines GRB spectra, which strongly pointed to a high-magnetic field neutron star origin for the bursts (see the discussion in section 4.1.2). The positive identifications from three separate experiments to a reasonably high degree of statistical accuracy seemed incontrovertible.

Unfortunately, in the 52 bursts in the BATSE 3B catalog which have high enough counts to analyse for spectral details, there have been no indications of line features. The detectability of bursts by BATSE has been discussed by Band *et al* (1995), which suggests that line features such as those observed by Ginga could have been observed by BATSE with relatively high probability. Even though the minimum energy threshold of BATSE (near 15 keV) is quite close to the expected energy of the absorption lines, it is somewhat troubling that no significant lines have been observed by this instrument; there is only approximately a 10 %

chance that the lack of BATSE observations is consistent with the earlier data.

Hopefully this problem will be resolved with future data from the ALLEGRO telescope, which is designed specifically to be sensitive to the appropriate energy range with high energy resolution (Matz *et al* 1996). If the line features in the three Ginga bursts were real, given that Ginga observed 23 GRBs in its 3.4 year operation, ALLEGRO should see approximately 60 bursts with line features over its two-year operating cycle.

## 3. PULSAR OBSERVATIONS

### 3.1 *Basic Observational Characteristics*

All we know about pulsars comes from data on their radiative emission. Therefore, the observations of these objects breaks down into only a few categories:

- **Pulse Period:** The time between pulses after averaging over many pulses gives a very accurate, and bin-independent, value. Its stability was one of the determining factors in choosing the model of a spinning compact object.
- **Period Derivative:** The period between pulses changes gradually over time; this period derivative is quite stable as well. Assuming that this energy loss is due to magneto-dipole radiation strongly suggests the  $10^{12}$  G surface fields.
- **Light Curve:** The shapes of the light curve for different pulsars can vary quite significantly, not only between different pulsars but in photon energy for a particular pulsar. Radio light curves can be somewhat complex, while the known gamma-ray light curves are generally only singly- or doubly-peaked.
- **Spectrum:** The spectrum of the radiation in different frequency regimes strongly constrains many models of pulsar emission. Matching the observations across the whole electromagnetic spectrum is a requirement of any physically realistic global model for the magnetosphere. The total power output at various frequencies is also an important parameter of pulsar emission, though it is often difficult to determine due to distance and beaming uncertainties.

- **Polarisation:** The polarisation of the emitted photons is another important piece of data which constrains the physics of the problem; this has been measured for the low-frequency pulsar emission, but cannot yet be observed for the gamma-ray emission. The next-generation gamma-ray telescopes may be able to determine photon polarisation, however.

### 3.2 *Radio Emission*

Pulsars were first observed in the radio band, and at present all known pulsars but one are observable in this frequency range. The exception is the Geminga pulsar, which is only seen in gamma-rays and X-rays - why this object is *not* seen in radio is unclear, though the prevailing explanation is that the radio emission is present but not beamed toward the Earth.

The physical process that generates the radio emission is almost certainly due to a coherent plasma process. This is required by the very high brightness temperatures observed; if a black-body spectrum is fit to the radio emission, the effective temperatures are often  $10^{25}$  K, and in some cases as high as  $10^{30}$  K (see, for example, Manchester & Taylor 1977). Such temperatures can only be generated by a (much lower-temperature) plasma radiating coherently in some fashion.

This thesis focusses on the gamma-ray emission from pulsars, so little will be said about the details of the radio emission. However, an important measurement that can be made from emission at these low frequencies is the inclination of the magnetic dipole moment to the rotation axis of the pulsar (see figure 1.1).

Two methods exist to make this estimate; both are somewhat model-dependent, and therefore the estimates must be treated with some caution. The first (Rankin 1990) assumes a conal model of emission from pulsars, where the peaks in the light curve are due to emission both from the edges of the cone and from a core component. The core component can be used to estimate the inclination angle; the width of the core component in degrees (with

360° being a full period),  $W_c$ , is given by the relatively simple expression

$$W_c = \frac{2.45^\circ}{P^{1/2} \sin \chi} \quad (3.1)$$

where  $P$  is the pulsar period and  $\chi$  is the inclination angle. This analysis can be done for any pulsar with a core component in its light curve.

The second method, due to Radhakrishnan & Cocke (1969), is based on several assumptions: the magnetic field around the pulsar is dipolar, and the charges follow the field lines and beam their radiation along their velocities. Then the linear polarisation is uniquely determined by the projection of the magnetic field onto the sky. For a dipole field, the position angle of the polarisation  $\phi_p$  is then given by

$$\tan \phi_p = \frac{\sin \chi \sin \Omega t}{\sin \beta \cos \chi - \cos \beta \sin \chi \cos \Omega t} \quad (3.2)$$

where  $\beta$  is the angle between the rotation axis and the direction to the observer. Despite the fact that  $\beta$  is unknown, the observed run of the position angle  $\phi_p$  agrees so closely with this dependence that both  $\beta$  and  $\chi$  can be found. However, in most cases the run of the position angle does not agree closely enough to determine a significant pair of values.

The two techniques give some degree of convergence, though the uncertainties on the values of  $\chi$  can be quite large (see, for example, Beskin, Gurevich, & Istomin 1993).

### 3.3 *The Gamma-Ray Pulsars*

To date, seven pulsars have been observed in gamma-rays at high statistical significance. Six of these have been observed above 50 MeV by the EGRET telescope on the Compton Gamma-Ray Observatory (CGRO); PSR 1509-58 has only been seen at frequencies less than an MeV.

Significantly more gamma-ray pulsars may remain undetected, as identification of periodicity in the gamma-ray flux can be difficult with low flux observations. Notably, there are three sources in the second EGRET catalog (Thompson *et al* 1995) which are positionally



Pulsar	$P$	$\dot{P}$	$\tau$	$d$	$L_\gamma$	$\eta$	Reference
Crab	0.0333	421	1250	2.49	$3.7 \times 10^{35}$	$8.1 \times 10^{-4}$	Ulmer <i>et al</i> 1995
1509-58	0.150	1540	1540	5.81	$1.1 \times 10^{36}$	$6.2 \times 10^{-2}$	Laurent <i>et al</i> 1994
Vela	0.0893	125	$1.1 \times 10^4$	0.61	$1.6 \times 10^{35}$	$2.3 \times 10^{-2}$	Kanbach <i>et al</i> 1994
1706-44	0.102	93.0	$1.7 \times 10^4$	1.82	$1.6 \times 10^{35}$	$4.3 \times 10^{-2}$	Thompson <i>et al</i> 1992
1951+32	0.0395	5.85	$1.1 \times 10^5$	2.37	$7.9 \times 10^{34}$	$2.1 \times 10^{-2}$	Ramamanamurthy <i>et al</i> 1995
Geminga	0.237	11.0	$3.4 \times 10^5$	0.16	$5.7 \times 10^{33}$	0.15	Mayer-Hasselwander <i>et al</i> 1994
1055-52	0.197	5.8	$5.4 \times 10^5$	1.53	$5.9 \times 10^{34}$	0.66	Fierro <i>et al</i> 1993

Tab. 3.1: Parameters for the seven known gamma-ray pulsars, sorted by characteristic age. The columns are the pulsar name, the period  $P$  in seconds, the period derivative  $\dot{P}$  in units of  $10^{-15}$  s/s, the characteristic age determined from  $P$  and  $\dot{P}$  in years, the distance  $d$  in kpc, the gamma-ray luminosity  $L_\gamma$  in ergs/s, the gamma-ray efficiency (fraction of power emitted in gamma-rays), and the reference for the flux data. The distances are taken from the pulsar database at Princeton (maintained by J. Taylor), and the gamma-ray luminosities are calculated by assuming the *average* power emitted each period is beamed into a solid angle of  $2\pi$ .  $\eta$  is calculated assuming that the magnetic dipole moment and rotation axis are perpendicular, and is therefore a lower limit.

coincident with three radio pulsars (PSR B1046-58, PSR B1823-13, and PSR B1853+01) often mentioned as candidates for high-energy emission. These objects are all rather noisy radio pulsars, making precise location difficult, and are in regions of low EGRET exposure and high gamma-ray background. Next-generation gamma-ray telescopes may, however, significantly increase the number of known gamma-ray pulsars.

The properties of the seven known pulsars are summarised in table 3.1. The characteristic ages are calculated assuming energy loss due to magneto-dipole radiation, as discussed in section 1.1.3, and the gamma-ray luminosities are calculated assuming that the *average* power is beamed into  $2\pi$  steradians (this is the power averaged over a period, and therefore is less than the power emitted in the pulse). The gamma-ray efficiency  $\eta$  is simply the ratio of power emitted in gamma-rays to the total (gamma-ray and magneto-dipole) power emitted.

### 3.3.1 Gamma-Ray Light Curves

The shapes of the light curves seen in these seven pulsars varies considerably. Figure 3.1 shows these light curves for the six of these pulsars along with their light curves at other frequencies for comparison. Figure 3.2 shows the light curve for PSR 1509-58 (not included

in the first plot due to its relatively late addition to the membership of the gamma-ray pulsars) (Ramanamurthy *et al* 1995).

- **The Crab Pulsar (PSR 0531+21):** This was the first pulsar to be observed in gamma-rays, and is often taken to be a prototypical gamma-ray pulsar. It is the youngest of the known pulsars, with an age of only 941 years, which we know quite accurately due to Chinese records of the Crab supernova in 1055 AD. Its gamma-ray light curve is doubly peaked, with the second peak following the first by  $0.40 \pm 0.02$  in phase, where a phase of 1 is a full period (Nolan *et al* 1993). Its gamma-ray peaks are almost exactly lined up with the peaks different frequencies, down to radio waves, suggesting that the emission regions for radio waves and gamma-rays are quite close to each other in the magnetosphere (or light travel time delays would shift the peaks relative to each other).
- **The Vela Pulsar (PSR 0833-45):** The light curve for the Vela pulsar is also double-peaked, though the two peaks are almost identical. The phase separation of the peaks is  $0.424 \pm 0.002$  (Kanbach *et al* 1994), almost equal to the value for the Crab pulsar within experimental limits. The gamma-ray light curve is quite different than that in the radio: the first gamma-ray peak trails the radio peak by  $0.118 \pm 0.001$  in phase, and there is no second peak in radio.
- **The Geminga Pulsar:** This was only recently discovered to by a pulsar by Halpern & Holt (1992); it is unique in that there is no observable emission at frequencies below X-ray, and particularly none in radio. Its light curve is also unique, doubly peaked but with peaks separated by 0.5 in phase (Mayer-Hasselwander *et al* 1994).
- **PSR 1951+32:** The light curve for this pulsar is also doubly peaked, with a phase separation between the peaks of 0.44 (Ramanamurthy *et al* 1995). The first peak trails the single radio peak by 0.1 in phase.

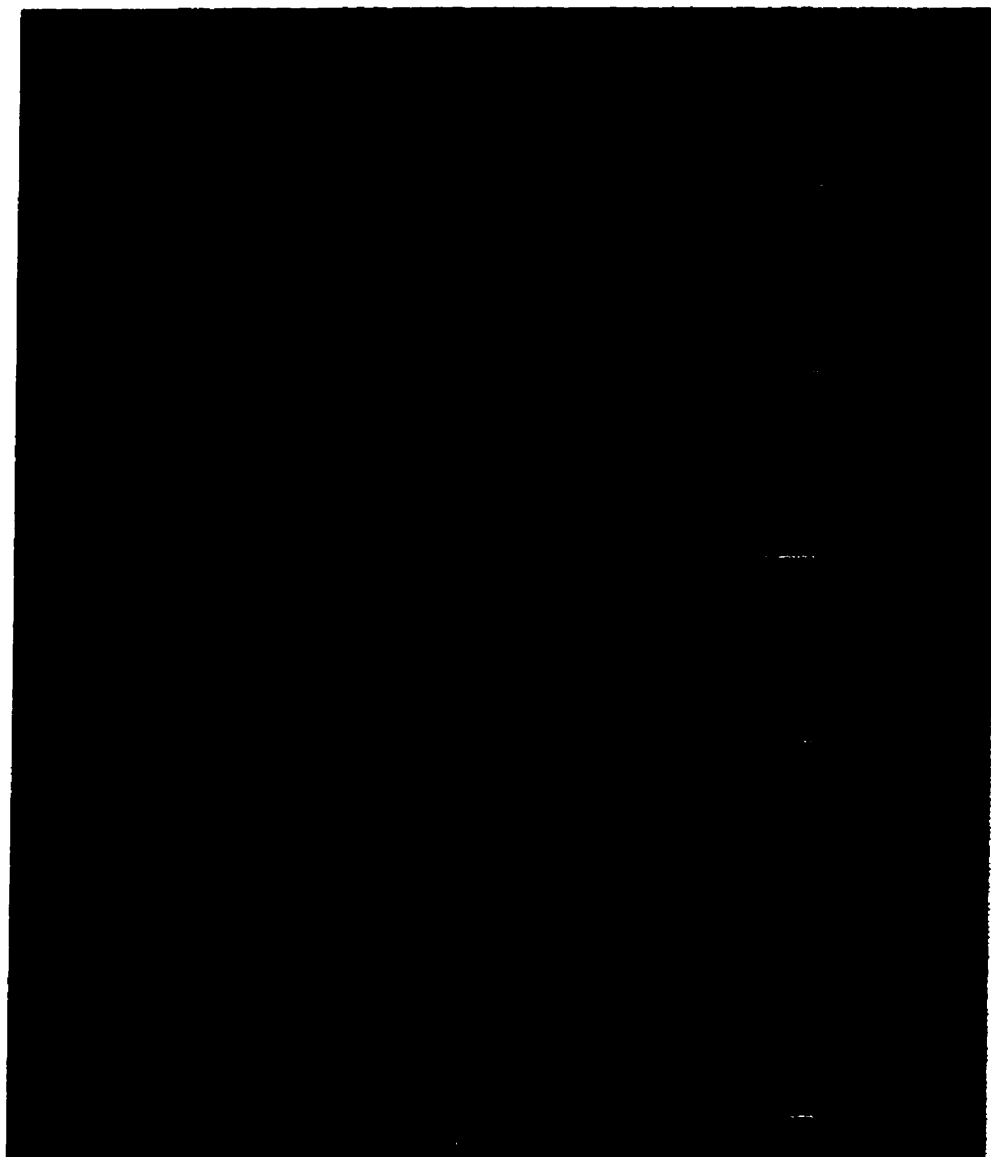


Fig. 3.1: Radio, optical, x-ray, and gamma-ray light curves for all of the known gamma-ray pulsars except PSR 1951+32. All gamma-ray light curves are shown at roughly 100 MeV except PSR 1059-58, which is shown at approximately an MeV, as it shows no detectable emission at the higher frequencies. The wide variety of gamma-ray light curves and their relationship to the lower energy emission must be described by any reasonable gamma-ray pulsar model. This plot was copied from the EGRET archives.

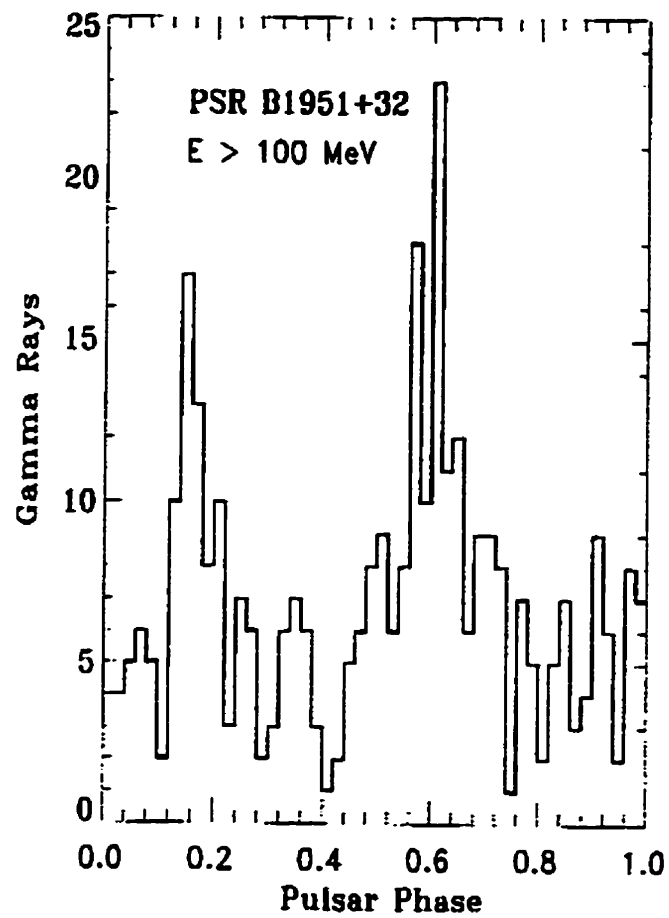


Fig. 3.2: The  $> 100$  MeV gamma-ray light curve for PSR 1951+32, from Ramanamurthy *et al* (1995) (their Figure 1).

- **PSR 1706-44:** This pulsar has a relatively complex light curve. One large peak dominates, and there is some evidence for this main peak to be an overlapping pair of peaks, and for a smaller peak (Nolan *et al* 1996)); however, the data is too sparse to make any convincing statistical claims. There is no coincidence in phase with the single radio peak.
- **PSR 1055-52:** The low flux observed from this pulsar make clear statements about the light curve somewhat difficult; the gamma-ray light curve definitely has a large main peak which lead the first radio peak slightly, and possibly has a second smaller peak which roughly coincides in phase with the second radio peak.
- **PSR 1059-58:** This pulsar shows no observable emission above a few MeV; the light curve show is for approximately 300 keV. It has a single, broad peak which is shifted in phase from the radio and x-ray peaks.

Early observations (e.g., Nolan *et al* 1993) were unable to distinguish between the background and the low flux from the pulsar, and it was believed that the gamma-ray emission was largely shut off for a significant fraction of the period. However, recent work (Nolan *et al* 1996) shows that these objects emit gamma-rays throughout their cycle, though at a significantly lower level off-peak than on-peak (by roughly a factor of 100).

Any gamma-ray pulsar model must be able to explain this wide variation in the observed properties of the light curves; none so far have been completely successful (see chapter 5).

### 3.3.2 *Gamma-Ray Spectra*

The spectrum of radiation in astrophysics is always a powerful instrument to constrain the physics. The spectra observed in gamma-rays do not correspond well to any simple physical process (blackbody radiation, thermal brehmstrahlung, or monoenergetic emitters of synchrotron or curvature radiation), and vary quite widely across the observed gamma-ray pulsars.

Figure 3.3 shows the gamma-ray photon number flux spectra for the six gamma-ray pulsars detected by EGRET. They are generally fit reasonably well by a single power law, the index of which varies between -1.18 (for PSR 1055-52) and -2.15 (for the Crab pulsar), and a break. The location of the break is often difficult to determine (Grenier, Hermsen, & Henriksen 1993), though better data is making the fits more significant. However, the power-law fits are often only rough approximations to the true spectrum. There is some suggestion for a trend to harder spectra with older pulsars, but the statistical significance is limited by the difficulty of fitting the spectra with single power laws.

The most curious of all the spectra is that of PSR 1509-58 (figure 3.4), which breaks at little over an MeV (Gunji *et al* 1994). It is a relatively young, fast pulsar, like the Crab, but has a drastically different spectrum. The outer gap model (see section 5.3.3) predicts a similar spectrum to that of Vela, and our model predicts a very high-energy spectrum (see section 9.10.7), both in opposition to the observations.

### 3.3.3 Gamma-Ray Power Output and Efficiency

The total radio power output of all pulsars is many orders of magnitude less than the total power loss observed by the pulsar spin-down, which is due to very long wavelength magneto-dipole radiation. The same is not true for the gamma-ray power, which can, in some cases, almost rival the spin-down power in magnitude.

The gamma-ray efficiency is defined as

$$\eta = \frac{P_\gamma}{P_{\text{tot}}} \quad (3.3)$$

where  $P_\gamma$  is the total gamma-ray power and  $P_{\text{tot}}$  is the total power (in general magneto-dipole + gamma-ray output). The total power is often estimated as the magneto-dipole power, which can be directly calculated when the period and period derivative for a pulsar are known. The gamma-ray power output is somewhat more difficult to estimate, as it can only be calculated from the observed flux. Therefore, the distance to the pulsar and the

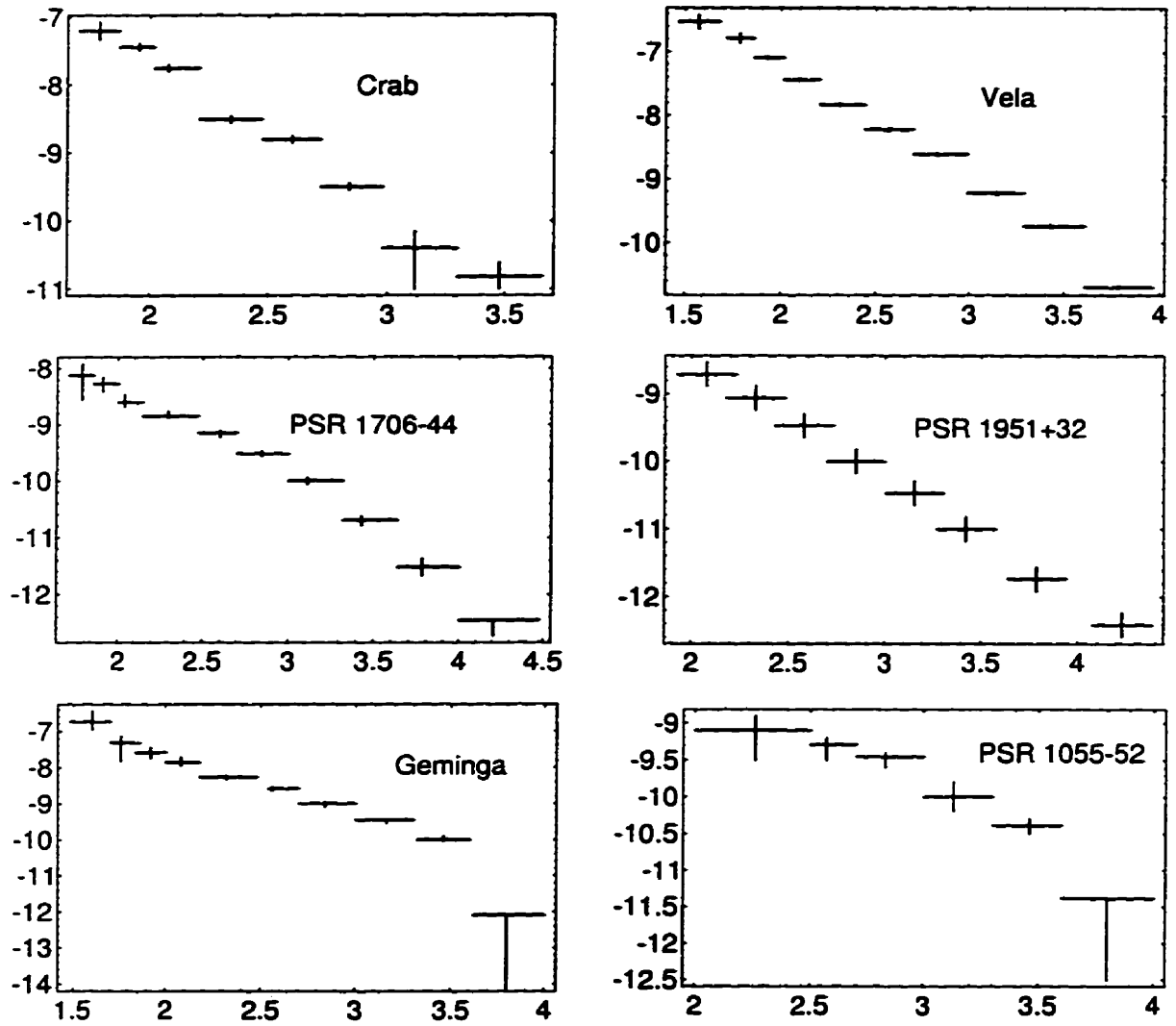


Fig. 3.3: The gamma-ray spectra for the six pulsars observed by EGRET. The horizontal axis units are logarithm of photon energy in MeV, and the vertical axis is the logarithm of differential photon number in units of  $\text{ph}/\text{cm}^2/\text{s}/\text{MeV}$ .

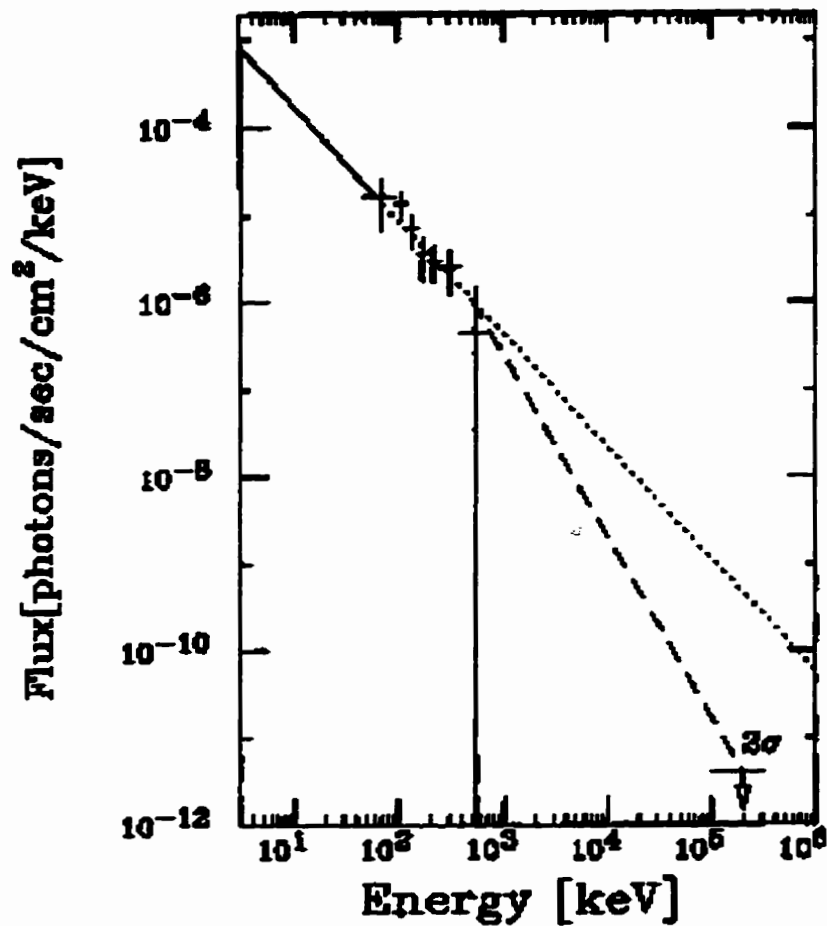


Fig. 3.4: The spectrum above 2 keV for PSR 1509-58. The solid line shows the Ginga best-fit line, and the crosses from the Welcome-1 balloon-borne detector. The  $2\sigma$  upper limit is derived from COS-B data. The dotted line is the extension of the power law spectrum from the x-ray band, and the dashed line was drawn by connecting the 500 keV point on the x-ray power-law spectrum and the  $2\sigma$  upper limit. The figure is taken from Gunji *et al* (1994) (their figure 5).



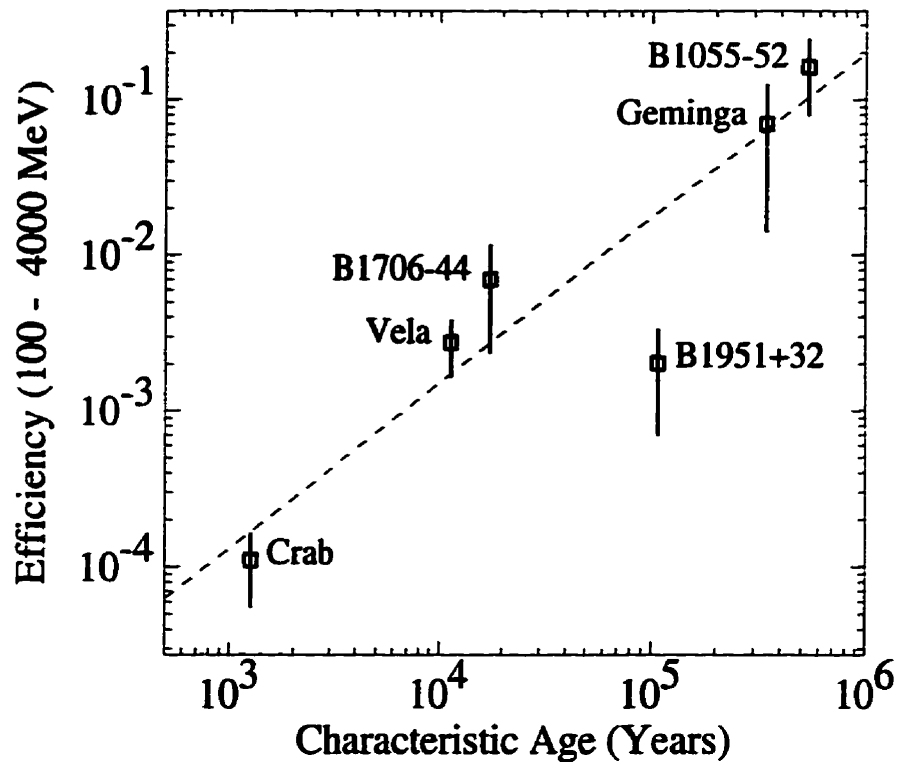


Fig. 3.5: The variation of gamma-ray efficiency for all of the known gamma-ray pulsars (except PSR 1509-58, which does not emit above MeV energies) with characteristic age. There is a clear trend toward higher efficiencies in the older pulsars, and Geminga and PSR 1055-52 have efficiencies approaching unity. The plot is taken from Nolan *et al* (1996), and assumes a beaming angle of 1.0 steradian for each pulsar.

solid angle into which the power is radiated must be known, leading to large uncertainties.

Figure 3.5 shows the gamma-ray efficiencies of the known gamma-ray pulsars (not including PSR 1509-58, which only radiates at energies near and less than an MeV) against their characteristic ages. There is a clear trend to higher gamma-ray efficiencies as the pulsar age increases, and Geminga and PSR 1055-52 both have efficiencies which are close to unity. The plot is taken from Nolan *et al* (1996) (their Figure 4), and assumes a beaming angle of 1.0 steradian for each pulsar.

## 4. NEUTRON STAR-COMET GAMMA-RAY BURST MODELS

The dearth of data on GRBs has allowed a proliferation of theoretical models, though the increasing amount of information from BATSE has thinned the ranks. I confine the discussion of these models to those that involve comets interacting with neutron stars, as this is the subject of the work in chapter 6.

First, however, it is worthwhile discussing the reasons why a Galactic neutron star origin for GRBs was favoured before the BATSE data, and whether it is still a possibility. An excellent review of this topic can be found in Lamb (1995), who discusses the arguments for a Galactic origin of GRBs in the first of a pair of papers based on the Diamond Jubilee of the “Great Debate”; in the second paper, the cosmological argument is propounded by Paczyński (1995).

### 4.1 *A Galactic Origin for GRBs*

Before that BATSE results, which show the remarkably isotropy of bursts on the sky, the general consensus was that the source of GRBs was neutron stars in a thick Galactic disk, and that we were probing only to relatively small distances (a few hundred pc). It was only reluctantly that sentiment began to move to a cosmological origin as the new, seemingly incontrovertible, data came out.

It is possible to imagine scenarios where GRBs are created on neutron stars around the Galaxy, but the disk origin must be discarded. The combination of isotropy on the sky, meaning the bursts are very far away or very close, and the observed deficit of weak bursts, suggesting that we are seeing to the edge of the distribution, makes a disk origin effectively ruled out: if we could see to the edge of a disk distribution, the disk would become obvious

in the distribution on the sky.

#### 4.1.1 Matching the Distribution on the Sky

The remaining alternative for Galactic GRBs is neutron stars in an extended halo around the Galaxy. The length scale for the halo, presumably symmetric about the Galactic centre, would have to be much larger than the distance from the Earth to the Galactic centre for the bursts to appear isotropic.

This can be demonstrated with a simple model of a burster distribution. Take the distribution to be homogeneous in a sphere around the Galactic centre with radius  $R$ . If we examine this distribution offset from the Galactic centre by a displacement  $R_0\hat{x}$ , the dipole statistics described in chapter 2 are given by

$$\begin{aligned}
\langle \cos \theta \rangle &= \langle \hat{r}' \cdot (-\hat{x}) \rangle \\
&= \frac{3}{4\pi R^3} \int_{\vec{r}} \left( \frac{\vec{r}' \cdot (-\hat{x})}{|\vec{r}'|} \right) d^3r \\
&\simeq \frac{R_0}{R} \\
\mathcal{W} &= 3 \langle \hat{r}'_1 \cdot \hat{r}'_2 \rangle \\
&= 3 \left( \frac{3}{4\pi R^3} \right)^2 \int_{\vec{r}_1} \int_{\vec{r}_2} \frac{\vec{r}'_1 \cdot \vec{r}'_2}{|\vec{r}'_1| |\vec{r}'_2|} d^3r_1 d^3r_2 \\
&\simeq 3 + 3 \left( \frac{R_0}{R} \right)^2
\end{aligned}$$

where  $\vec{r}' = \vec{r} - R_0\hat{x}$  is the distance to the burst in a coordinate system centred around the Sun. These estimates are valid in the limit where  $R_0 \ll R$ , such that  $|\vec{r}'| \simeq |\vec{r}|(1 - \vec{r} \cdot R_0\hat{x})$ . This is a nice example of how the coordinate-dependent tests are more sensitive to variations than the coordinate-independent tests when the anisotropy breaks the coordinate symmetry. The quadropole statistics are, of course, zero for this distribution, as there is no clumping toward the disk, or toward any other plane.

To be within the  $\pm 0.017$  uncertainty on the  $\langle \cos \theta \rangle$  value for the BATSE distribution,  $R_0/R < 0.017$ , or  $R > 470$  kpc. A halo of this radius is much larger than even postulated

dark matter halos, and is large enough that an equivalent halo from M31 would overlap with ours, and we might expect to see a clustering of bursts in its direction. This is not observed in the data.

It is possible to shrink this radius somewhat by altering the distribution - making a cored distribution, for example, with no bursts within a radius  $R_{\min}$  would reduce the estimate of  $\langle \cos \theta \rangle$  to

$$\langle \cos \theta \rangle = \frac{R_0}{R} \left[ \frac{1 - \left(\frac{R_{\min}}{R}\right)^2}{1 - \left(\frac{R_{\min}}{R}\right)^3} \right] \quad (4.1)$$

which approaches  $\frac{2}{3} \frac{R_0}{R}$  in the limit of  $R_{\min} \rightarrow R$ , reducing the required halo size to  $> 310$  kpc.

This is not as unlikely as it might first seem. The observed pulsar birth velocity distribution, re-examined by Lyne & Lorimer (1994), shows that neutron stars which become pulsars have very high velocities. The distribution has a peak near 225 km/s and a long tail to high velocities, giving an average pulsar birth velocity of 450 km/s. This is comparable to the escape velocity from the Galactic disk outside a few kpc of the centre, and means that a significant fraction of pulsars may have high enough velocities to populate a large halo.

Long-wavelength radio observations of pulsars have also linked several of these objects to young supernova remnants (SNRs), and suggest that the stars can sometimes have extremely high velocities (Frail *et al* 1994). Figure 4.1 shows a false-colour radio map of the “duck” SNR and PSR 1757-24. Age estimates of the nova coupled with a relatively well-determined distance suggest that the pulsar speed is between 1300 km/s and 1700 km/s, which leaves this object unquestionably unbound from the Galaxy’s potential well.

Unfortunately, a significant fraction of these stars also remain trapped in the potential well of the Galaxy and orbit at radii less than the distance to the Sun. These stars, if they become bursters, should make the GRB distribution significantly clumped toward the Galactic centre. There are several ways around this problem: the low-velocity stars may not become bursters, or the bursts may be beamed strongly along the star’s velocity vector.

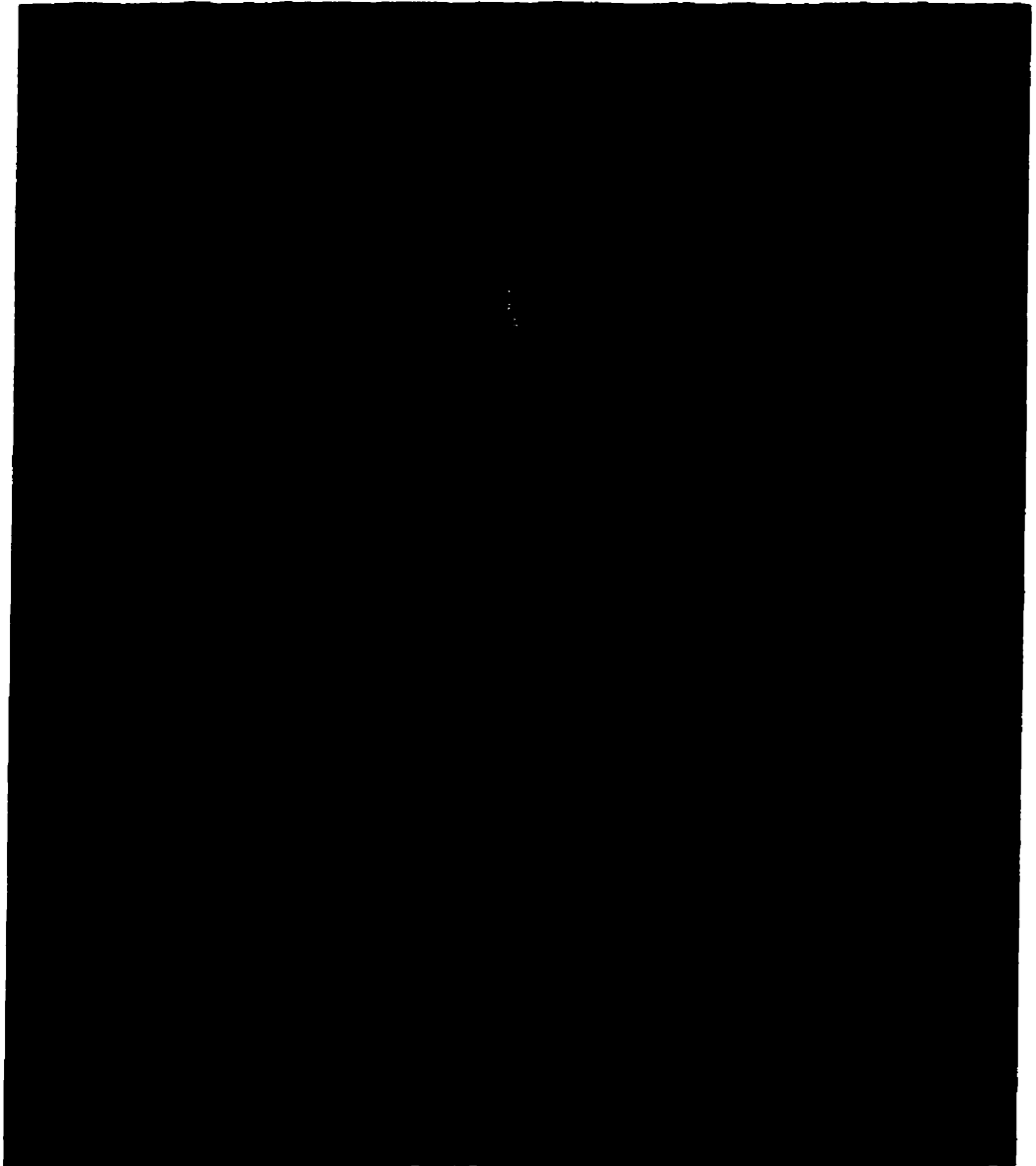


**Fig. 4.1:** False-colour long-wavelength radio map of the “duck” SNR (G5.4-1.2) and the pulsar PSR 1757-24. Estimates of the size and age of the SNR suggest that the pulsar has a velocity of at least 1300 km/s away from the disk of the Galaxy, which leaves it completely unbound from the Galaxy’s potential well.

This beaming means that stars closer to us have a smaller chance of being observed, simply because the cones of their emission have a smaller probability of including the Earth, and also alleviates possible problems with clumping of observed sources toward Andromeda (Duncan *et al* 1993).

Including a minimum time before which a star cannot become a GRB also may alleviate the problem of clumping toward the Galactic centre, and having only high-velocity neutron stars become bursters means that there will be no significant clumping of the GRBs to the Galactic disk. There are therefore several models of Galactic GRB sources which are still viable (e.g., Li & Dermer 1992, Podsiadlowski *et al* 1995).

However, making GRBs Galactic requires a somewhat uncomfortable amount of fine-tuning the parameters involved in the model, which are often numerous. This is why sentiment is now turning to favour a cosmological origin of these objects. Before the BATSE data, though, a neutron star origin was strongly favoured. There are good reasons for this, which are worth discussing.

#### *4.1.2 Factors in Favour of a Neutron Star Origin*

All we know about neutron stars comes from pulsar observations and stellar evolution theory. However, the observations have given a wealth of information which characterises these objects rather well. The similarities with GRB observations were the main reasons for the belief that these objects are associated with neutron stars.

#### *Photon energy*

The typical photon energies from GRBs are on the order of hundreds of keV to MeV. Gamma-ray pulsars generally radiate at somewhat higher energies, in the 100 MeV to GeV range, but give off significant power at MeV energies. If the GRB sources are old pulsars which have spun down to lower angular speeds, the expected photon energy also drops as the electric fields generated in the neutron star magnetosphere decline.

The spectrum of GRB radiation is also somewhat similar to pulsar spectra, in that both are decidedly non-thermal. It is difficult to give an example of a “typical” pulsar gamma-ray spectrum (see chapter 3), but they are generally fairly hard power-law spectra, in rough agreement with the GRB spectra.

### *Temporal structure*

Variations in the emission from GRBs have been observed down to the scale of tens of milliseconds. From light travel time, this implies a source size of less than about  $10^8$  cm, which suggests a compact star origin for these objects (unless the variability is somehow intrinsic to the burst physics, which is certainly feasible - see, for example, Babul, Paczynski, & Spergel 1987, for a model involving superconducting cosmic strings which gives rapid variability).

Similar variations are seen in the gamma-ray light curves of pulsars which have been measured to these levels - see, for example, the Crab, Vela, and Geminga light curves in figure 3.1. This coincidence in temporal structure also suggests the neutron star origin.

### *Burst energies*

The total energy stored in the electromagnetic field of a pulsar can roughly be estimated from the energy stored in a dipole magnetic field, where the minimum radius  $a$  is the stellar radius of 10 km:

$$E_{\text{tot}} = \frac{\mu^2}{3a^3} \simeq 3 \times 10^{41} \text{ergs} \left( \frac{\mu}{10^{30} \text{G} - \text{cm}^3} \right)^2 \left( \frac{10^6 \text{cm}}{a} \right)^3 \quad (4.2)$$

A burst at a radius of 100 kpc, if it gives a flux at the Earth of  $10^{-6}$  ergs/s/cm<sup>2</sup> for 1 sec and beams equally into the full solid angle, has an energy of  $2 \times 10^{42}$  ergs. The relatively close coincidence between these values is also somewhat leading. It is difficult, however, to imagine a process which would extract *all* the energy from the magnetic field, or even a significant fraction of it. This is not necessarily prohibitive, however, since bursters may be

naturally high-magnetic field objects, and only release a small fraction of the stored energy in a burst. In addition, the energy stored in the form of rotational kinetic energy can be as large as  $5 \times 10^{44}$  ergs for a star spinning with an angular velocity of 1 rad/s; this could easily be the source for the burst energy.

Unfortunately, a similar numerical coincidence occurs for cosmological bursts, where the total energy required for a burst ( $10^{52}$  to  $10^{53}$  ergs) is comparable to the gravitational binding energy of a solar-mass star.

### *Line features*

Prior to the launch of the BATSE telescope, several gamma-ray observations of GRBs suggested line features which were readily attributable radiation physics in the teragauss magnetic fields expected near the surface of neutron stars (see section 2.5). Such features are often observed in the spectra of x-ray pulsars (see, for example, Shrader & Gehrels 1995).

This was taken as a strong confirmation that GRBs were Galactic objects, as it is difficult to imagine a scenario involving narrow line emission in a cataclysmic collision. Line-like features can, however, be generated not by the source physics of a cosmological burst but by gravitational femtolensing by small ( $10^{-13}$  -  $10^{-16}$ ) dark matter objects (Gould 1992). In this model, the small path changes induced by the lens cause interference patterns in the spectrum at frequencies determined by the mass and size of the object, and can be consistent with the early line observations (Stanek *et al* 1993).

Early models for line creation in a Galactic GRB considered a plane-parallel plasma threaded by a perpendicular magnetic field (e.g., Preece & Harding 1992). Line features were created by resonant Compton scattering (described in detail by Daugherty & Harding 1986), a circumstance in which the cross-section for Compton scattering of photons off electrons or positrons is greatly enhanced for some photon energies when a strong magnetic field is present. Annihilation features were also naturally produced in the dense pair plasma created by pair cascades naturally produced in the strong surface fields of neutron stars. These initial



models assumed that the outward radiation force on the plasma had to be much less than the gravitational force, or else the lines would be washed out. This constraint meant that the maximum burst energy could only be of order  $10^{36}$  erg/s or less, constraining the GRB distance to  $< 100pc$ . Until the BATSE measurements, this was not considered to be a problem; however, the isotropy and flux distributions observed in these later data essentially ruled out a close, Galactic disk origin for the bursts.

Miller *et al* (1991) presented a model of narrow line formation in a relativistic, radiation-driven wind, and showed that the wind velocity itself is not responsible for line broadening, only the velocity dispersion and magnetic field variation. This model could reproduce the observed line features in GRBs and allows for bursts in a  $\simeq 100$  kpc halo to generate enough energy to be seen at the Earth.

### *Soft Gamma-Ray Repeaters*

The soft gamma-ray repeaters (SGRs) have been fairly conclusively linked to high-velocity neutron stars (Hurley *et al* 1994). While they are in general qualitatively different than classical GRBs (their spectrum is thermal and at significantly lower energy, they have been observed to repeat, and are generally associated with very young rather than very old stars), it is powerful evidence that a high-velocity neutron star can produce at least a kind of gamma-ray burst.

In addition, the SGRs may not be entirely different than classical GRBs. The most famous SGR, the March 5, 1979 event (which has now been observed to repeat 17 times, but never with the same spectral features as the initial burst), showed a powerful initial spike which has only been recently analysed (Fenimore *et al* 1996). The spectrum for the initial, sharp burst is entirely consistent with that of the classical GRBs; the only difference is the weak, pulsing and low-energy afterglow. BATSE has the sensitivity to have observed similar weak afterglows in more distant bursts, and has not seen any; however, the similarity between the initial spike in the March 5 event and the population of classical GRBs is

certainly suggestive.

## 4.2 Comet-Neutron Star Models

Generating GRBs by impacting comets or asteroids onto neutron stars was suggested very early in the study of these objects (e.g. Harwitt & Salpeter 1973, Shklovskii 1974). The first serious studies of the physics of such an encounter were done in the early 1980s by Newman & Cox (1980) and Colgate & Petschek (1981).

Both sets of authors recognised that a powerful magnetic field is required on the neutron star to create bursts which appear like those observed; with no magnetic field, the explosion on the surface expands and cools rapidly, giving small ( $< 10^{-3}$ ) efficiencies of energy conversion to gamma-rays, and burst times ( $\simeq 10^{-8}$  seconds) much shorter than those observed. A strong magnetic field contains the explosion along the field lines, reducing the cooling and extending the burst time.

These models typically only give rise to total energies on the order of  $10^{38}$  ergs, which is appropriate for a local Galactic disk model, but is several orders of magnitude too low to account for the required power of a Galactic halo GRB. The higher energies cannot be generated because the source of the energy is mainly the kinetic energy of the comet or asteroid rather than the larger store of energy in the neutron star electromagnetic fields.

A proposal which takes advantage of this energy source was originally suggested by Ruderman & Cheng (1988), where GRBs are the final stage of gamma-ray emission from pulsars. Their model is based on the original outer gap model of Cheng, Ho, & Ruderman (1986a,b); pulsars with period roughly shorter than 200 ms will generate pulsed gamma-ray emission, but stars which have spun down to longer periods can no longer generate the electron-positron pair flux to maintain the outer gap. However, an appropriate “spark” in the outer magnetosphere might re-initiate the pair cascade and cause brief emission of gamma radiation. Mitrafanov (1990) considered the potential of this model in some detail.

This model has the problem that the power generated can only be of order  $10^{36}$  to  $10^{38}$

ergs, which is far too low for a Galactic halo population. However, this source of gamma-ray generation only taps the fields in the outer magnetosphere, where the field strengths are much lower than near the stellar surface. A similar spark model applied to the inner magnetosphere has not been proposed, but the basic idea is not unreasonable.

## 5. EXISTING MODELS OF PULSAR GAMMA-RAY EMISSION

Before discussing our model of high-energy emission from pulsars, it is worthwhile discussing some of the other models which have been developed over the last twenty years, as well as a method for differentiating between the two groups of popular gamma-ray pulsar models which has not been discussed in the literature.

The basic physics involved in the gamma-ray emission from these objects is thought to be fairly well-understood, unlike the case of pulsar radio emission. The charges move in the ultra-high fields of the magnetosphere and radiate through three main mechanisms. There are only a few processes by which new charges and photons can be created or destroyed.

### *5.1 Radiation Processes in Ultra-High Fields*

There are only three radiation processes which are important in the pulsar magnetosphere, one of which is really a scattering process. However, as it effectively generates gamma radiation, it is included in the discussion as a radiation process.

#### *5.1.1 Synchrotron Radiation*

Classically, as a charge moves in a helical path around a magnetic field line, it gives off radiation due to its acceleration. This radiation was first observed in early synchrotron accelerators, and was termed synchrotron radiation. A charge moving in a circle around the field line (with no velocity component parallel to the line) can have any energy from zero to infinity, and the radiation is emitted at frequencies that are harmonics of a natural frequency  $w_0 = c/r$  (where  $r$  is the radius of the circular path) that is tied to the periodic nature of the charge path. For ultrarelativistic motion, the power is contained in very high harmonics,

and the spectrum looks roughly continuous (see Jackson 1975).

The quantum picture is somewhat different (for an excellent description of the physics and valid limits of the various treatments see Mészáros 1992). A charge moving in a circle around the field line can only have particular energies:

$$E = \hbar\omega_{\text{cyc}}n \quad (5.1)$$

where  $\omega_{\text{cyc}} = eB/(mc)$  is the classical cyclotron frequency. This effect becomes important in fields when the radius of the orbit (given by  $r = \lambda\sqrt{2n}$ , where  $\lambda = \sqrt{\hbar c/(eB)}$  is a characteristic radius) becomes of the same order as the deBroglie wavelength of the charge.

This is roughly equivalent to the condition that that  $\hbar\omega_{\text{cyc}}$  is equal to the charge rest mass energy, which determines a critical field

$$B_Q = \frac{m^2c^3}{e\hbar} = 4.413 \times 10^{13}\text{G} \quad (5.2)$$

where the quantum effects becomes important (at  $B = B_Q$ ,  $\hbar\omega_{\text{cyc}} = mc^2$ ).

As long as the charge energy is much larger than  $\hbar\omega_{\text{cyc}}$ , the classical picture works very well. However, in the very large fields of a pulsar magnetosphere (which can approach  $B_Q$  in some cases), quantum effects become important. Therefore, synchrotron radiation in these fields is well-approximated by jumps between these energy levels.

In general, high-energy charges in these fields radiate away synchrotron radiation very rapidly and sit in their lowest Landau level (moving parallel with the magnetic field line). An order-of-magnitude estimate of the timescale for synchrotron radiation can be derived from the classical picture (where synchrotron radiation is merely curvature radiation for a charge on a small circular path); the power radiated by synchrotron radiation in this limit is roughly

$$P_{\text{synch}} \simeq \frac{e^4}{m^2c^3}B^2\gamma^2 \quad (5.3)$$

where  $B$  is the local magnetic field strength and  $\gamma$  is the charge's Lorentz factor. Setting this equal to  $-\dot{\gamma}mc^2$ , the timescale for synchrotron radiation is

$$\tau_{\text{synch}} = \frac{m^3 c^5}{\gamma e^4 B^2} = 3.5 \times 10^{-23} \text{sec} \left( \frac{10^{12} \text{G}}{B} \right)^2 \left( \frac{10^7}{\gamma} \right) \quad (5.4)$$

which is much smaller than any other timescales in the pulsar magnetosphere. Even at the light cylinder, where the fields can be as small as tens of gauss for the slowest gamma-ray pulsars, the timescale is much smaller than the pulsar rotation period.

### 5.1.2 Curvature Radiation

Curvature radiation and synchrotron radiation, in the classical picture, are really two limits of the same physics (though curvature emission gives a continuous spectrum and synchrotron radiation emits in lines due to the periodic nature of the charge path). In synchrotron radiation, a charge radiates because it is forced into a curved path as it circles a field line. Curvature radiation is that from a charge moving along a curved magnetic field line; in this case, the charge path is curved not because of motion around the field line, but because the field line itself is not straight, and the charge is constrained to follow  $\vec{B}$ .

Jackson (1975) derives the radiation pattern from a charge moving in instantaneously circular motion on a path with radius of curvature  $\rho$ . The frequency distribution is given by:

$$\frac{dI}{d\omega} = 2\sqrt{3} \frac{e^2}{c} \gamma \frac{\omega}{\omega_c} \int_{2\frac{\omega}{\omega_c}}^{\infty} K_{5/3}(x) dx \quad (5.5)$$

where  $\omega$  is frequency (in units of rad/s),  $\omega_c = 3\gamma^3(c/\rho)$  (the characteristic frequency of emission), and  $K_{5/3}(x)$  is a modified Bessel function of order 5/3. For frequencies much less than  $\omega_c$ , this reduces to

$$\frac{dI}{d\omega} \simeq 3.25 \frac{e^2}{c} \left( \frac{\omega \rho}{c} \right)^{1/3} \quad (5.6)$$

and in the limit  $\omega \gg \omega_c$  becomes

$$\frac{dI}{d\omega} \simeq \sqrt{3\pi} \frac{e^2}{c} \gamma \left(\frac{\omega}{\omega_c}\right)^{1/2} e^{-2\omega/\omega_c} \quad (5.7)$$

These expressions are integrated over the angular pattern of the radiation; this is not important for high-energy charges, as the emission is beamed along the velocity vector with a typical pattern width of  $1/\gamma$ . Therefore, assuming that all the energy is beamed in a pencil-beam along the velocity is a good approximation for  $\gamma \gg 1$ .

The low-frequency limit of the radiation pattern has an intensity which increases like  $\omega^{1/3}$ , or a distribution in photon number which drops like  $\omega^{-2/3}$ .

The total power output, integrated across frequency and the radiation pattern, for a single charge in instantaneously circular motion is given by

$$P = \frac{2}{3} \frac{e^2 c}{\rho^2} \gamma^4 \quad (5.8)$$

and the typical photon energy is  $\hbar\omega_c$  (see section 8.1 for a derivation of this in the context of the radiation reaction force).

### 5.1.3 Inverse-Compton Radiation

This “radiation” process is really a scattering process, where low-energy photons scatter off high-energy electrons or positrons, and leave the interaction with much higher energy. Since the charges in the magnetosphere can have Lorentz factors as high as  $10^7$ , the photon energies created through inverse-Compton scattering can be as high as the TeV range.

The problem can be considered by examining relativistic scattering of a low-energy photon ( $E \ll m_e c^2$ ) by a high-energy charge (mass  $m_e$  and  $\gamma \gg 1$ ). Transforming to the rest frame of the charge changes the situation to a high-energy photon (with energy  $E' \simeq \gamma E$ ) scattering off a charge at rest. If the photon energy in the original (lab) frame is much less than  $m_e c^2/\gamma$ , the scattered photon will have relatively low energy as well; for photon energies (in the lab frame) in the range  $mc^2/\gamma \ll E \ll mc^2$ , the charge will share its energy roughly equally with the scattered photon.

Due to relativistic beaming, the scattered photon will be directed mainly along the charge's velocity vector, with a spread in angle roughly of order  $1/\gamma$ .

The physical scenario is shown in figure 5.1. The solution of the problem, given  $\theta$ ,  $\phi$ ,  $\gamma$ , and  $\lambda$ , is

$$\gamma' = \frac{\gamma^2 \phi^2}{2\lambda(1 - \cos \theta) + \gamma \phi^2} \quad (5.9)$$

$$\lambda' = \gamma \left( 1 - \frac{\gamma \phi^2}{2\lambda(1 - \cos \theta) + \gamma \phi^2} \right) \quad (5.10)$$

$$\alpha = \frac{2\lambda(1 - \cos \theta)}{\gamma \phi} \quad (5.11)$$

The cross-section for scattering is best viewed from the rest frame of the electron. In this frame, the cross-section for scattering a photon with energy  $E_{\text{ph}}$  much less than an electron rest mass energy is simply the Thompson cross-section  $\sigma_{\text{T}} = 6.7 \times 10^{-25} \text{ cm}^2$ . At photon energies much higher than  $m_e c^2$ , the cross-section is approximately (Jackson 1975)

$$\sigma \simeq \frac{3}{4} \sigma_{\text{T}} \frac{m_e c^2}{E_{\text{ph}}} \quad (5.12)$$

In the intermediate interval, where  $E_{\text{ph}} \simeq m_e c^2$ , interesting effects can become important in strong magnetic fields. When the photon energy is roughly equal to the cyclotron energy for charge motion around the field line, resonant effects can increase the cross-section for scattering enormously. This “magnetic” Compton scattering has important ramifications for charged particle motion near the pulsar surface, where the magnetic fields can approach  $B_{\text{Q}}$  (e.g., Sturmer 1995).

Lieu & Axford (1993) have shown that inverse Compton scattering and synchrotron/cyclotron radiation can be seen as the same process, where synchrotron radiation is the inverse Compton scattering of an equivalent photon field by the charge. This is discussed in more detail in section 8.1 in relation to the radiation reaction force.



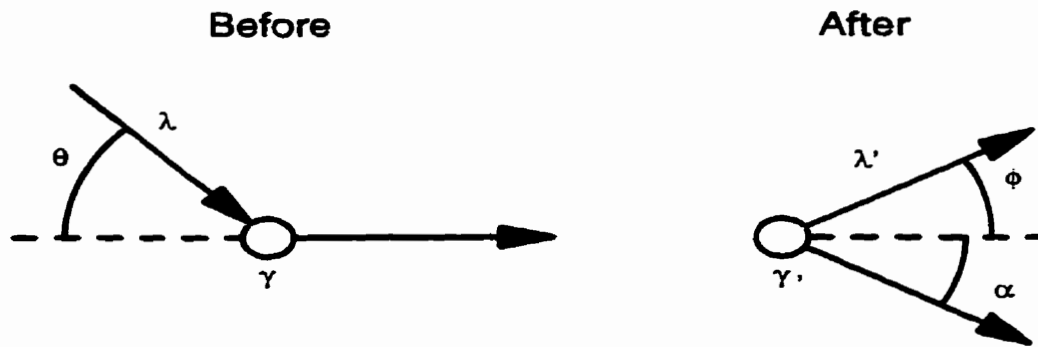


Fig. 5.1: An illustration of the inverse Compton scattering process. The photon energy before the collision is  $\lambda m_e c^2$ , and the electron energy is  $\gamma m_e c^2$ . The scattering angles  $\phi$  and  $\alpha$  are both much less than unity due to relativistic beaming. Inverse Compton scattering is distinguished from Compton scattering because the electron energy is much greater than the photon energy: after the collision, for  $1/\gamma \ll \lambda \ll 1$ , the charge shares its energy roughly equally with the scattered photon.

## 5.2 Scattering in Pulsar Magnetospheres

Pair creation processes are very important in modern pulsar magnetosphere models. There are only two processes which are significant in the typical fields and photon energies in the space around a pulsar:  $\gamma$ - $B$  pair creation, where a photon converts into an electron-positron pair on a powerful magnetic field, and  $\gamma$ - $\gamma$  scattering, where two photons scatter to create a pair. Other processes are somewhat important, though are generally negligible compared to these primary two routes to pair generation.

### 5.2.1 $\gamma$ - $B$ Pair Creation

It was recognised early on in pulsar physics (Sturrock 1971) that high-energy photons would create electron-positron pairs in the extremely high fields near the stellar surface. The mean free path of this process is extremely sensitive to the product of photon energy and magnetic field; if

$$\chi = \gamma \frac{B}{B_Q} \sin \theta > 1 \quad (5.13)$$

where  $\gamma$  is the photon energy in units of the electron rest mass energy and  $\theta$  is the angle between the photon velocity and magnetic field direction, then the mean free path for conversion of the photon into an electron-positron pair is extremely short. This is true for 100 MeV photons within a few stellar radii of the pulsar surface, but is not an important charge creation process in the outer magnetosphere where the magnetic fields are much smaller.

This process can generate a huge amount of charge through a cascade process, where a single photon generates an electron-positron pair, which are then accelerated to high energies by the electric fields. These high-energy charges radiate gamma-rays themselves, which produce more pairs. The process continues until the electric fields are shorted out, or some other steady state is reached.

### 5.2.2 $\gamma$ - $\gamma$ Pair Creation

Pairs can also be generated through interactions between a pair of photons, as long as the total energy is greater than twice the rest mass energy of an electron.

The cross-section for photon-photon pair creation is often approximated as

$$\sigma = \frac{\sigma_T}{3} \frac{(m_e c^2)^2}{E_{\text{ph-1}} E_{\text{ph-2}}} \quad (5.14)$$

for  $E_{\text{ph-1}} E_{\text{ph-2}} > (m_e c^2)^2$ , and zero for  $E_{\text{ph-1}} E_{\text{ph-2}} < (m_e c^2)^2$ , where  $E_{\text{ph-1}}$  and  $E_{\text{ph-2}}$  are the two photon energies (Cheng, Ho, & Ruderman 1988b). This form assumes head-on collisions between the photons.

The cross section then is maximally of order the Thompson cross section  $\sigma_T$ , and drops inversely with the product of the two photon energies.

This process can be important throughout the pulsar magnetosphere, as photon fluxes can be quite high for some models.  $\gamma$ - $\gamma$  pair creation is not important near the star for high photon energies ( $> 10 - 100$  MeV), as it is very much dominated by  $\gamma$ - $B$  pair creation.

### 5.2.3 Photon Splitting

Photons which have energies somewhat lower than that required to pair create on the magnetic field can instead split into two lower-energy photons (Adler 1971). In the limit of  $B \ll B_Q$ , the attenuation coefficient (the inverse of the mean free path) is approximately

$$R \simeq 0.37 \left( \frac{B}{B_Q} \right)^6 \left( \frac{E_{\text{ph}}}{m_e c^2} \right)^5 \quad (5.15)$$

This can be important in pulsar radiation models where the generation of the radiation occurs near to the stellar surface (as the mean free path is very long for the smaller magnetic fields in the outer magnetosphere). However, it generally affects only a small energy range, and is usually neglected in radiative calculations.

#### 5.2.4 Triplet Pair Production

A photon can pair-produce not only on an external magnetic field, but also on the Coulomb field of an electron. The process then is

$$\gamma + e^- \rightarrow 2e^- + e^+ \quad (5.16)$$

Mastichiadis (1991) examines this effect in terms of gamma-ray spectra. Even though it is a third-order QED process, the cross-section can exceed the Compton cross-section for high collision energies. In general, however, triplet pair production is a relatively unimportant process in the generation of pulsar gamma radiation.

### 5.3 Pulsar Gamma-Radiation Models

Gamma-ray emission models can be roughly sorted into two categories: polar cap models, where the radiation is generated near the polar caps of the pulsar in the  $10^{12}$  G fields, and outer gap models, where the emission comes from charges radiating farther out in the magnetosphere, at distances from the star on the order of the light cylinder radius. The observations so far have not been able to differentiate between these two basic models, as the observed light curves and spectra are quite varied, and neither model is entirely successful at describing them.

Our model (see chapter 9) falls into the category of the outer gap models, as the charge acceleration and radiation is generated relatively far out from the star (at radii  $r > 0.1R_{lc}$ ).

#### 5.3.1 Vacuum Birefringence as a Model Test

To differentiate between the models, there must be a robust consequence of the different physics that is testable. One possibility which has not been examined in the literature is “vacuum birefringence”, an effect where the effective indices of refraction for photons travelling with polarisations parallel and perpendicular to the plane formed by the magnetic field and the photon velocity can be different (Tsai & Erber 1975):

$$n_{\parallel} \simeq 1 + \frac{\alpha}{4\pi} \sin^2 \theta \left[ \frac{14}{45} \left( \frac{B}{B_Q} \right)^2 - \frac{13}{315} \left( \frac{B}{B_Q} \right)^4 \right] \quad (5.17)$$

$$n_{\perp} \simeq 1 + \frac{\alpha}{4\pi} \sin^2 \theta \left[ \frac{8}{45} \left( \frac{B}{B_Q} \right)^2 - \frac{379}{5040} \left( \frac{B}{B_Q} \right)^4 \right] \quad (5.18)$$

where  $\alpha$  is the fine structure constant,  $\theta$  is the angle between the photon velocity and the magnetic field direction, and  $B_Q$  is the critical field discussed in section 5.1.1. These expressions are valid for  $B < 0.1B_Q$  to better than 0.05%. The different indices of refraction lead to different photon speeds; if a parallelly- and perpendicularly-polarised pair of photons travel far enough, the lag will be equal to a wavelength. The lag over a distance  $dx$  is given by

$$dl = \Delta v \frac{dx}{c} \simeq \frac{6}{45} \frac{\alpha dx}{4\pi} \sin^2 \theta \left( \frac{B}{B_Q} \right)^2 \quad (5.19)$$

If this lag is much larger than the photon wavelength, the photons will show no bulk polarisation. Assuming a magnetic field which varies as  $B = B_s(R/r)^3$  (with  $B_s$  equal to the surface field and  $R$  equal to the stellar radius), the lag for a photon created at radius  $r$  and travelling to infinity is roughly

$$l(r) \simeq \frac{3}{45} \frac{\alpha R}{4\pi} \left( \frac{B_s}{B_Q} \right)^2 \left( \frac{R}{r} \right)^5 \quad (5.20)$$

Taking a surface field of  $B_s = 10^{12}$  G, the radius inside which the lag is greater than the photon wavelength is

$$r = 4.4 \times 10^7 \text{ cm} \left( \frac{E}{1 \text{ MeV}} \right)^{1/5} \quad (5.21)$$

The very strong magnetic fields near the stellar surface will induce a rapid polarisation shift in gamma-ray photons with energies below the pair creation threshold, leaving no significant bulk polarisation (this has been discussed in the framework of x-ray emission from x-ray binaries and pulsars by Novick *et al* 1977).

Vacuum birefringence is strongly dependent on magnetic field strength, and therefore will not be a factor in models where the emission is produced in the outer magnetosphere. The cut-off radius of equation 5.21 is less than  $0.1R_{lc}$  for pulsars with angular velocities greater than  $\Omega = 70$  rad/s, which is true for the older gamma-ray pulsars.

If significant linear polarisation is observed in pulsar gamma-ray light curves, this will be a very strong argument against the polar cap-type models in general (though vacuum birefringence may be important for outer gap emission in very young pulsars). Significant linear polarisation is expected from curvature and synchrotron emission (Jackson 1975), though not necessarily from inverse Compton radiation. No current gamma-ray telescopes can detect photon polarisation, but the proposed GLAST telescope may allow polarisation measurements of gamma-ray photons.

### 5.3.2 Polar Cap Models

Polar cap models involve the acceleration of charges from the stellar surface or from  $\gamma - B$  pair creation by electric fields in a gap above the star which extends to distances of roughly a stellar radius above the polar cap. Pair-creation effects are extremely important in these models due to the very short mean free path of photons which satisfy the  $\gamma - B$  pair-creation criterion (equation 5.13).

The recent polar cap models have been separated into two camps: models where the primary gamma radiation mechanism is curvature radiation, and those where the charge energies are somewhat lower, and the dominant source of high-energy photons is inverse Compton scattering of thermal photons from the star.

Both sorts of model are similar in spirit. Charges are ejected from the polar cap and follow the magnetic field lines very closely, as perpendicular momentum is quickly radiated away through synchrotron radiation. They are accelerated by an electric field component parallel to the magnetic field line, and lose energy through a variety of different processes. Following Daugherty & Harding (1996), the energy of a relativistic charge following a field

line obeys the one-dimensional equation of motion

$$\frac{d\gamma}{ds} = \frac{1}{c} \left[ \left( \frac{d\gamma}{dt} \right)_{\text{acc}} - \left( \frac{d\gamma}{dt} \right)_{\text{cr}} - \left( \frac{d\gamma}{dt} \right)_{\text{cs}} - \left( \frac{d\gamma}{dt} \right)_{\text{other}} \right] \quad (5.22)$$

where  $s$  is the distance along the field line, “acc” represents acceleration mechanisms (the electric field), “cr” represents curvature radiation, “cs” inverse Compton scattering losses, and “other” various other scattering processes, such as triplet pair production.

The curvature radiation term has been discussed already in section 5.1.2; it is given by

$$\left( \frac{d\gamma}{dt} \right)_{\text{cr}} = \frac{2}{3} \frac{e^2}{mc} \frac{\gamma^4}{\rho^2} \quad (5.23)$$

where  $\rho$  is the local radius of curvature of the magnetic field line (known analytically).

The inverse Compton scattering energy losses can be found by integrating over all incident photon energies and angles; the general expression, following Sturmer (1995), is

$$\left( \frac{d\gamma}{dt} \right)_{\text{cs}} = c \int_0^\infty d\epsilon \int_{\text{polarcap}} d\Omega n_{\text{ph}}(\epsilon, \Omega) (1 - \beta \cos \chi) \int_0^{\epsilon'_s} d\epsilon'_s \oint d\Omega'_s \left( \frac{d\sigma}{d\epsilon'_s d\Omega'_s} \right) (\epsilon_s - \epsilon) \quad (5.24)$$

where quantities with an “s” subscript relate to the scattered photon and primed quantities to those in the electron rest frame.  $n_{\text{ph}}(\epsilon, \Omega) d\epsilon d\Omega$  is the density of incident photons with energies between  $\epsilon$  and  $\epsilon + d\epsilon$  and within solid angle  $d\Omega$  from direction  $\Omega$ .

The scattering cross-section contains three terms, the so-called angular, nonresonant, and resonant contributions. The resonant contribution comes from photons which have energies in the charge rest frame equal to the local cyclotron energy, where the cross-section is increased dramatically.

Sturmer (1995) derives approximate expressions for the inverse Compton scattering deceleration from the angular, nonresonant, and resonant contributions which are given analytically in terms of the height  $h$  above the polar cap, the temperature  $T$  of the polar cap, and the surface magnetic field strength  $B$ .

Both Sturmer (1995) and Daugherty & Harding (1996) consider only triplet pair-production for contributions under “other”, where an incoming electron scatters off an electron to create an electron-positron pair. Both groups show that this term is generally negligible for gamma-ray pulsar parameters.

The curvature radiation and inverse Compton scattering terms dominate the energy loss in different regimes. For large Lorentz factors, the curvature radiation losses are generally the most important; these arise when the polar cap is not very hot, or the electric fields are large.

Sturmer, Dermer, & Michel (1995) consider the case of relatively low accelerating electric fields and high polar cap temperature, when the dominant energy loss mechanism is inverse Compton scattering, enhanced by the resonant Compton scattering in the strong magnetic fields (which is also the dominant contribution to the emergent gamma-ray spectrum). Charges are accelerated along the field lines and radiate gamma-rays through inverse Compton scattering along their velocities, creating a hollow cone of emission. An observer with a line of sight that cuts the cone at various angles can see a singly- or doubly-peaked light curve, though the angle of inclination of the magnetic dipole moment must be quite small.

Daugherty & Harding (1996) consider the case of large electric fields, where the curvature term is dominant. Their model is similar to the last one, where charges are accelerated along the field lines and give off curvature photons to produce a hollow cone of emission while producing pairs on the strong magnetic fields. They Monte Carlo-simulate charges started near the star in various (assumed) electric fields, and follow the charge and photon creation numerically to develop the emergent spectra.

These two polar cap models are generally quite similar in the generated light curves (if not in spectra): the peaks in the light curves occur as the line of sight cuts the hollow cone of emission. The light curves can only be singly- or doubly-peaked; however, there is evidence of a triply-peaked light curve with PSR 1706-44 (Thompson *et al* 1995a).



These models predict no emission over a significant fraction of the pulsar period. Recent observations suggest the opposite (Nolan *et al* 1996).

### 5.3.3 Outer Gap Models

Models for generating pulsar gamma-ray emission in the outer magnetosphere have a long history. Early models considered acceleration near the light cylinder to be important (da Costa & Kahn 1982). The acceleration came from a “slingshot” effect, where the charge drift went to  $c$  on certain surfaces, rapidly increasing the energy of the particles so that they gave off curvature gamma radiation.

Later models turned to using deviations from the Goldreich-Julian charge density at various locations in the magnetosphere to create large electric field components parallel to the local magnetic field. These components accelerated charges to very high energies, where the three radiation mechanisms mentioned earlier become important.

The basis of the modern outer gap models is a pair of papers written in 1988 (Cheng, Ho, & Ruderman 1988a and 1988b), where the basic model was elucidated.

The starting point of the outer gap model is an assumed current structure in a magnetosphere which is full of Goldreich-Julian charge density. There is no physical motivation for this current pattern; it is taken that a magnetosphere filled with Goldreich-Julian charge density would begin to circulate as assumed, and the validity of the model predictions give the justification. Figure 5.2 shows this magnetosphere model.

This current distribution has the property that, near the boundary between positive and negative charge density (a surface where  $\vec{\Omega} \cdot \vec{B} = 0$ ), growth of charge-deficient gaps is unstable. The charge deficit creates large electric fields in the gaps which can accelerate charges to high energies and emit gamma-rays.

Since these generated gamma-rays can pair create on one another, they will tend to close up gaps farther out in the magnetosphere. However, the structure of the dipole field lines means that a gap along the boundary of the last open/closed magnetic field line will not be

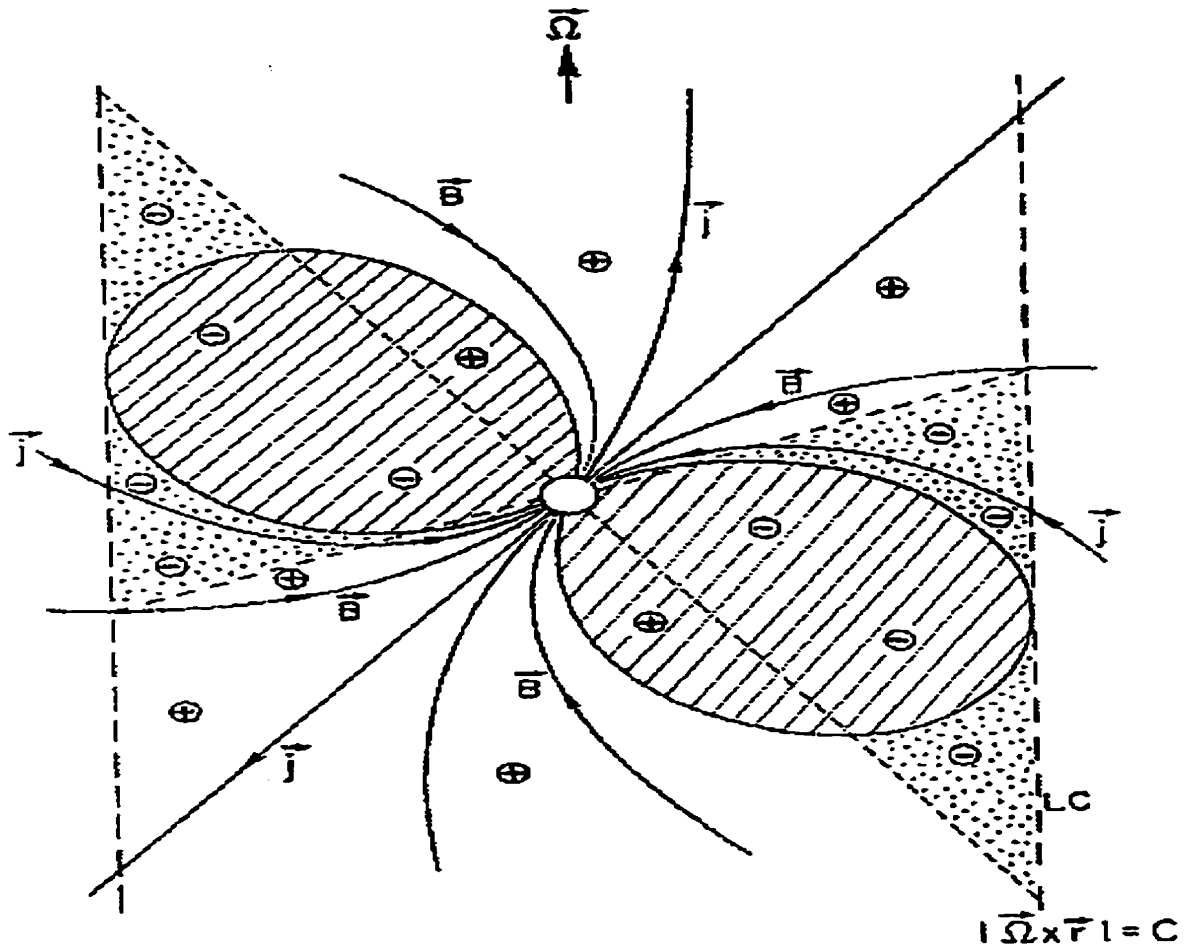


Fig. 5.2: The current structure in the early outer gap model of Cheng, Ho, & Ruderman (1988a) (their Figure 1). The current structure is not the result of any basic physics; it is assumed that a magnetosphere, started with space filled with the Goldreich-Julian charge density everywhere, would begin to circulate as show. This current structure creates unstable growth of gaps near the boundary between the positive and negative charge density regions (separated by the  $\vec{\Omega} \cdot \vec{B} = 0$  surface).

closed due to gamma emission closer in, and will be stable. There are two of these gaps, travelling from well within the light cylinder near the poles to the light cylinder.

The gap increases in size until its growth is checked by pair creation near the boundary, and a steady-state is approached. The boundary layer has a low value of  $\vec{E} \cdot \vec{B}$  due to the creation of “secondary” charges from pair creation due to the gamma-ray emission of the initial charges inside the gap; these secondary charges still have high energy, however (due to the high energy of the incident photons), and pair create further out, making “tertiary” charges with relatively low energies. The tertiary charges radiate mainly through weak synchrotron emission and flood the gap with a low-energy photon flux.

Curvature radiation and inverse Compton scattering are both important processes inside the gap, as the charges have quite high energies, and the tertiary charges create a flux of low-energy photons in the gap.

This early model assumed that the gap was a single region, with characteristic values of photon flux and magnetic field. However, it could still give a relatively good fit to the observed Crab and Vela pulsar spectra.

The light curves generated from the early outer gap model were almost always doubly-peaked, as the two outer gaps radiated fan-shaped beams of radiation both of which pass through most viewing angles. This was not a problem in 1988, when Crab and Vela were the only known gamma-ray pulsars, but with increasing data showing several singly-peaked light curves, this early model was significantly challenged.

Chiang & Romani (1994) extended the original calculation by removing some of the simplifying approximations. In particular, they modelled the gap not as a single zone with a characteristic magnetic field and photon flux (which is difficult to justify when the gap spans a significant distance radially), but as a number of sub-zones which interact self-consistently.

The shape of the gap was altered by allowing gaps to form along all field lines on the boundary between the open and close field line regions (as opposed to only the field lines in the plane formed by  $\vec{\Omega}$  and  $\vec{\mu}$ ), and particle and photon transport between the gap emission

zones was included. These changes allowed for singly-peaked light curves for some viewing angles, making the model consistent with the newer observations, though the modelling of the spectra suffered somewhat. In the case of the Crab pulsar, which had been relatively well-modelled in the earlier effort, the model spectrum had far too few low-energy photons.

As with the polar cap models, the outer gap models produce singly- or doubly-peaked light curves only and predict no emission for a significant fraction of the pulsar period, neither of which agree with observations.

## 6. DISTRIBUTION OF GAMMA-RAY BURSTS IN HALO NEUTRON STAR-COMET MODELS

### 6.1 *Introduction*

There have been many models over the years which try to identify gamma-ray bursts (GRBs) with neutron stars (NSs) in an extended Halo around the Galaxy which interact in some way with passing comets (e.g. Pineault and Duquet 1993 or Mitrofanov and Sagdeev 1990). The details of the environment which would allow such a scenario involving interstellar comets have not been worked out in detail.

It has been estimated that approximately  $10^{12}$  comets have escaped the Sun's gravitational well (Stern 1990) over the age of the solar system. If other solar systems behave in a similar manner, there should be a large number of free comets in globular clusters (GCs), which, after escaping the clusters by scattering, could seed an extended Halo.

This work evolved a population of  $10^6$  NSs born in the disk. It also evolved  $10^7$  comets ejected from GCs, and assumed a population of disk comets which follow the mass density of the disk. Using these results, samples of GRBs were created.

### 6.2 *The Model of Galactic Potential*

The model used was taken from Paczynski (1990), with some modifications. It assumes three contributions to the total potential: a disk, a spheroid, and a spherical dark matter halo. The values used for the constants in his model, relating to the oblateness of the spheroid ( $a_1$  and  $b_1$ ) and disk ( $a_2$  and  $b_2$ ), are:  $a_1 = 0$ ,  $b_1 = 0.277$  kpc,  $a_2 = 3.7$  kpc, and  $b_2 = 0.2$  kpc. A dark matter halo with constant density inside a radius  $r_c = 8$  kpc, and density falling off like  $r^{-2.25}$  outside  $r_c$ , replaced Paczynski's halo. The masses used are:  $M_1 = 1.12 \times 10^{10} M_\odot$

(the spheroid mass),  $M_2 = 8.07 \times 10^{10} M_\odot$  (the disk mass),  $M_c = 1.75 \times 10^{10} M_\odot$  (the dark halo mass inside  $r_c$ ).

Other components contributing to the Galactic potential, such as satellite galaxies or the globular cluster population, were ignored for simplicity. Over the course of the simulation, roughly 10 % of the comets would be affected by such objects; this is not expected to change the results to any great degree. In addition, it is assumed that the Galactic dark matter does not interact with the comets to any appreciable degree. This assumption would fail if the dark matter is mainly molecular clouds, for example.

### 6.3 The Three Populations

The GC population comets were ejected from the GC stellar systems with small relative speeds. A small fraction of these comets escaped from the GC without scattering; however, a much larger fraction were scattered by stars in the GC (for simplicity, all scattering stars were taken to have a mass  $M_\odot$ ), and were ejected from the GC with speeds approximately 10-20 km/s. The distribution in velocity of these objects is shown in figure 6.1; the points are the real distribution generated from  $10^6$  ejected comets, and the solid line is an analytic fit used for simplicity, of the form

$$\frac{dn}{dv} = v \exp[3 \times 10^{-3}(v + 10.77)^2] \quad (6.1)$$

where  $v$  is the velocity in units of km/s (the plot has been scaled vertically to best fit the data points). The velocities of the GCs are typically much higher than these escape velocities, and the comets remain close to their parent clusters for a significant fraction of the integration time.

140 typical GCs were used in the simulation. The GC population was found by assuming a radial distribution which falls off like  $r^{-0.85}$  (Kulesa and Lynden-Bell (1992)), and a velocity distribution with gaussian form, with average value  $v_0 = 220 - 2r_{\text{kpc}}$  km/s, and standard deviation  $\sigma = 120 - r_{\text{kpc}}$  km/s, to roughly match the observed variation. Here,  $r_{\text{kpc}}$  is the

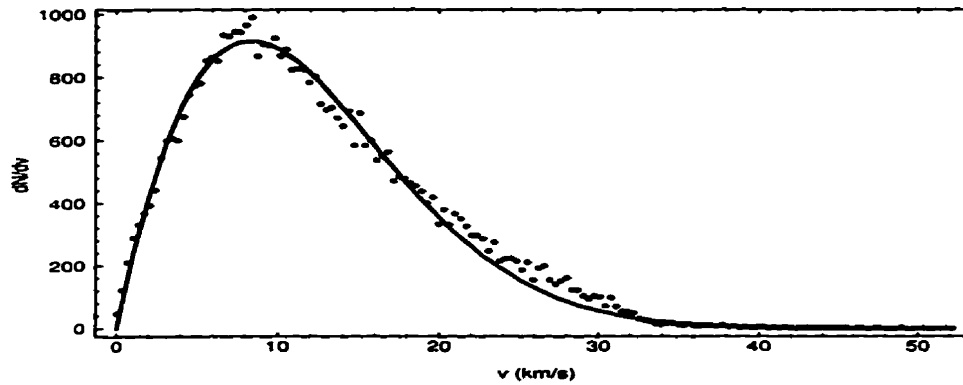


Fig. 6.1: The distribution of comets ejected from a  $10^5 M_{\odot}$  GC in velocity. The comets leave the cluster and are placed in the Galactic halo with a randomly oriented velocity sampled from this distribution, plus the space velocity of the parent GC. The points are the real distribution generated from  $10^6$  ejected comets, and the solid line is an empirical fit.

radial distance from the centre of the Galaxy in kpc, allowed to range from 6-110 kpc. Each GC was taken to have mass  $10^5 M_{\odot}$ , and the Plummer model, with a radial distance scale of 1 pc, was used for the gravitational potential. A variation of these parameters does not affect the results unduly, as a change only affects the small relative velocity of the comets to the GC.

The distribution of comets in space at the end of the simulation (after five billion years) is quite close to radially symmetric, as the comets created in the halo feel little of the disk potential. Figure 6.2 shows the radial distribution of comets. Inside 100 kpc, the distribution roughly follows a power law with index 0.88 (shown as the superimposed line), corresponding to a comet density which falls off like  $r^{-1.12}$ , since the distribution is roughly spherical. The bumps on the distribution correspond to clumps of comets near their parent GCs.

The disk population of comets was taken to follow the disk component of the total density. The total number of disk comets was set to the total number of GC comets multiplied by the ratio of the disk mass to the total mass of GCs, and a factor  $f$  (one of the free parameters in the work), which is a ratio of the efficiencies of comet ejection in the disk to comet ejection in the GCs.

The NSs were started in the disk, with a position distribution which follows the observed pulsar distribution, taken from Johnston (1994). Different distributions of initial speeds considered ranged from roughly 450 km/s to 2000 km/s in a frame of reference rotating around the Galactic centre with the circular velocity at that point.

The NS space distributions at the completion of the simulations generally were clumped toward the disk, with more spherically symmetric distributions at higher velocities as is expected. Figure 6.3 shows the radial distribution (with radius measured from the Galactic centre) of NSs for three different birth velocity distributions. The black points correspond to NSs started with a velocity distribution following the observed pulsar distribution as derived by Lyne & Lorimer (1994), where the distribution has the form



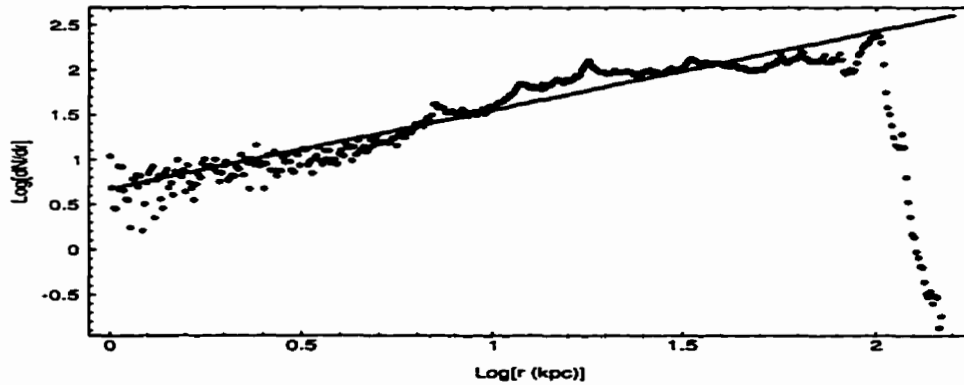


Fig. 6.2: The radial distribution of halo comets at the end of the simulation. The distribution shows several bumps, representing clumps of comets near their parent GCs. The edge of the distribution corresponds to the edge of the GC distribution, near 100 kpc. Inside this radius, the distribution roughly follows a power law with index 0.9, shown by the line superimposed on the data; this trend corresponds to a comet density which falls off like  $r^{-1.1}$ .

$$dn(v) = ve^{-v/v_0} \quad (6.2)$$

where  $v_0$  is the velocity scale, fit to 450 km/s from pulsar observations. The initial peak corresponds to the peak in the spacial birth distribution at roughly 3kpc; inside this radius, the density drops off like  $r^{-0.6}$ , and outside like  $r^{-3.5}$  (the density power law index for a spherical distribution is just  $\alpha - 2$ , where  $\alpha$  is the power law of the radial number number distribution shown). The distribution inside several hundred kpc is strongly peaked toward the disk. At large radii ( $\gg 100$  kpc), the density drops off like  $r^{-2.6}$ , where the distribution turns spherical again.

The blue points correspond to a birth distribution equal to the observed pulsar birth velocity distribution, but with  $v_0 = 700$  km/s rather than 450 km/s. A significant fraction of the stars escape the Galaxy's potential well, though there are still a large number of bound objects near the Galactic centre.

The red points correspond to NSs born with a birth velocity of 700 km/s; the distribution follows a power law with index 0.1 inside several hundred kpc and is strongly peaked toward the disk; at very large radii, the distribution follows a power law with index -0.4, corresponding to a density which varies like  $r^{-2.4}$ . There are not many stars near the Galactic centre, as none of these objects are bound to the Galactic potential well.

NSs born with a velocity of 2000 km/s are shown as the green data points. The distribution follows an  $r^{-2}$  power law almost exactly, as the stars are moving with velocity much larger than the escape velocity from the Galaxy.

#### 6.4 *Estimating the Interaction Probability*

The probability of interaction between the NS and comet populations was taken to be (e.g. Pineault and Poisson (1989))

$$P = \frac{An_{ns}n_c}{v_{rel}} \quad (6.3)$$

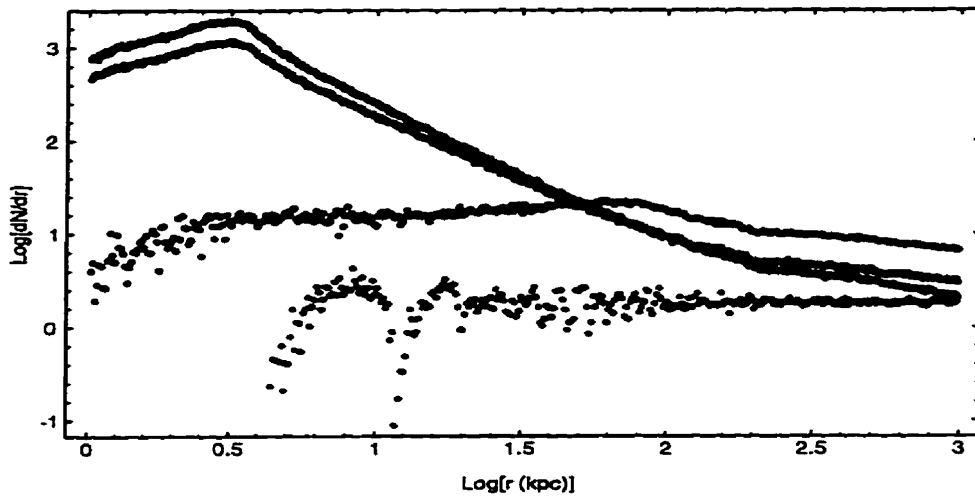


Fig. 6.3: The radial distribution of NSs at the end of the simulation for three different birth velocity distributions with  $f = 0$  (no disk comets). The black points follow the observed pulsar birth velocity distribution found by Lyne & Lorimer (1994). The blue points show the results from a similar birth velocity distribution, but with the average velocity set to 700 km/s rather than 450 km/s. The red points show NSs born with a single velocity of 700 km/s (a  $\delta$  function birth velocity distribution), and the green points correspond to a birth velocity of 2000 km/s. Any distributions which leave bound stars in the deep central potential well of the Galaxy give a significant concentration of objects at small radii.

Here,  $A$  is a constant relating to the cross-section for collisions,  $n_{\text{ns}}$  is the NS number density, normalised to unity at the maximum value,  $n_c$  is the normalised total comet number density (disk comets plus GC comets), and  $v_{\text{rel}}$  is the average relative speed of the two populations at the point in question, determined in the simulations. This includes only gravitational focussing in the collisions.

The burst frequency in this model can be roughly estimated, but since much of the physics is unknown, assigning values to the constants should be taken as tentative at best. Very approximately,  $\frac{dN_{\text{bursts}}}{dt} = N_c \bar{n}_{\text{NS}} \sigma_{\text{int}} v_{\text{rel}}$ , where  $N_c$  is the total number of comets,  $\bar{n}_{\text{NS}}$  is an average number density of NSs, and  $\sigma_{\text{int}}$  is the interaction cross-section.

The total number of comets is given by  $N_c = N_{\text{sGC}} N_{\text{cGC}} + N_{\text{sd}} N_{\text{cd}}$ , where  $N_{\text{sGC}}$  is the total number of GC stars ( $\simeq 10^7$ ),  $N_{\text{sd}}$  is the total number of disk stars ( $\simeq 10^{10}$ ),  $N_{\text{cd}}$  is the number of comets produced by a disk star, and  $N_{\text{cGC}}$  is the number of comets produced by a GC star; using the efficiency ratio  $f$  from section 6.3,  $N_{\text{cGC}} = N_{\text{cd}}/f$ .

As a rough estimate, we can use the number of comets estimated to have been ejected from our solar system as an approximation to  $N_{\text{cd}}$ . Assuming a total population of  $10^9$  NSs, most inside a sphere of radius 40 kpc, relative speeds on the order of  $10^3$  km/s, and that the cross-section is just the square of the light-cylinder radius for a NS spinning with an angular velocity of 0.1 rad/s, the number of bursts per day is roughly  $\frac{dN}{dt} \simeq 4\text{bursts/day}(\frac{10^{-6}}{f})$ .

### 6.5 Simulated Gamma-Ray Burst Distribution

The burster distribution was investigated for several different choices of neutron star birth velocity distribution and efficiency ratio  $f$ . Table 6.1 lists the different models and the results of the statistical tests discussed in chapter 2. The LL distribution is that taken from Lyne & Lorimer (1994) (equation 6.2), and the 700 avg distribution is this same distribution with the average velocity increased from 450 km/s to 700 km/s. Since the minimum flux observable flux in our model is a free parameter (related to the total GRB luminosity, which is a free parameter), the value of  $F_{\text{min}}$  that makes  $V/V_{\text{max}} = 0.33 \pm 0.01$  is given (to match the BATSE

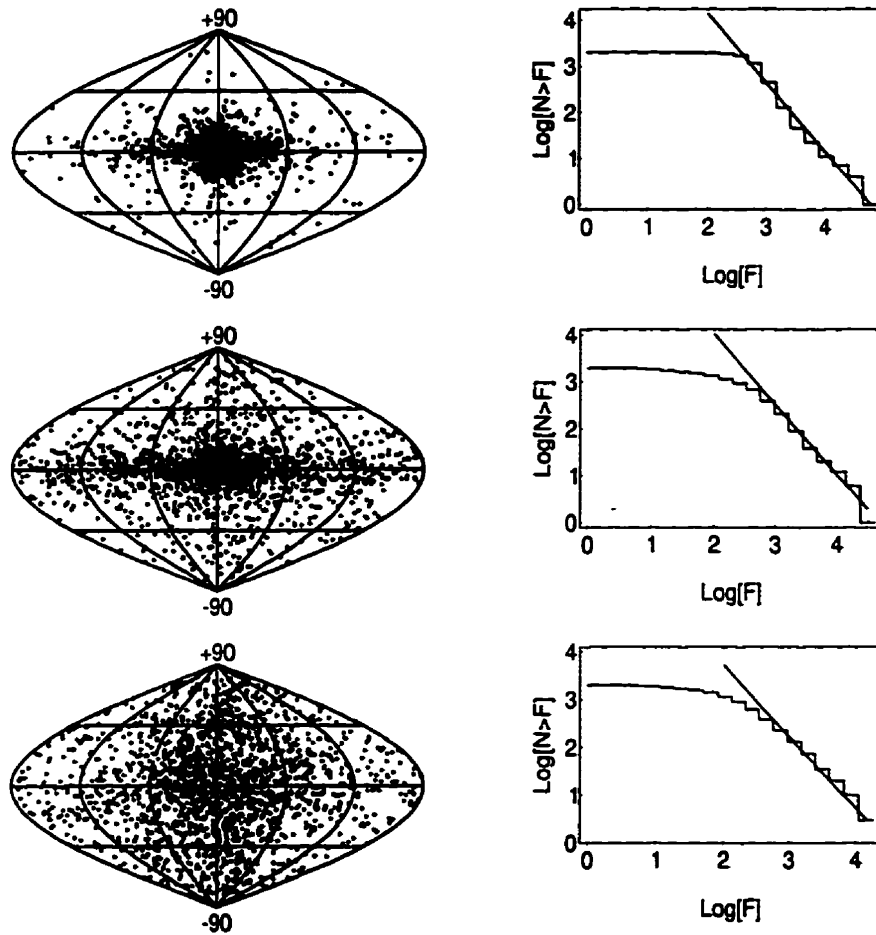


Fig. 6.4: The distributions on the sky and in flux of 2000 GRBs for three different NS birth velocity distributions. The top plots show the results for a birth distribution following the observed pulsar distribution, the middle plots correspond to a birth velocity fixed at 700 km/s, and the bottom plots are the results of a birth velocity of 2000 km/s.

Distribution	$\langle \sin^2 b - 1/3 \rangle$	$\langle \cos \theta \rangle$	$\mathcal{W}$	$\mathcal{B}$	$F_{\min}$	$r_{\max}$
LL	-0.300	0.860	4435	5611	$252 \pm 7$	$12.6 \pm 0.2$
700 avg	-0.290	0.841	4250	5206	$248 \pm 7$	$12.7 \pm 0.2$
700 km/s	-0.205	0.450	1219	1357	$200 \pm 9$	$14.1 \pm 0.3$
2000 km/s	-0.051	0.373	836	167	$105 \pm 5$	$19.5 \pm 5$

Tab. 6.1: The tests of isotropy and homogeneity for the simulated GRB distributions. The expected values for an isotropic distribution are:  $\langle \sin^2 b - 1/3 \rangle = 0 \pm 0.007$ ,  $\langle \cos \theta \rangle = 0 \pm 0.013$ ,  $\mathcal{W} = 3.00 \pm 2.45$ , and  $\mathcal{B} = 5.00 \pm 3.16$ .  $F_{\min}$  is the required minimum flux such that  $\langle V/V_{\max} = 0.33 \pm 0.01$  to match the BATSE distribution, and  $r_{\max}$  is the distance (in kpc) corresponding to this minimum flux (the maximum observable distance).

value).  $r_{\max}$ , the corresponding radius in kpc out to which the hypothetical instrument can probe, is also given.

Figure 6.4 shows sky maps and distributions in flux of 2000 sample GRB positions for three different birth velocity distributions of the NSs. The first has a birth velocity distribution following the observed pulsar birth velocity distribution, the second shows stars born with a single velocity of 700 km/s, and the third has stars born with a velocity of 2000 km/s. The efficiency ratio  $f = 0$  (no disk comets) for all these simulations. The anisotropy toward the Galactic centre is obvious for all the cases, even without including the effect of the disk comet population, though is most striking for the birth velocity distribution which follows the observed pulsar birth velocity distribution, as the low-velocity tail of the distribution binds a large number of stars well inside the Galaxy's potential well. Including a disk population rapidly (for any  $f > 10^{-5}$ ) makes clumping toward the Galactic plane extremely efficient. Note that increasing  $f$  beyond  $10^{-5}$  not only causes clumping toward the disk, but also decreases the number of bursts/day to numbers much smaller than are observed. The requirement of such a discrepancy in the ejection efficiencies is another strike against this model.

The flux of a burst was calculated by letting the total luminosity  $L$  of a burst follow a gaussian distribution in logarithmic space with an average value of  $5 \times 10^5$  (unitless); the value chosen is arbitrary, as it simply sets the scale for flux. A standard deviation of half an order of magnitude was used. This is a somewhat ad-hoc value; the true distribution

in  $E$  likely depends on distributions of NS magnetic field strength and spin rate, which are unknown for the burster population. The results are not very sensitive to this spread as long as it is less than two orders of magnitude, where it becomes comparable to the spread in flux due to the range in distances of the bursts.

Table 6.1 gives the maximum radius  $r_{\max}$  to which the hypothetical instrument can probe if the value of  $V/V_{\max}$  for the simulation distributions is set to the BATSE value. However, since the plots in figure 6.4 show all the bursts, regardless of their flux, the actual observed distribution of bursts will be somewhat different. Figure 6.5 shows the distribution for the simulation with a NS birth velocity of 2000 km/s where only the bursts with  $r < r_{\max}$  are shown. The bursts are clumped even more strongly toward the Galactic centre in this flux-limited case.

The relation  $\log(N > F) \propto -3/2 \log F$  holds for an isotropic distribution of standard candles, where  $\log(N > F)$  is the number of bursts with flux greater than  $F$ . This relationship holds for all the simulation data (shown in the right-hand column of figure 6.4) at large values of flux (probing the close GRBs), though the fit is quite rough for the data where the NSs are born with the observed pulsar birth velocity distribution. The 700 km/s and 2000 km/s NS birth velocity simulations show qualitatively the same behaviour as the BATSE distribution.

## 6.6 Conclusions

These results suggest that models of GRBs as comet-NS collisions in an extended Halo are untenable for a wide range of free parameters. While simulation data, with a somewhat unphysical choice for the ejection efficiency of GC stars, roughly meet the distribution in flux of real GRBs, no values of the free parameters allow a fit to the isotropy data. However, this work does assume that the NSs are ejected from the Galactic disk, and are not relics from the initial formation of the Galaxy. Choosing an appropriate distribution of relic NSs may allow a model in agreement with the observations.

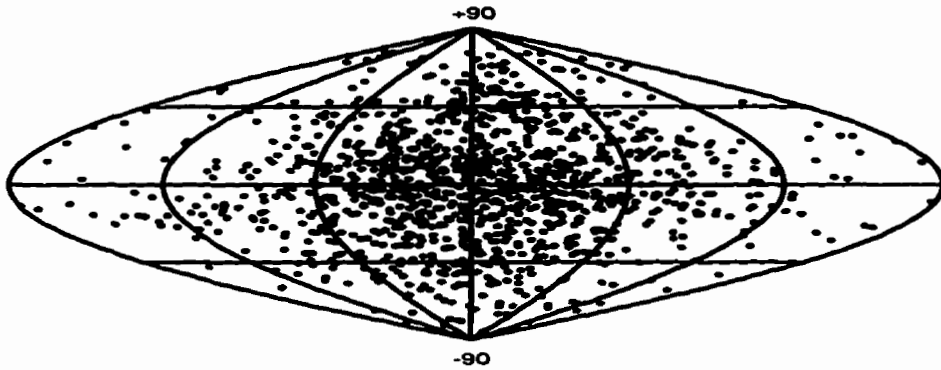


Fig. 6.5: Sky distribution of 1194 GRBs inside  $r_{\max} = 19.5$  kpc for the simulation with a NS birth velocity of 2000 km/s. This is the distribution which would be observed by setting the minimum observable flux which makes  $V/V_{\max}$  for the distribution equal to the BATSE value of 0.33. The clumping toward the Galactic centre is more obvious than in the sample which is not minimum-flux-limited.



The most powerful constraint on the model, even ignoring the clustering of bursts toward the Galactic centre, is that GC stars must be  $> 10^6$  times as efficient at producing comets as disk stars; if not, the burst rate would be many orders of magnitude too low and the bursts would be clustered very strongly toward the Galactic disk. There is no reason to believe that the older stars in GCs would produce so many comets, though there does not seem to be any convincing theoretical arguments to suggest that they would not.

There are a number of ways to change the simulation to allow a more isotropic distribution, though adding these factors simply adds free parameters. Allowing a minimum time before a NS can become a burster, a maximum time after which it can no longer burst, or beaming the radiation along the NS velocity (REFs?) can help remove the clumping toward the Galactic centre. However, since the comet distribution is peaked toward the Galactic centre and along extends to a radius of approximately 100 kpc, these parameters would have to be very fine-tuned to meet the constraints derived by the BATSE observations. In addition, replacing the spherical dark matter halo with an oblate one might reduce the clumping toward the Galactic centre.

## 7. THE DEUTSCH FIELDS

The electromagnetic fields around a highly conducting and magnetic sphere in vacuum were derived by Deutsch (1955). When the charge densities outside the star are everywhere much less than the Goldreich-Julian charge density (equation 1.6), these fields are a good description of those around a pulsar. The arguments for an evacuated magnetosphere are presented in chapter 9; this chapter deals with an in-depth analysis of the Deutsch field structure, independent of the physics which allows such a high-energy structure to exist. The full expressions for the electric and magnetic fields are given in Appendix 1.

### 7.1 *Definition of Vacuum*

Goldreich & Julian (1969) examined the case of a filled, corotating magnetosphere and calculated the charge density at every point in space.

If we assume a dipole magnetic field (a good approximation well inside the light cylinder, since the currents are small), we know that

$$\vec{\nabla} \cdot \vec{B} = 0 \qquad \vec{\nabla} \times \vec{B} = 0 \qquad (7.1)$$

Also, for corotation with the star, the electric field must enforce a drift of  $\vec{\beta}_\phi = \vec{\Omega} \times \vec{r}$ . Therefore,

$$\vec{E} = \vec{\beta}_\phi \times \vec{B} \qquad (7.2)$$

The charge density can be found from

$$4\pi\rho = \vec{\nabla} \cdot \vec{E}$$

$$\begin{aligned}
&= \vec{\nabla} \cdot (\vec{\beta}_\phi \times \vec{B}) \\
&= \vec{B} \cdot (\vec{\nabla} \times \vec{\beta}_\phi) - \vec{\beta}_\phi \cdot (\vec{\nabla} \times \vec{B})
\end{aligned}$$

However, since  $\vec{\nabla} \times \vec{B} = 0$  for the dipole field, and using  $\vec{\nabla} \times \vec{\beta}_\phi = 2\vec{\Omega}/c$ ,

$$\rho = \frac{\vec{\Omega} \cdot \vec{B}}{2\pi c} \quad (7.3)$$

which is the Goldreich-Julian result (equation 1.6).

Since this charge density forces corotation, it can be taken to be a representative charge density that will significantly alter the electric fields. If the charge density is much less than the Goldreich-Julian value, the induced electric field will be much less than the vacuum electric field.

The magnetic fields will also be unaffected by a charge density much less than the Goldreich-Julian value; in fact, even a corotating magnetosphere will only affect the vacuum fields near the light cylinder. This can be shown by examining Maxwell's equations for the induced magnetic field due to currents of order  $J \simeq en_{\text{GJ}}c$ :

$$\vec{\nabla} \times \vec{B}_{\text{ind}} \simeq \frac{B_{\text{ind}}}{r} \simeq \frac{4\pi}{c} J \simeq 4\pi n_{\text{GJ}} e \quad (7.4)$$

where  $B_{\text{ind}}$  is the magnetic field induced by the currents. Also,

$$\vec{\nabla} \cdot \vec{E}_{\text{cr}} \simeq \frac{E_{\text{cr}}}{r} = 4\pi n_{\text{GJ}} e \quad (7.5)$$

where  $\vec{E}_{\text{cr}} = -\vec{\beta}_\phi \times \vec{B}$  is the corotation electric field. Substituting for  $n_{\text{GJ}}$  in terms of the electric field, the induced magnetic field is estimated as

$$B_{\text{ind}} \simeq E_{\text{cr}} \quad (7.6)$$

Therefore, since the electric field inside the light cylinder is much smaller than the magnetic field (of order  $B(r/R_{\text{lc}})$ ), the induced magnetic field is negligible compared to the vacuum magnetic field everywhere well inside the light cylinder when the charge density is equal

to the Goldreich-Julian value. Charge densities much less than those required to enforce corotation will not alter the magnetic field even near the light cylinder.

## 7.2 The Point Dipole Fields

The Deutsch fields are given in full in Appendix 1. These fields tend to the fields of a spinning point dipole in vacuum when far from the star, as would be expected (the boundary conditions at the star alter the fields only locally). Some discussion of the point dipole fields is therefore worthwhile.

### 7.2.1 Inside the Light Cylinder

When  $r \ll R_{lc}$ , the point dipole magnetic fields look like a rotating, undistorted dipole inclined at angle  $\chi$  to the rotation axis, and the electric fields are circles in planes parallel to the plane defined by  $\vec{\Omega}$  and  $\vec{\mu}$ .

A coordinate change to a frame where the  $z$ -axis is parallel to  $\vec{\mu}$  rather than  $\vec{\Omega}$  simplifies the analysis of the fields in this limit enormously. In this frame, the magnetic field is a static dipole. The physics is made somewhat more clear by using a Cartesian coordinate system, where  $\hat{z}$  is parallel to  $\mu$  and  $\hat{y}$  is parallel to  $\vec{\Omega} \times \vec{\mu}$ . In these coordinates,

$$E_x = -\frac{\mu z}{r^3 R_{lc}} \sin \chi \quad E_y = 0 \quad E_z = \frac{\mu x}{r^3 R_{lc}} \sin \chi \quad (7.7)$$

and

$$B_x = \frac{3\mu x z}{r^5} \quad B_y = \frac{3\mu y z}{r^5} \quad B_z = \frac{\mu}{r^5} (3z^2 - r^2) \quad (7.8)$$

In this coordinate system, it is immediately obvious that the electric field lines form circles in planes parallel to the  $x$ - $z$  plane. Also, since

$$\vec{E} \cdot \vec{B} = -\frac{x\mu^2 \sin \chi}{r^6 R_{lc}} \quad (7.9)$$

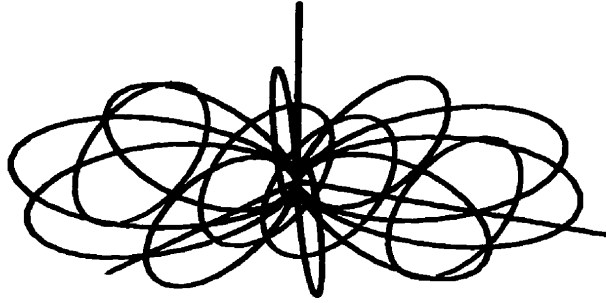


Fig. 7.1: The magnetic and electric field lines for the rotating dipole fields in the limit  $\tau \ll R_{lc}$ . The coordinates have the  $z$ -axis parallel to the effective magnetic dipole moment  $\mu$ ; the rotation axis lies in the  $x$ - $z$  plane - the orientation only affects the magnitude of the electric field, not its direction. The magnetic field (shown in black) is a static dipole field in these coordinates, and the electric field lines (in red) are circles around the  $y$ -axis.  $\vec{E}$  and  $\vec{B}$  are perpendicular everywhere in the  $y$ - $z$  plane, forming a simple example of a null surface that is important to the Deutsch field gamma-ray pulsar model.

it can be readily seen that the component of electric field parallel to the magnetic field goes to zero in the  $x = 0$  plane. This is a simple (yet important) example of a **null surface**, where  $\vec{E} \cdot \vec{B} = 0$ ; these will be discussed in more detail in section 7.4.

Figure 7.1 shows a plot of the magnetic and electric field lines for the pulsar. In this plot, the rotation axis lies in the  $x$ - $z$  plane. Figure 7.2 shows the drift velocity of charges in the  $x = 0$  plane, where  $\vec{E} \cdot \vec{B} = 0$ . The charge velocities on the null surface have two components: one parallel or anti-parallel to the field line, and another equal to the drift velocity. This is a special case of charge motion in arbitrary strong electric and magnetic fields, which is discussed in more detail in chapter 8.

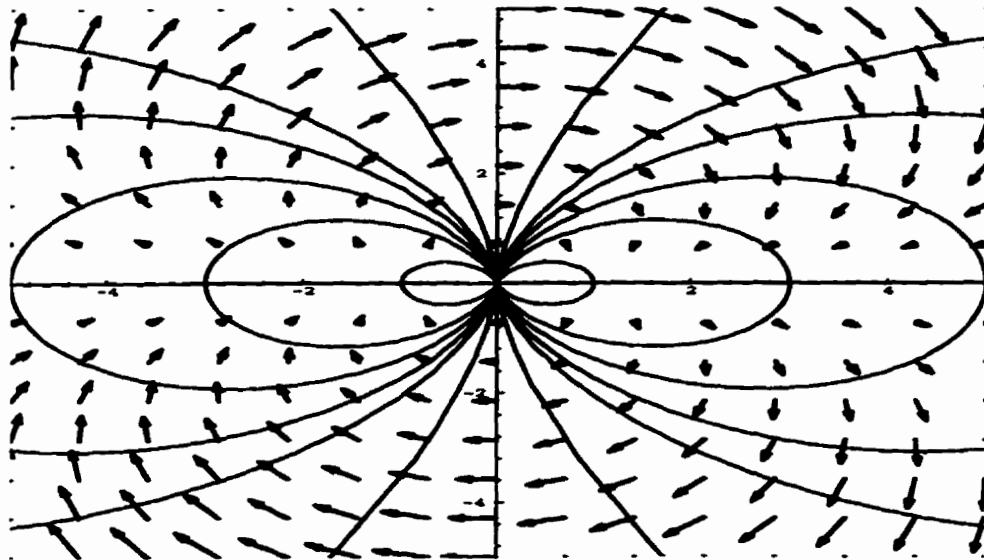


Fig. 7.2: The charge drift velocity (black arrows) on the null surface  $x = 0$  superimposed on the dipole field lines (in red). Charges which hit the null surface are bound to it; their velocities have a component equal to the drift velocity and another parallel to the magnetic field line.

### 7.2.2 Outside the Light Cylinder

When  $r \gg R_{lc}$ , the electric and magnetic fields are given by:

$$E_r = 0 \quad E_\theta = -\frac{\mu}{rR_{lc}^2} \sin \chi \sin \lambda \quad E_\phi = -\frac{\mu}{rR_{lc}^2} \sin \chi \cos \theta \sin \lambda$$

$$B_r = 0 \quad B_\theta = \frac{\mu}{rR_{lc}^2} \sin \chi \cos \theta \sin \lambda \quad B_\phi = -\frac{\mu}{rR_{lc}^2} \sin \chi \sin \lambda$$

where  $\lambda = \phi - \Omega t + r/R_{lc}$ .

Here we have returned to the usual spherical coordinate system with a z-axis parallel to  $\vec{\Omega}$  rather than  $\vec{\mu}$  (in contrast to the last section).

Since  $|E| = |B|$  and  $\vec{E} \cdot \vec{B} = 0$ , these fields describe an electromagnetic wave, propogating spherically away from the star with a frequency equal to the frequency of the star's rotation. The total power carried away by this wave can be found by integrating the Poyting vector over the surface of a sphere of radius  $r$ :

$$\begin{aligned} P &= \int \vec{S} \cdot \hat{n} dA \\ &= \frac{c}{4\pi} \int_{\phi=0}^{2\pi} \int_{\theta=0}^{\pi} [(\vec{E} \times \vec{B}) \cdot \hat{r}] r^2 \sin \theta d\theta d\phi \end{aligned}$$

This reduces to

$$P = \frac{2\Omega^4 \mu^2 \sin^2 \chi}{3c^3} \quad (7.10)$$

This radiation, called **magneto-dipole radiation** (originally derived by Ostriker & Gunn 1969), is the cause of the pulsar's spindown: the magneto-dipole radiation is lost at the expense of the star's rotational kinetic energy. This fact is the primary means of calculating the effective magnetic dipole moment, and hence the magnetic field at the stellar surface.

Since the rotational kinetic energy is equal to  $\frac{1}{2}I\Omega^2$ , where  $I$  is the stellar moment of inertia,

$$I\Omega\dot{\Omega} = -P$$

and substituting for  $P$  from above,

$$\dot{\Omega} = -\frac{2\mu^2 \sin^2 \chi}{3c^3 I} \Omega^3 \quad (7.11)$$

Writing  $\Omega$  and  $\dot{\Omega}$  in terms of the period  $P$  and the period derivative  $\dot{P}$  and substituting representative values, the effective magnetic dipole moment is:

$$\mu \simeq 2 \times 10^{30} \text{G} - \text{cm}^3 \left( \frac{P\dot{P}}{5 \times 10^{-15} \text{s}} \right)^{1/2} \left( \frac{I}{10^{45} \text{g} - \text{cm}^3} \right)^{1/2} \csc \chi \quad (7.12)$$

Roughly, with  $B_{\text{surf}} \simeq \mu/R^3$ , where  $R \simeq 10^6$  cm is the stellar radius,

$$B_{\text{surf}} \simeq 2 \times 10^{12} \text{G} \left( \frac{P\dot{P}}{5 \times 10^{-15} \text{s}} \right)^{1/2} \left( \frac{I}{10^{45} \text{g} - \text{cm}^3} \right)^{1/2} \csc \chi \quad (7.13)$$

### 7.2.3 Near the Light Cylinder

The most complicated behaviour occurs when  $r \simeq R_{\text{lc}}$ . The dipole field structure of the inner magnetosphere begins to twist as the light travel time becomes of the same order as the rotation period, and the electric field structure is similarly complicated; there is no simple interpretation of the field structure, unlike with the limiting cases. Figure 7.3 shows some of the magnetic field lines which close outside the light cylinder in the case of orthogonal fields (where the rotation axis and effective magnetic dipole moment are perpendicular). The dipole-like field lines begin to wrap up, approaching the radiation fields as  $r$  increases.

## 7.3 The Effect of the Star

The boundary conditions at the surface of the star have no effect on the magnetic field, but do dramatically alter the electric field near the star - extra components which fall off



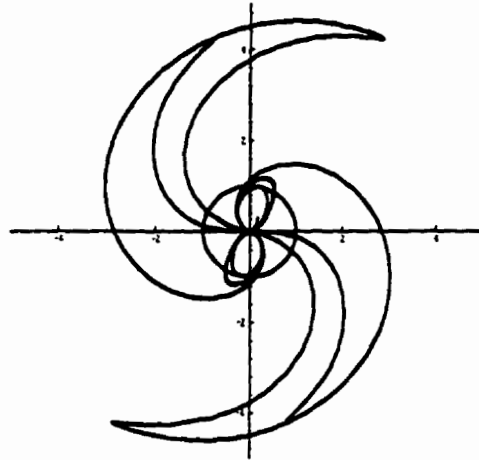


Fig. 7.3: Selected field lines for the orthogonal point dipole fields in the plane perpendicular to the rotation axis. The circle shows the light cylinder, and the dimensions are in units of the light cylinder radius  $R_{lc}$ .

like  $r^{-4}$  (as compared to the  $r^{-2}$  behaviour of the fields far from the star) are added which do not have a simple structure. These “boundary fields” can significantly alter the null surface structure within a stellar radii of the surface, which is one of the critical factors in determining global current structure.

The electric fields in spherical polar coordinates near the star are approximately given by

$$E_r = -\frac{\mu a^2}{2r^2 R_{lc}} \left[ \frac{(1 + 3 \cos 2\theta) \cos \chi}{r^2} + \frac{3 \cos \phi \sin 2\theta \sin \chi}{r^2} \right] \quad (7.14)$$

$$E_\theta = -\frac{\mu}{r^2 R_{lc}} \left[ \frac{a^2 \sin 2\theta \cos \chi}{r^2} + \left(1 - \frac{a^2}{r^2}\right) \cos \phi \sin \chi \right] \quad (7.15)$$

$$E_\phi = \frac{\mu}{r^2 R_{lc}} \left(1 - \frac{a^2}{r^2}\right) \cos \theta \sin \phi \sin \chi \quad (7.16)$$

which shows that the radial component of the electric field disappears for  $r \gg a$ . The effect of the boundary conditions at the star drops off very quickly with radius, and is dominated by the point dipole fields for approximately  $r > 3a$ .

## 7.4 Null Surfaces

A “null surface” is defined to be a surface in the magnetosphere where the electric and magnetic fields are perpendicular. Charges are often attracted to these surfaces (see section 8.4 for a discussion of charge motion on and near the null surfaces), where they can move around the magnetosphere with low energy. As such, they are critical to the determination of the current structure, which must be known in a global model of the pulsar magnetosphere. In addition, since charges on null surfaces move with relatively small Lorentz factors, they do not contribute to the high-energy radiation observed by young pulsars.

The dynamics of charges in the magnetosphere, and in particular on null surfaces, is discussed in chapter 8; I will only present the basic characteristics of these surfaces in this section.

Two basic types of null surfaces exist: one which contains the magnetic field lines, and one which does not. Which structure dominates in different regions of the magnetosphere is important to demonstrate.

#### 7.4.1 *Wired Null Surfaces*

A null surface which contains the magnetic field lines is called a “wired” null surface (as the magnetic field lines wire the surface). This sort of null surface dominates the intermediate magnetosphere, far from the star but far inside the light cylinder (for  $a \ll r \ll R_{lc}$ ). This is easily observed by examining equations 7.8 and 7.9;  $\vec{E} \cdot \vec{B} = 0$  in the plane  $x = 0$ , and  $B_x = 0$  in this plane as well.

As discussed in chapter 8, these surfaces are important to vacuum models because they attract charges of both signs equally. Therefore the surfaces remain uncharged, and do not affect the electric field structure.

#### 7.4.2 *Pierced Null Surfaces*

A “pierced” null surface is one which does *not* contain the magnetic field lines (instead they pierce the surface). This sort of null surface attracts only one kind of charge, because the electric field parallel to the magnetic field line switches direction on either side of the surface. In the case of pierced null surfaces, this is how charges are bound, which is quite different than the case of wired surfaces. These surfaces are dangerous in a magnetosphere attempting to remain evacuated, since the surfaces build up charge in a relatively small volume. If the charges densities are large enough, this will destroy the null surface by altering the electric field structure.

This sort of null surface is seen near the star and in the outer magnetosphere near the light cylinder. The binding of charges to these surfaces is less persistent than with the wired surfaces, because a change in the orientation of the electric field will eject the particle from the surface rather than trap it.

### 7.4.3 Null Surface Structure in the Deutsch Fields

As previously mentioned, the null surface in the limit  $a \ll r \ll R_{lc}$  is a wired null surface. However, the null surface structure changes as  $r$  approaches  $a$  or  $R_{lc}$  and becomes pierced as the field structure becomes more complex.

For example, in the orthogonal Deutsch fields (where  $\vec{\mu}$  is perpendicular to  $\vec{\Omega}$ , the requirement of  $\vec{E} \cdot \vec{B} = 0$  reduces to

$$\left(\frac{r}{a}\right)^2 \cos \theta (\cos \phi + \sin^2 \phi) - \cos \theta (\cos \phi + \sin^2 \phi) - 3 \cos^2 \phi \sin \theta \sin 2\theta = 0 \quad (7.17)$$

In the limit of  $r \gg a$ , the only null surface is at  $\theta = \pi/2$ , which is the wired point dipole null surface for these orthogonal fields. On the star,  $\vec{E} \cdot \vec{B} = 0$  occurs when  $\theta = 0, \pi/2, \pi$  and when  $\phi = \pi/2, 3\pi/2$ .

For  $r \simeq a$ , however, the null surface is rather different than the point dipole fields. Figure 7.4 shows the surface defined by equation 7.17 for  $t = 0$ . Charges of different sign are attracted to or repelled by the surface in different areas (see section 8.4.3); a charge attracted to the surface will flow along it until it hits an area of the surface where it is repelled and leaves the surface. The regions on the null surface that attract positrons are shown in red, and those that attract electrons are shown in blue. Therefore, charges are not attached to this null surface for significant times. The units on the coordinate axes are distances in terms of the stellar radius - the star is a sphere of radius 1.

### 7.5 Symmetries in the Deutsch Fields

To simplify the numerical calculations, we took advantage of three symmetries of the problem. First, there is a symmetry (Symmetry 1) in the fields  $\vec{E} \rightarrow -\vec{E}$  and  $\vec{B} \rightarrow -\vec{B}$  under a translation  $\phi \rightarrow \phi + \pi$ ,  $\theta \rightarrow \pi - \theta$ , where  $\theta$  is the poloidal angle and  $\phi$  is the toroidal angle relative to the rotation axis. Therefore, if a charge  $q$  started at  $\vec{r}_0$  follows the path  $\vec{r}(t)$ , the same charge started at  $-\vec{r}_0$  will take the path  $-\vec{r}(t)$ . The symmetry applies for any

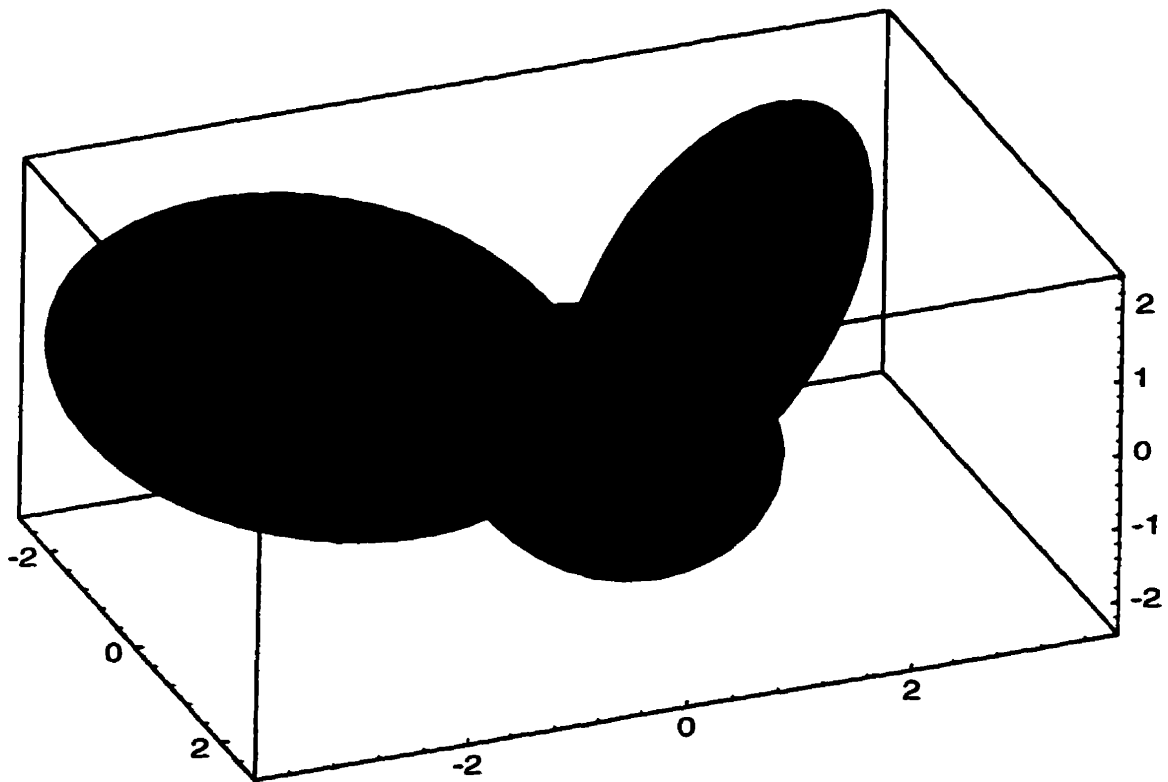


Fig. 7.4: The null surface near the star for the orthogonal Deutsch fields. The null surface is pierced - that is, it does not contain the magnetic field lines everywhere, and therefore different regions attract particular signs of charge. The red regions attract positrons (and repel electrons) and the blue regions attract electrons (and repel positrons). As a charge of one sign flows along the null surface, eventually it will hit a region which repels it, and will leave the surface. Therefore, charges will not be attached to this surface for any significant time. The units along the axes are distances in terms of the stellar radius.

orientation of the dipole moment to the rotation axis.

The second symmetry (Symmetry 2) is between charges of different sign, but only applies when the dipole axis is perpendicular to the rotation axis. The path of a charge  $-q$  started at  $(r_0, \theta, \phi)$  is equal to the path of a charge  $q$  started at  $(r_0, \theta, \phi + \pi)$  rotated through 180 degrees toroidally.

The third symmetry (Symmetry 3) is a result of another property of the fields, that  $\vec{E}(r, \theta, \phi, t)$  equals  $\vec{E}(r, \theta, \phi - \Omega t, 0)$  rotated through an angle  $\Omega t$  in  $\phi$ . This means that a charge  $q$  started at  $(r_0, \theta, \phi, t_0)$  will follow the path of a charge  $q$  started at  $(r_0, \theta, \phi - \Omega t_0, 0)$  rotated through  $\Omega t_0$  toroidally. This symmetry holds for any orientation of the dipole moment.

Symmetry 1 means that the path of a charge started in the bottom half ( $\theta \in (\pi/2, \pi]$ ) of the magnetosphere at position  $\vec{r}$  can be inferred from the path of a charge in the top half of the magnetosphere started at position  $-\vec{r}$ . A consequence of Symmetry 3 is that charges started at a time  $t_0$  not equal to zero can be found from the paths started at  $t_0 = 0$  by a rotation azimuthally. Symmetry 2 means that positron paths can be inferred from electron paths, but only in the orthogonal Deutsch fields.

The combination of Symmetry 2 and Symmetry 3 has an important consequence for the inferred light curves when the dipole moment is perpendicular to the rotation axis: positrons will radiate in exactly the same manner as electrons, but a half period later. If the electron contribution is a single peak, the positrons will contribute a second peak, exactly 0.5 later in phase, if the distribution of positrons is equal to that of electrons in the magnetosphere. This does not hold for non-orthogonal systems, as Symmetry 2 is broken.

## 8. THE DYNAMICS OF CHARGES IN THE DEUTSCH FIELDS

The model we use for the pulsar magnetosphere is the Deutsch fields. Understanding particle motion in these fields is then critical to the development of a somewhat self-consistent picture of the magnetosphere and the radiation emitted by the pulsar.

To be consistent with the vacuum assumption, particle motion must allow for any charges created to flow out of the magnetosphere - there can be no sinks for charge, or eventually the accumulated charge will cause the vacuum assumption to fail. This is a subtle problem which requires a detailed examination of the different types of possible charge motion in these relatively complex fields.

### *8.1 The Radiation Reaction Force*

Our simulation of charge motion only considers three forces: the electric force, the magnetic force, and the radiation reaction force. The first two are well-understood; however, it is worthwhile to discuss the radiation reaction force in some detail due to the uncertainty in its form.

Most problems in classical electrodynamics can be attacked with a somewhat incomplete theory where the fields determine particle motion, and the radiation can be calculated as a small, if not negligible, perturbation. This is not the case in pulsar physics; the details of how the radiation reacts back on the particle are important.

As per Jackson (1975), the power emitted from a non-relativistic particle is given by Larmor's formula

$$P_{\text{non-rel}} = \frac{2}{3} \frac{e^2}{c} |\ddot{\vec{v}}|^2 \quad (8.1)$$

This can be written as

$$P_{\text{non-rel}} = \frac{2}{3} \frac{e^2}{m^2 c^3} \left( \frac{d\vec{p}}{dt} \cdot \frac{d\vec{p}}{dt} \right) \quad (8.2)$$

where  $\vec{p}$  is the charge's momentum. The relativistic generalisation is then

$$P_{\text{rel}} = -\frac{2}{3} \frac{e^2}{m^2 c^3} \left( \frac{dp_\mu}{d\tau} \frac{dp^\mu}{d\tau} \right) \quad (8.3)$$

where  $p^\mu$  is the charge's four-momentum and  $\tau$  is the charge's proper time ( $d\tau = dt/\gamma$ ).

Since

$$-\frac{dp_\mu}{d\tau} \frac{dp^\mu}{d\tau} = \left( \frac{d\vec{p}}{d\tau} \right)^2 - \beta^2 \left( \frac{dp}{d\tau} \right)^2 \quad (8.4)$$

the power output can be written

$$P_{\text{rel}} = \frac{2}{3} \frac{e^2 \gamma^2}{m^2 c^3} \left[ \left( \frac{d\vec{p}}{dt} \right)^2 - \beta^2 \left( \frac{dp}{dt} \right)^2 \right] \quad (8.5)$$

In the perturbative limit, where the energy loss over a typical mechanical timescale is much smaller than the charge's energy, the second term in the square bracket is much smaller than the first if the motion is not linear. If the motion is instantaneously circular with a radius of curvature  $\rho$ , then  $|\frac{d\vec{p}}{dt}| = \omega |\vec{p}|$ , where  $\omega = c\beta/\rho$ . Then, the radiative power output can be written

$$P_{\text{rad}} = \frac{2}{3} \frac{e^2 c}{\rho^2} \beta^4 \gamma^4 \quad (8.6)$$

The radiation is beamed along the particle's velocity vector with a pattern width of approximately  $\theta = 1/\gamma$ ; for  $\gamma \gg 1$ , assuming all the power to be beamed along the velocity is a very good assumption. Therefore, in this limit the radiation reaction force can be expressed as

$$\vec{F}_{\text{rad}} = -\frac{P_{\text{rad}}}{c} \hat{v} \quad (8.7)$$



where  $\hat{v}$  is a unit vector in the direction of the velocity.

It is not generally true that the radiative power losses in charges in pulsar magnetospheres are perturbatively small. In the limit where the radiation back-reaction is important, the problem becomes much less well-defined from the classical point of view.

The problem has been investigated by Lieu & Axford (1993) (and extended in Lieu & Axford 1995) where they show that synchrotron emission is equivalent to inverse Compton scattering of the charge off a field of photons which approximate the electromagnetic fields observed by the charge (an “equivalent” photon field). They give analytic expressions for spinless particles in the interesting Landau limit of  $\gamma B > B_Q$  and  $\gamma \gg 1$  where quantum electrodynamic effects become important, and show that the effect of spin is negligible (though incorrectly estimated by use of their equivalent photon field technique).

They find that the total power output in the Landau limit (which is important for the case of the pulsar magnetosphere) is strongly suppressed reduced from that expected from the classical emissivity due to Compton redshift associated with recoil and because the Compton cross-section decreases below the Thompson value.

The form of the radiation reaction force used in this work followed the low-energy limit of Jackson, and ignores the problem of self-interaction. There is some justification for this, as the charges are almost always radiation-reaction limited (see section 8.7). Therefore, the charge’s energy does not vary particularly quickly, though for different reasons than in the perturbative limit. The effect of recoil on the charge may still significantly alter the radiation physics.

## 8.2 *Numerical Integration of Charge Motion - the Complete Simulation*

The equations of motion for the charges in the Deutsch fields have no analytic solution in general. Therefore, it was necessary to resort to numerical techniques for solving the problem.

In what will be called the “complete” simulation (to differentiate it from the simulation

which applies an approximation to the particle motion, discussed in the next section), the equations of motion were integrated directly, using a fourth-order Runge-Kutta numerical technique.

The equation of motion is simply

$$\frac{d\vec{p}}{dt} = \vec{F} = q(\vec{E} + \vec{v} \times \vec{B}) + \vec{F}_{\text{rad}} \quad (8.8)$$

where  $\vec{F}_{\text{rad}}$  is the radiation reaction force, taken as equation 8.7.

Several timescales present themselves. The first is the pulsar period,  $T = 2\pi/\Omega$ , on the order of milliseconds to seconds. The second is the period of synchrotron motion around the field line

$$T_{\text{synch}} = \frac{2\pi\gamma mc}{eB} \quad (8.9)$$

where  $\gamma$  is the charge's Lorentz factor and  $B$  is the local magnetic field. For non-relativistic charges in magnetic fields of  $10^9$  G (typical of the inner magnetosphere, at roughly a tenth of the light cylinder radius), this timescale is roughly  $4 \times 10^{-16}$  seconds.

A third timescale is similar to the synchrotron timescale, but related to the electric field rather than magnetic field. Since the electric field is generally much less than the magnetic field (except near and outside the light cylinder, where it is of the same order), this timescale is longer than  $T_{\text{synch}}$ , and does not affect the simulation construction.

A fourth timescale is related to the radiation reaction force; it is roughly the time needed to radiate away the charge's energy perpendicular to the magnetic field lines in synchrotron radiation:

$$T_{\text{rad}} = \frac{m^3 c^5}{\gamma e^4 B^2} \quad (8.10)$$

Setting  $\gamma = 1$  (where the approximation about the nature of the radiation reaction force fails, but illustrative nonetheless) gives an upper limit to this timescale at roughly  $10^{-10}$  seconds (again with  $B = 10^9$  G).

The difficulty in simulating charge motion in these powerful fields is the disparity in the different timescales of the problem. Too wide a gap in timescales generally translates into very long integration times to properly capture the full solution. In fact, the synchrotron timescale is so constraining that charges with energies less than roughly  $10^3$  cannot be simulated in a reasonable amount of computing time.

### 8.3 *The Drift-Frame Bead on a Wire Approximation*

#### 8.3.1 *The Approximation*

The numerical integration of the charged particle motion in the simulations is simplified enormously under the application of a key assumption in this work, labelled the drift frame bead-on-a-wire (DFB) approximation. It is assumed that, in a frame where the electric field is parallel to the magnetic field, the charge has a velocity directed parallel or antiparallel to  $\vec{B}$  with magnitude approximately equal to  $c$ ; the velocity in the pulsar rest frame at any point can then be determined by boosting back to the original frame of reference. This is the case when synchrotron motion is not important, which occurs when the timescale to radiate away momentum perpendicular to the field line is very short.

Consider a point in the magnetosphere with electric field  $\vec{E}$  and magnetic field  $\vec{B}$ . Define the  $z$ -axis to be parallel to  $\vec{B}$ , and  $\vec{E}$  to have components only in the  $z$  and  $y$  directions. There exists a boost of  $v = c\beta\hat{x}$  which defines a frame of reference where  $\vec{E}'$  is parallel to  $\vec{B}'$  as long as the electric field is not perpendicular to the magnetic field (the case of  $\vec{E} \cdot \vec{B} = 0$  is considered separately as motion on a null surface, discussed in section 7.4); this has been recognized by other authors as well (e.g. Robertson & Noonan 1968). This scenario is shown in Figure 8.1; the boost can be shown to be

$$\beta = \frac{B^2 + E^2 - \sqrt{(B^2 + E^2)^2 - 4B^2E_y^2}}{2BE_y} \quad (8.11)$$

where all the quantities relate to the pulsar rest frame. This is valid for  $E > B$  or  $E < B$ , and even  $E = B$  as long as the two are not perpendicular.

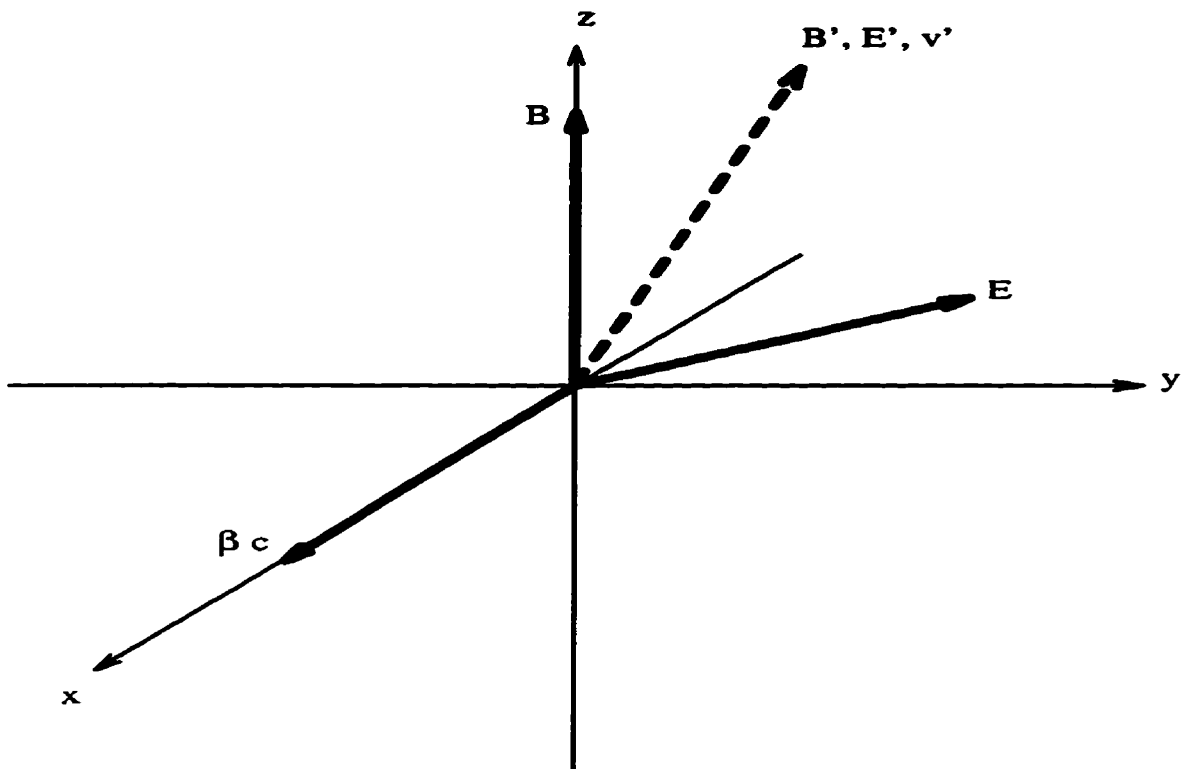


Fig. 8.1: The coordinate system for the DFB approximation analysis. A boost along the  $x$ -axis shown in the figure moves into a frame where the electric field  $\vec{E}'$  is parallel to the magnetic field  $\vec{B}'$ . In the pulsar rest frame, the  $z$ -axis is taken to be parallel to  $\vec{B}$ , and  $\vec{E}$  lies in the  $y$ - $z$  plane. In the boosted frame, the charges are assumed to move either parallel or anti-parallel to  $\vec{B}'$ .

It is assumed that, in this frame, the velocity of the charge is either parallel or anti-parallel to  $\vec{B}'$  (depending on the sign of  $q\vec{E} \cdot \vec{B}$ , where  $q$  is the particle's charge) and that the particle is ultra-relativistic, so its speed is nearly  $c$ . This requires no momentum perpendicular to the field line in this frame, which occurs with small pitch angle motion or when the perpendicular momentum is quickly radiated away through synchrotron radiation. Boosting back to the initial frame, the charge's velocity is then

$$\vec{v} = c\beta\hat{x} \pm \frac{c B'_y}{\gamma B'}\hat{y} \pm \frac{c B'_z}{\gamma B'}\hat{z} \quad (8.12)$$

$$= c\beta\hat{x} \pm \frac{c \beta E_z}{\gamma U}\hat{y} \pm \frac{c B - \beta E_y}{\gamma U}\hat{z} \quad (8.13)$$

where  $U = \sqrt{B^2 + \beta^2 E^2 - 2\beta E_y B}$  and  $\gamma = 1/\sqrt{1 - \beta^2}$ . The expression is exact, given the assumption about the particle motion in the boosted frame of reference.

Given an initial position, the charge's motion is now defined by the solution to a set of three first-order ordinary differential equations  $\vec{v} = d\vec{r}/dt$ , which can be solved numerically with relative ease. The particle's energy can be found by integrating the power input due to the electric field and the power output due to the radiation loss.

It is generally found that, since the fields are so large, the radiation reaction force acts like a thermostat, balancing the energy input from the electric force with the energy output due to radiation (see section 8.7). This gives a convenient description of the particle's energy at any point,

$$\gamma^4 = \frac{3 q \vec{E} \cdot \vec{v} \rho^2}{2 e^2 c} \quad (8.14)$$

where the radiative power output was taken as equation 8.6.

The whole approximation is only valid where the timescale to radiate away the momentum perpendicular to the field direction is much less than the timescale  $1/\Omega$  over which the fields vary significantly; this reduces to another constraint on  $\Omega$  and  $\mu$  when the charges are *not* on a null surface:

$$\Omega^{\frac{21}{4}} \mu^{\frac{9}{4}} \gg 5 \times 10^{71} \quad (8.15)$$

For a typical  $\mu = 10^{30} \text{ G cm}^3$ , this gives  $\Omega \gg 6 \text{ rad/s}$ , which is true for all the observed gamma-ray pulsars.

If this condition is not met, then in some cases the DFB approximation will still apply. If the radius of the synchrotron orbits is much smaller than the other length scales in the magnetosphere (most critically the light cylinder radius), and the pitch angle of the motion relative to the magnetic field line is small (to maintain a parallel velocity roughly equal to  $c$ ), then the approximation is still valid. This applies for charge motion on the null surface in some cases, where the low Lorentz factors translate into tight orbits around the field lines. However, it does not apply for highly relativistic charges (unattached to a null surface) in a pulsar which does not satisfy condition 8.15.

### 8.3.2 *Comparison with the Complete Simulation*

To test the validity of the DFB approximation, the simulation results were compared with those from the more complex complete simulation which made no approximations about the charge motion. The complete simulation was orders of magnitude slower than the DFB simulation, since the time steps had to be much smaller to properly capture the synchrotron motion around the field lines.

The energy of the particles under the DFB approximation was calculated by integrating the net energy input, which includes two contributions: energy input due to the electric field parallel to the velocity, and energy output due to radiative losses.

To investigate the accuracy of the DFB approximation, charges were started in a Deutsch field magnetosphere at different locations, and their progress charted in the DFB simulation and the complete simulation until they hit a null surface or escaped from the magnetosphere.

In general, one would expect that the DFB approximation would begin to fail outside the light cylinder, where the smaller magnetic fields would translate into longer timescales to

radiate the momentum perpendicular to the magnetic field line (see equation 8.10). However, it should work well in the inner magnetosphere where the fields are much stronger than at the light cylinder.

The first two simulations were run using a model pulsar with  $\Omega = 100$  rad/s and  $\mu = 10^{30}$  G cm<sup>3</sup>. This pulsar readily satisfies condition 8.15, so the approximation should be valid for charge motion off a null surface.

The first simulation run used for comparison has an electron started at  $r = 0.2R_{lc}$ ,  $\theta = \pi/8$  radians, and  $\phi = \pi/4$  radians. The charge (in both simulations) hits the null surface rather quickly, in slightly under  $7 \times 10^{-4}$  s (compared to the pulsar period of  $6.02 \times 10^{-2}$  s). The DFB approximation works very well before the charge hits the null surface, as is demonstrated in Figure 8.2. Plots (a) to (c) show the fractional difference between the complete and approximate solutions over the charge path for the  $x$ ,  $y$ , and  $z$  components respectively. These are all tiny, generally less than 0.01%. Plot (d) shows the fractional difference for Lorentz factors between the two simulations, which is somewhat larger, though generally less than 1%.

The second run considers a path which leaves the magnetosphere, but in this case the DFB approximation still gives a good solution. The electron was started again at  $r = 0.2R_{lc}$ , but with  $\theta = \pi/4$  radians and  $\phi = \pi/8$  radians; figure 8.3 shows the fractional differences between the approximate and complete simulation solutions for the  $x$ ,  $y$ , and  $z$  components of the position, as well as the charge energy, in plots (a) through (d). The approximation solves for the position to better than 3% (and generally better than 1%), and for the energy to a few percent.

The DFB approximation does not hold as closely for the slower pulsars, as is suggested by condition 8.15. This is demonstrated by a run for a charge in the fields of a model pulsar with  $\Omega = 1$  rad/s and  $\mu = 10^{30}$  G cm<sup>3</sup> (which does not meet condition 8.15), shown in figure 8.4. The initial position was  $r = R_{lc}$ ,  $\theta = 3\pi/8$  radians, and  $\phi = 3\pi/4$  radians. The solution from the complete simulation is shown with a dashed line in plots (a) through (d),

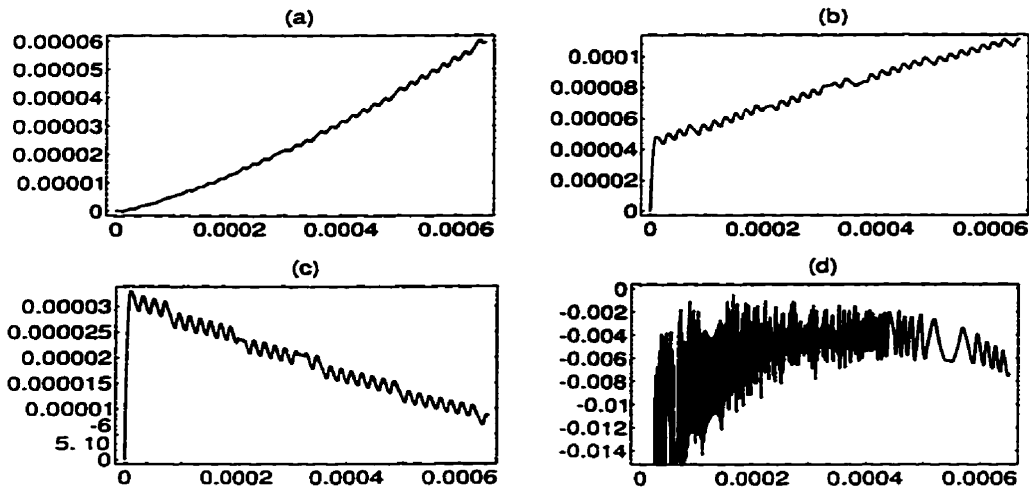


Fig. 8.2: A comparison of the results of the DFB simulation to the more exact complete simulation, for an electron started at  $r = 0.2R_{lc}$ ,  $\theta = \pi/8$  radians, and  $\phi = \pi/4$  radians in the fields of a pulsar with  $\Omega = 100$  rad/s and  $\mu = 10^{30}$  G cm<sup>3</sup>. Plots (a) through (c) show the fractional differences in solutions for the  $x$ ,  $y$ , and  $z$  components of the position respectively, and plot (d) shows the fractional difference in Lorentz factor. The position of the particle agrees to better than 0.01%, and the energy to 1%. With these initial conditions, the charge hits the null surface well inside the light cylinder, where the fields are still very large.



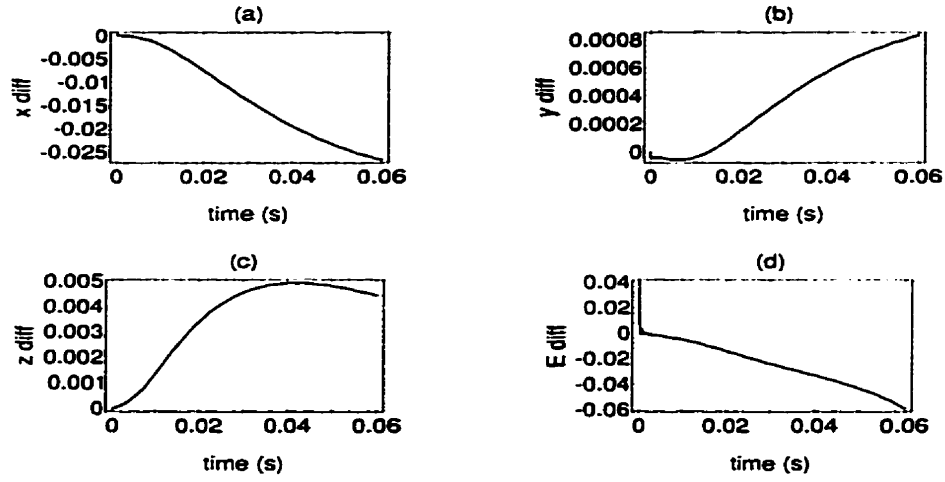


Fig. 8.3: A comparison of the results of the DFB simulation to the more exact complete simulation, for an electron started at  $r = 0.2R_{\text{lc}}$ ,  $\theta = \pi/4$  radians, and  $\phi = \pi/8$  radians in the fields of a pulsar with  $\Omega = 100$  rad/s and  $\mu = 10^{30}$  G cm<sup>3</sup>. Plots (a) through (c) show the fractional differences in solutions for the  $x$ ,  $y$ , and  $z$  components of the position respectively, and plot (d) shows the fractional difference in Lorentz factor. The position of the particle agrees to better than 3%, and the energy to 4%. In this scenario, the charge leaves the magnetosphere without hitting a null surface; the end of the run leaves the charge at approximately  $r = 6R_{\text{lc}}$ .

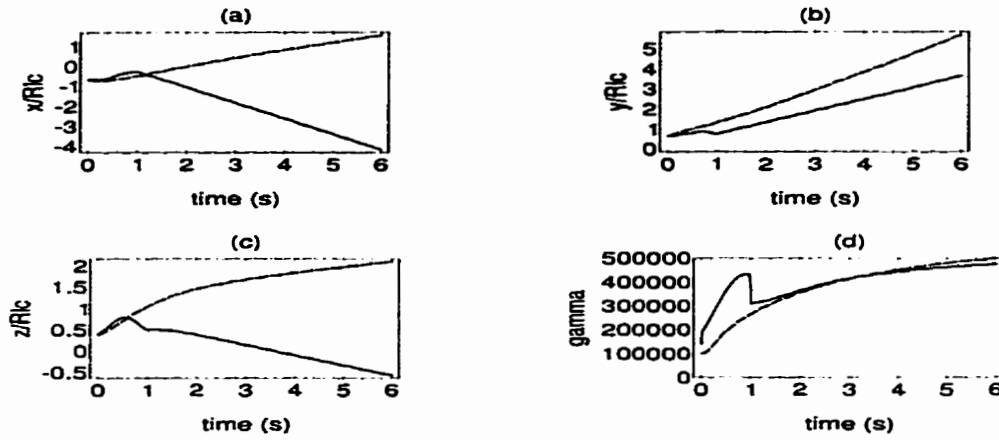


Fig. 8.4: A comparison of the results of the DFB simulation to the more exact complete simulation, for an electron started at  $r = R_{lc}$ ,  $\theta = 3\pi/8$  radians, and  $\phi = 3\pi/4$  radians in the fields of a pulsar with  $\Omega = 1$  rad/s (slower than any of the known gamma-ray pulsars) and  $\mu = 10^{30}$  G cm<sup>3</sup>. Plots (a) through (c) show the  $x$ -,  $y$ -, and  $z$ -components of the position for the complete simulation (dashed lines) and for the DFB simulation (solid lines). Plot (d) shows the Lorentz factor of the particle under the two different simulations. The DFB simulation gives an incorrect solution for the particle motion and energy in this case, as is expected.

and the solution from the DFB simulation with a solid line. The DFB solution is seen to diverge significantly from the complete solution, as is expected in these relatively weak fields.

Since the approximation fails for pulsars with periods representative of the typical population of normal pulsars, its use in simulating these slower objects is limited. However, even for the slowest pulsars, the DFB approximation applies to charge motion well within the light cylinder where the fields are still very large.

## *8.4 Charge Motion on the Null Surface*

The DFB approximation describes the motion of charged particles in the fields of the fast gamma-ray pulsars very well when the charges are not on a null surface. However, when the charges hit one of these surfaces, they lose almost all of their energy to radiation, since there is no longer a component of electric field parallel to the magnetic field to provide energy input.

Charges move quite differently on the two different sorts of null surface; the details of their motion can be quite important in terms of sustaining the vacuum fields, since the charges are confined to a plane and can have quite large charge densities if neutrality is not maintained.

### *8.4.1 Charge Motion on Wired Surfaces*

The charge velocity on a wired null surface has two components: one is the local drift velocity, and the other is a basically undetermined component along the local magnetic field line.

The local drift velocity is given by equation 8.11, which reduces to the regular  $\vec{E} \times \vec{B}$  drift velocity since  $\vec{E}$  and  $\vec{B}$  are perpendicular on the null surface. Since this is generally of order  $r/R_{lc}$ , this component is much less than the speed of light well inside the light cylinder, and generally will be dominated by the component along the magnetic field line.

Since there is no component of  $\vec{E}$  parallel to  $\vec{B}$  on the null surface, there is no preferred direction along the magnetic field line for charge motion. However, since the null surface is

rotating, “centrifugal force” will tend to move the charges out toward the light cylinder. The drift velocity and centrifugal forces affect both types of charge equally, and, for a neutral plasma, will not create any net current which might affect the magnetic fields.

#### 8.4.2 Charge Motion Near a Wired Null Surface

Whether charges are attracted to or repelled from the different sorts of null surfaces is extremely important for the charge dynamics. If a null surface only attracts one sort of charge, it will quickly build up enough charge to alter the fields, since the charges are confined to a two- rather than three-dimensional volume.

By way of demonstration, and because it is central to the problem considered in this thesis, consider the wired null surface in the point dipole fields. In this limit ( $a \ll r \ll R_{lc}$ ), the DFB drift velocity is small compared to the velocity component along the field line; this latter component will dominate the dynamics.

If the charge velocity always forces motion toward the null surface (the  $x = 0$  plane in the coordinates presented in section 7.2.1), then the null surface attracts; otherwise, it repels charge. The charge motion in the  $x$ -direction is dependent on  $B_x$  and the sign of  $q\vec{E} \cdot \vec{B}$ , which determines the direction of motion along the magnetic field line.

In these fields,

$$f = q(\vec{E} \cdot \vec{B})B_x = -\frac{3q\mu^2 x^2 z \sin \chi}{R_{lc} r^7 \sqrt{r^2 + 3z^2}} \quad (8.16)$$

The sign of  $f$  can be seen to be equal to the sign of  $-qz$ , and the sign of  $f$  is also equal to the sign of  $v_x$ . Therefore, for  $z > 0$ , electrons are attracted from negative  $x$  to the null surface and repelled from it from positive  $x$ , and positrons are attracted from positive  $x$  and repelled from negative  $x$ . The opposite is true for  $z < 0$ .

This null surface attracts both positive and negative charges from different parts of the magnetosphere, and therefore will tend to remain electrically neutral. Any slight charge imbalance will create small electric fields along the surface which will restore the balance

without changing the field dynamics too dramatically.

This is a fairly general property of wired null surfaces; the charge dynamics tend to keep them electrically neutral. Obviously, this aspect of the null surface is important in our pulsar model, since it does not tend to create charged surfaces which would alter the electromagnetic fields.

### 8.4.3 Charge Motion on Pierced Surfaces

Charges are attracted to pierced surfaces in a somewhat different manner than to wired surfaces. Near the surface, the charge follows the local drift velocity, but performs ultra-relativistic one-dimensional simple harmonic motion across the surface by oscillating along the magnetic field line direction.

Since there are no simple pierced null surfaces in the Deutsch fields, consider a simple field configuration containing such a surface, with electric and magnetic fields equal to

$$\vec{B} = B\hat{z} \qquad \vec{E} = E_0(\hat{y} + \frac{z}{a}\hat{z}) \qquad (8.17)$$

where  $B$ ,  $E_0$ , and  $a$  are constants (changing the direction of the added electric field off the null surface or changing the form of the variation will not qualitatively affect the results). Then the surface  $z = 0$  is a pierced null surface, and charges on this surface move with a drift velocity  $E_0/B\hat{x}$ . They are still free to move along the magnetic field line, however, but there is a linear restoring force (for negative charges) which returns the charge to the surface. Note that the electric field acts quite differently for positive charges: these are repelled from the null surface everywhere. Pierced null surfaces can only attract *one* sign of charge.

A negative charge, then, will perform simple harmonic motion along the magnetic field line, and follow the  $\vec{E} \times \vec{B}$  drift velocity in the null surface, as long as the amplitude of the oscillations is much less than  $a$  (otherwise, the drift velocity would change).

If the charge is ultra-relativistic for most of its oscillation, the analysis is simplified considerably. Also, if  $E_0 \ll B$ , the drift velocity can be ignored for the purpose of determining

the parameters of the oscillation.

For this sort of ultra-relativistic simple harmonic motion (URSHM), energy conservation is the most direct route to a solution. Assuming that the charge's energy as it crosses the null surface is  $\gamma_0 mc^2$ , the amplitude of the oscillation is:

$$A = \sqrt{2\gamma_0 mc^2 a} \quad (8.18)$$

and the period (found by assuming the charge is always moving almost at the speed of light) is:

$$T = \frac{4A}{c} = \sqrt{32\gamma_0 ma} \quad (8.19)$$

The frequency of oscillation in the ultra-relativistic limit can be compared to that in the non-relativistic limit by setting  $k = 1/a$  as the effective "spring constant"; letting  $m' = \gamma_0 m$  be the effective relativistic mass,

$$\omega_{\text{ur}} = \sqrt{\frac{\pi^2}{8}} \sqrt{\frac{k}{\gamma_0 m}} = \sqrt{\frac{\pi^2}{8}} \omega_{\text{nr}} \quad (8.20)$$

where  $\omega_{\text{ur}}$  is the frequency for URSHM, and  $\omega_{\text{nr}}$  is the frequency for NRSHM, with  $m$  replaced by  $m'$ .

As mentioned earlier, pierced null surfaces only attract one sign of charge, depending on the orientation of the electric field on either side of the surface. Charge can build up on such surfaces and alter the vacuum fields. Fortunately, no pierced null surfaces which attract only one sign of charge are sustained over a significant spatial extent exist in the Deutsch fields, and they are not important to the field structure; for example, section 7.4.3 discusses the pierced null surface near the star which attracts electrons in some places and positrons in others. A charge attracted to one area will flow along the surface until it encounters an area where it is repelled, and then is ejected from the surface.

## 8.5 *Types of Charge Motion in the Deutsch Fields*

When charges are *not* on a null surface, their motion is well described by the DFB approximation; when on a null surface, the charges move as described above.

The paths observed in the simulation runs can be grouped into three categories:

- **Outgoing Paths:** These paths move fairly directly from their starting point to infinity without hitting a null surface. They contribute the majority of the radiation from the pulsar. If a charge started well inside the light cylinder passes through the light cylinder without encountering a null surface, it will invariably be following an outgoing path. Only a small fraction of paths are outgoing.
- **Ingoing Paths:** These paths hit the star without encountering a null surface. Most are quite short, though some (which follow field lines near the boundary between open and closed field lines) can extend for some distance. Since these paths are quite curved, particles following these paths can radiate quite powerfully.
- **Stopped Paths:** These paths hit a null surface before leaving the magnetosphere or hitting the star, and, along with ingoing paths, form the majority of the paths seen in the simulation for charges started with  $r > 0.1R_{lc}$ . The paths are generally quite short, leaving little time for the charges to radiate.

The simulation results show that, in the Deutsch fields, there are *no* outgoing paths for charges started with  $r < 0.1R_{lc}$ . The paths are a mix of stopped paths and ingoing paths, which suggests that charges created inside this sphere will not escape readily except as a low-energy neutral plasma along the null surface.

## 8.6 *The Inner and Outer Magnetospheres*

A key concept of our model is that the magnetosphere can be roughly divided into two regions: the inner and outer magnetospheres. The inner magnetosphere is defined as a

sphere of radius  $r = 0.1R_{lc}$ , inside which the charge density is large enough to alter the fields. It is assumed that, inside this region, the charge density equals the Goldreich-Julian charge density - that is, the plasma co-rotates with the star. In fact, from the point of view of the generated fields, the inner magnetosphere is *indistinguishable* from the star.

The outer magnetosphere is assumed to be entirely evacuated; therefore, the electromagnetic fields in this region are the Deutsch fields, but using  $0.1R_{lc}$  for the “stellar” radius. This region is where the gamma-radiation is generated, as the charges move at extremely high energies (generally with Lorentz factors of several  $\times 10^7$ ).

This distinction is crucial to a model which is consistent with radio observations; without a high-density plasma, the radio waves (which require a coherent plasma process) would not be generated. It is a fairly rough approximation, both in terms of the cut-off in corotation charge density at the boundary between the inner and outer magnetosphere and in the shape of the inner magnetosphere; however, it does capture some of the basic physics of the situation. The inner magnetosphere may be required to generate the small charge density in the outer magnetosphere (much less than the Goldreich-Julian charge density to maintain vacuum) which produces the gamma-radiation; this point is discussed in chapter 10.

## 8.7 Charge Energetics

The DFB approximation generally gives the particle paths to high accuracy; however, so far little has been said about the charge energies along those paths.

The energy as a function of time can be found by integrating the power, expressed as the charge’s Lorentz factor:

$$\frac{d\gamma}{dt} = \frac{q}{mc} \vec{E} \cdot \vec{\beta} - P_{\text{rad}} \quad (8.21)$$

where  $P_{\text{rad}}$  is the radiative power loss; as mentioned earlier, equation 8.6 was used for radiative power in these simulations.

If the electric fields are strong enough and act to increase the energy of a charge, the



radiation reaction force will act like a thermostat, fixing the particle's energy at a particular value for a given electric field. That is, if the particle's energy rises above the equilibrium value, the radiative power increases above the power input due to the electric field, and the charge loses energy. If its energy is below the equilibrium value, the radiative power drops below the power input from the electric field, and the charges energy increases. If the electric field acts to decrease the energy of a charge, it will quickly stop and accelerate in the opposite direction, and the thermostat will become operational.

This equilibrium value can be found by setting the power input due to the electric field equal to the radiative power loss:

$$\frac{e}{mc} E_{\parallel} = P_{\text{rad}} = \frac{2}{3} \frac{e^2 c}{\rho^2} \gamma_{\text{eq}}^4 \quad (8.22)$$

and therefore

$$\gamma_{\text{eq}}^4 = \frac{3}{2} \frac{\rho^2}{emc^2} E_{\parallel} \quad (8.23)$$

Here  $E_{\parallel}$  is the component of  $\vec{E}$  parallel to the charge's velocity.

When the electric field is large enough that this process is efficient, the charge is called "radiation reaction limited". This occurs when the timescale for the electric field to accelerate the charge to  $\gamma_{\text{eq}}$  is much less than the characteristic timescales of the problem; for a pulsar, it must be much less than the pulsar period  $T = 2\pi/\Omega$ .

The magnitude of the electric field in the outer magnetosphere of the Deutsch pulsar, where there is a significant component of  $\vec{E}$  parallel to  $\vec{B}$ , is roughly

$$E \simeq \frac{\mu}{u^2 R_{\text{lc}}^3} = \frac{\mu \Omega^3}{u^2 c^3} \quad (8.24)$$

where  $u = r/R_{\text{lc}}$ . Using this value for  $E_{\parallel}$ , the equilibrium Lorentz factor is

$$\gamma_{\text{eq}} = \left( \frac{3}{2} \frac{\Omega \mu}{ec} \right)^{1/4} \simeq 5.7 \times 10^7 \left( \frac{\Omega}{100 \text{ rad/s}} \right)^{1/4} \left( \frac{\mu}{10^{30} \text{ G} - \text{cm}^3} \right)^{1/4} \quad (8.25)$$

which does not depend on  $u$ . Therefore, the charges move with roughly constant energy through the magnetosphere; however, the form of equation 8.24 is an oversimplification of the true fields, and the component parallel to the velocity will vary.

The timescale  $\tau_{\text{rf}}$  required to accelerate a charge from low energy to  $\gamma_{\text{eq}}$  in these fields, as a fraction of the pulsar period  $T$ , is

$$\frac{\tau_{\text{rf}}}{T} = 1.4 \times 10^{-3} u^2 \left( \frac{\Omega}{100 \text{ rad/s}} \right)^{-7/4} \left( \frac{\mu}{10^{30} \text{ G} \cdot \text{cm}^3} \right)^{-3/4} \quad (8.26)$$

For a pulsar with  $\mu = 10^{30} \text{ G} \cdot \text{cm}^3$  at the light cylinder ( $u = 1$ ),  $\tau_{\text{rf}} \approx T$  at an angular frequency of  $\Omega = 0.08 \text{ rad/s}$ , and therefore the approximation that the charges are radiation reaction limited is a very good one for all the known gamma-ray pulsars.

## 9. THE DEUTSCH FIELD PULSAR MODEL

This chapter builds on the results of the last two chapters and lays out the framework for a new model of gamma-ray emission from pulsars. It is a roughly self-consistent model, where the gamma-ray emission is generated in the evacuated outer magnetosphere and the radio emission is created in the inner magnetosphere.

We make a set of assumptions about the global magnetospheric structure that differs from past models: we assume that the charge density is very small in the outer magnetosphere, and that the inner magnetosphere can be treated as a spinning, highly magnetised and conducting sphere in vacuum (the electromagnetic fields around such a star were derived by Deutsch 1955). This assumption is justified in our model because we find that any charges created in the inner magnetosphere follow paths constrained to stay close to the star. They are thus unable to populate the outer magnetosphere and short out the electric fields (the distinction between the inner and outer magnetosphere was elaborated in section 8.6).

By so fixing the fields, particle motion can be integrated relatively easily, and the radiation observed from the model pulsar can be estimated fairly accurately. With low number densities, inverse Compton scattering and photon/photon interactions are unlikely, and synchrotron emission is not important, so curvature radiation is the only source of emission. The back reaction on the particles of the curvature emission is included in the determining the particle energies.

## 9.1 Radiation Processes in the Deutsch Fields

### 9.1.1 Particle-Photon and Photon-Photon Interactions

This model assumes that the only emission contributing to the light curves is a result of curvature radiation by the high-energy particles moving along curved paths in the magnetosphere. This is justified as long as the number densities of charges are small; how small can be roughly calculated by examining the mean free path of photons subject to Compton scattering off electrons and to self-scattering.

#### *Inverse Compton Scattering*

The cross-section for Compton scattering (or inverse Compton scattering) is approximately equal to the Thompson scattering cross-section for photon energies in the electron rest frame much less than the electron rest mass. For photon energies in this frame much greater than the electron rest mass, the cross-section is approximately  $\frac{3}{4}\sigma_{\text{T}}mc^2/E_{\gamma}$  (Jackson (1975)). Therefore, the Thompson cross-section will be used as an upper limit to the cross-section (although this neglects resonant interactions with the magnetic field, which can increase the cross-section by several orders of magnitude above the Thompson value for a limited energy range - see, for example, Daugherty & Harding 1991).

The optical depth of the magnetosphere to inverse Compton scattering for a photon is then approximately

$$\tau_{\text{ICS}} \simeq n_e \sigma_{\text{T}} R_{\text{lc}}$$

where  $n_e$  is an average electron density,  $\sigma_{\text{T}} = 6.65 \times 10^{-25} \text{ cm}^2$  is the Thompson scattering cross-section, and  $R_{\text{lc}} = c/\Omega$  is the light cylinder radius.

The number density of photons in the magnetosphere can be roughly estimated from the power output of each electron  $P_e$ , the average photon energy  $E_{\gamma}$ , and the characteristic time the photons are within the magnetosphere  $1/\Omega$  as

$$n_\gamma \simeq \frac{P_e}{\Omega E_\gamma} n_e \quad (9.1)$$

To ensure that the number of photons which scatter off electrons is much less than the number of electrons,

$$n_\gamma \tau_{\text{ICS}} \ll n_e$$

This puts a limit on the number density of electrons of

$$n_e \ll \frac{\Omega^2 E_\gamma}{\sigma_T c P_e} \quad (9.2)$$

For relativistic motion on a path with radius of curvature  $\rho$ , the power and average frequency of curvature emission can be written (e.g., Jackson 1975)

$$P_e = \frac{2}{3} \frac{e^2 c}{\rho^2} \gamma^4 \quad (9.3)$$

$$E_\gamma \simeq \hbar \frac{c}{\rho} \gamma^3 \quad (9.4)$$

where  $\gamma$  is the charge's Lorentz factor and  $e$  its charge.

Substituting these into inequality (9.2),

$$n_e \ll \frac{\hbar \Omega}{\sigma_T e^2 \gamma} \quad (9.5)$$

The Lorentz factor of particles can be estimated from the fields (see equation (8.14)) by equating the power output from radiation with the power input from the electric field. Roughly, this gives

$$\gamma^4 \simeq \frac{\Omega \mu}{ec}$$

This can be used to define an upper limit to a combination of the stellar parameters below which this model remains applicable by setting the Goldreich-Julian number density

equal to the limit of equation (9.5) (the number densities must always be much less than the Goldreich-Julian number density). Using the expression for  $\gamma$  above, the condition for negligible scattering is

$$\Omega^{\frac{13}{4}} \mu^{\frac{5}{4}} \ll 3.3 \times 10^{49} \quad (9.6)$$

For example, with a magnetic dipole moment of  $10^{30}$  G cm<sup>3</sup> (giving a surface magnetic field of approximately  $10^{12}$  G), the upper limit on  $\Omega$  is approximately 5000 rad/s, much larger than any standard pulsar spin rates. Thus, for the population of normal pulsars, the Goldreich-Julian number density is not sufficient to ensure significant Compton scattering. This assumes that the only photons are the gamma-ray photons generated by the charges; a high flux of x-ray-energy photons from the inner magnetosphere might change these assumptions.

#### *Photon-Photon Scattering*

A similar calculation can be done for the case of photon-photon scattering, where the cross-section above the pair production limit is again maximally of order the Thompson cross-section. For the spectrum to remain unperturbed as it leaves the magnetosphere,

$$\tau_{\gamma-\gamma} \ll 1$$

where  $\tau_{\gamma-\gamma} = n_{\gamma} \sigma_{\text{T}} R_{\text{lc}}$ . This gives exactly the same constraint on the electron number density and on the angular velocity and dipole moment (equation (9.6)) as the inverse Compton scattering criterion above.

While the fraction of photons affected by photon-photon scattering is rather small, the photons which do interact create charges in the magnetosphere. This could provide a source for the charges, though a more complex calculation is required to properly examine the viability of this option (see sections 9.5.1 and 10.1 for some discussion of this problem).

### 9.1.2 *Synchrotron Radiation*

Under the DFB approximation, charges move parallel to the magnetic field line in a frame where the electric and magnetic fields are parallel. The timescale to radiate away perpendicular momentum through synchrotron radiation is very short, so there is no sustained emission. However, if there is pair production throughout the outer magnetosphere, the new charges will be created with velocities at angles to the local magnetic field and will radiate the perpendicular momentum away, possibly contributing significantly to the overall emission. This effect is not included in the present model.

## 9.2 *Outline of the Model*

The charge density in the outer magnetosphere is taken to be much less than the Goldreich-Julian charge density, as charges created in the inner magnetosphere ( $r < 0.1R_{lc}$ ) are either bound to the inner magnetosphere or flow out of the magnetosphere as a low-energy neutral plasma on the null surface.

With this justification of the vacuum assumption for the magnetosphere, the basic model can be defined as a rough approximation to a global self-consistent solution to the pulsar problem. The outer magnetosphere ( $r > 0.1R_{lc}$ ) is the region of particle acceleration, where charges can be ejected from the magnetosphere. The only radiation which is important is curvature radiation, for the reasons discussed earlier.

Particles radiate gamma-ray photons, some toward the star, where they create electron-positron pairs on the powerful magnetic fields in the inner magnetosphere. These charges are all bound on closed paths to the inner magnetosphere, and cannot populate the outer magnetosphere to short out the large electric fields. A charge balance is established by having charges being created near the star and flowing out with low energies along the null surfaces. The effect of the outflowing charges on the fields is neglected, as the null surface attracts both positive and negative charges which flow with the same drift, creating a neutral plasma.

Since the paths of the charges are all bound for radii  $r < 0.1R_{ic}$ , charges were started on a sphere of radius  $0.2R_{ic}$  (called the “starting sphere”) at intervals of  $\pi/16$  radians in the toroidal and poloidal angles to fully sample the range of initial starting positions. The starting energies were unimportant, since the charges immediately move to balance radiation power out with electric field power in. The source for these charges is left undetermined.

The radiation from these trajectories was calculated and binned to build up light curves and spectra for different viewing directions; this is discussed in detail in sections 9.3 and 9.6.

To simplify the numerical calculation, we took advantage of the three symmetries of the Deutsch fields described in section 7.5.

Symmetry 1 means than runs need be done only for particle starting points in the top half of the magnetosphere; paths in the bottom half are reflections of those in the top half. A consequence of Symmetry 3 is that charges started at a time  $t_0 \neq 0$  can be found from the paths started at  $t_0 = 0$  by a rotation azimuthally. Symmetry 2 means that positron paths can be inferred from electron paths, but only in the orthogonal Deutsch fields.

The combination of Symmetry 2 and Symmetry 3 has an important consequence for the inferred light curves when the dipole moment is perpendicular to the rotation axis: positrons will radiate in exactly the same manner as electrons, but a half period later. If the electron contribution is a single peak, the positrons will contribute a second peak, exactly 0.5 later in phase, if the distribution of positrons is equal to that of electrons in the magnetosphere. This does not hold for non-orthogonal systems, as Symmetry 2 is broken.

### 9.3 *Light Curve Generation*

With paths of all the charges known, a pattern of radiative emission for different retarded times  $\tau$  ( $\tau = t - \hat{n}_{obs} \cdot \vec{r}/c$ , with  $\hat{n}_{obs}$  a unit vector pointing toward the observer) could be generated.

A numerical routine stepped along the paths for each of the different starting angles, and for 100 steps in starting angle  $t_0$ . The emission from paths in the bottom half of the



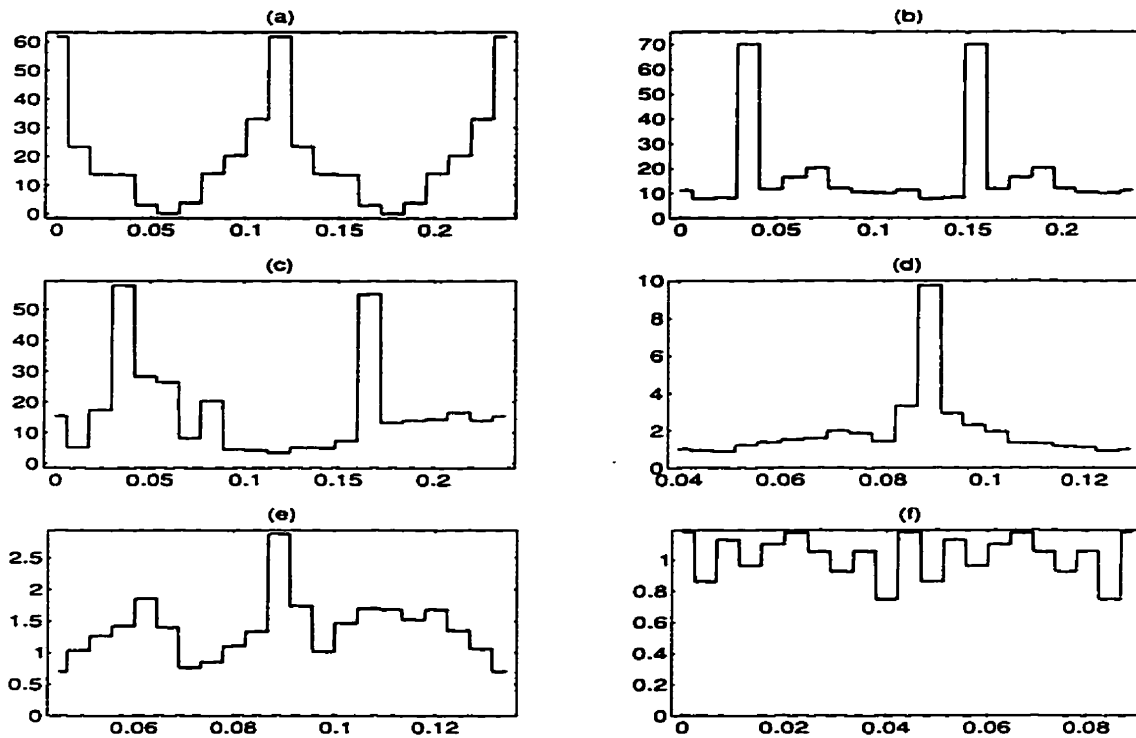


Fig. 9.1: Representative light curves produced by the model for different viewing directions, spin rates, field strengths, and dipole inclinations. See the text for a complete discussion. Time is plotted along the horizontal axis, and arbitrary intensity along the vertical. All plots have radio peaks at  $\tau = 0$  and/or  $\tau = \pi/\Omega$ , presuming the radio emission to be generated close to the star and near the pole. Plot (d) is shown offset in time to show the single peak more clearly.

magnetosphere (and for positron paths when considering orthogonal fields) was included by inferring their paths from the three symmetries discussed earlier.

Since the emission generated is only for a single electron started at  $(\theta, \phi)$  on the starting sphere and at time  $t_0$ , the power must be scaled by a distribution function  $f_{e,p}$  of charges over the starting sphere and over starting time, where  $f_{e,p}d\Omega dt_0$  is the number of charges (either electrons or positrons) flowing through the starting sphere between solid angle  $\Omega$  and  $\Omega + d\Omega$  at times between  $t_0$  and  $t_0 + dt_0$ . This distribution function can be varied to model different sources; however, since most emission comes from the outgoing paths, which only originate on a small region of the starting sphere, changes in  $f_{e,p}$  do not much affect the light curves. Throughout this work,  $f_e = f_p = f$  for the light curve generation; the actual value of  $f$  is constrained by the total power emitted by the pulsar, and sets the number density at the starting sphere.

The spectrum of the radiation at one point along a path, for a given particle Lorentz factor and path radius of curvature, is assumed to be instantaneously that for circular motion; this is discussed in section 9.6 The emitted radiation was calculated at several different frequencies to capture the spectrum at each time on the light curve.

The emitted power was binned into angular bins of  $\pi/16$  radians in azimuthal and polar viewing angles, bins of  $T/20$  in  $\tau$  (where  $T$  is the pulsar period), and bins of 0.25 in  $\log \omega$ , where  $\hbar\omega$  is the photon energy. Any emission which was beamed through the inner magnetosphere ( $r < 0.1R_{lc}$ ) was not included in the light curves, as it was assumed to have been absorbed in the denser plasma near the star.

Figure 9.1 shows some representative 1 MeV light curves generated by the model, which cover many of the variations seen in the observed gamma-ray pulsar light curves. Plots (a) and (b) correspond to a Geminga-like pulsar, with an angular velocity of  $\Omega = 26.5$  rad/s and a magnetic dipole moment of  $\mu = 10^{30}$  G cm<sup>3</sup> aligned perpendicular to the rotation axis. The first is for a viewing angle of  $\theta_v = 84.4^\circ$ , and the second represents radiation into  $\theta_v = 50.6^\circ$ . These show the characteristic symmetry between the first and second halves of the

light curve due to the action of Symmetry 2 in the orthogonal field. Light curve (c) is for the same Geminga-like pulsar, but with the dipole moment inclined at  $45^\circ$  to the rotation axis, seen at a viewing angle of  $73^\circ$ . The two main peaks are separated by a phase of 0.45. (d), (e), and (f) all correspond to emission from a Vela-like pulsar, with  $\Omega = 70.6$  rad/s and  $\mu = 3.7 \times 10^{30}$  G cm<sup>3</sup>. The dipole moment in (d) and (e) is nearly aligned at only  $11.25^\circ$  to the rotation axis; (f) corresponds to orthogonal fields. (d) represents emission into a viewing angle of  $16.9^\circ$ , and shows a well-defined single peak. (e) is seen from a viewing angle of  $61.9^\circ$  and shows three quite well-defined peaks (there is a suggestion of a triply-peaked light curve for PSR B1706-44, though two of the peaks appear to be quite close in phase, unlike in our plot - Thompson *et al*, 1995a). (f) is seen from a viewing angle of  $39.4^\circ$ , and shows no discernable pulsation at frequencies less than 50 GeV. This pulsar would likely be missed in a pulsar survey.

All the plots discussed relate to emission beamed into  $\phi_v = 0$ ; one of the poles points toward the observer at  $t = 0$  at this angle. The light curves for  $\phi_v \neq 0$  are identical except for a phase change. For all these plots, the radio emission peaks (presumed to come from the poles near the star) would be seen at  $\tau \simeq 0$  and/or  $\tau = \pi/\Omega$ ; the gamma-ray peaks are significantly displaced in some cases, while in others they align quite closely.

## 9.4 Light Curve Structure

The light curves generated by this numerical procedure often show quite thin, tall peaks, which are not observed in the data. These peaks are generally caused by ingoing paths which penetrate a significant distance into the outer magnetosphere, radiating quite powerfully as they follow the curved magnetic field line.

These paths are often quite close to the boundary between the open and closed magnetic field lines (closed field lines close inside the light cylinder, and open field lines close outside). Paths started close together in the region of the starting sphere containing the feet of the open field lines can diverge quite significantly as they move out into the outer magnetosphere.

The area of the starting sphere which contains the feet of the open field lines is quite small, and the numerical routine does not treat this region any differently than others; a better procedure would reduce the grid size here to capture the divergence of the paths. Adding this feature to the calculation may cause the thin peaks seen in the light curves to spread out, both in phase and in emitting angle.

## 9.5 Total Emitted Power

The total power emitted into all directions by the electrons or positrons at any time  $t$  is given by:

$$P_{e,p}(t) = \int_{\Omega} \int_{t_0} [f_e \hat{P}_e + f_p \hat{P}_p] d\Omega dt_0 \quad (9.7)$$

where  $\hat{P}_{e,p}(\theta, \phi, t_0; t - t_0)$  is the power output of one electron (e) or positron (p) at time  $t - t_0$  along the path, started at  $(\theta, \phi)$  on the starting sphere at time  $t_0$ .  $f_{e,p}$  are the distribution functions of charges on the starting sphere, which is not fixed in the model.

### 9.5.1 The Required Number Density

If the total high-energy power output of a pulsar is known, this fact can be used to estimate the number density of charges at the starting sphere required to supply that energy. If this number density is larger than the Goldreich-Julian number density, the fields will be altered and the model will break down.

Taking a constant distribution  $f_e = f_p = f$ , the total energy radiated in one period is given by

$$E = f \int_{\Omega} \int_{t_0} \int_t (\hat{P}_e + \hat{P}_p) dt dt_0 d\Omega \quad (9.8)$$

Since the radiation reaction force fixes the radiated power to be very closely equal to the power input from the electric field,

$$\hat{P}_{e,p} = e\vec{E} \cdot \vec{v}_{e,p} = ec\frac{\mu\Omega^3}{c^3}\vec{E} \cdot \vec{\beta}_{e,p} \quad (9.9)$$

where  $\vec{E}$  is a dimensionless electric field which no longer depends on the values of  $\mu$  and  $\Omega$ , and  $\vec{\beta}_{e,p} = \vec{v}_{e,p}/c$ .

Defining  $\tau_0 = \Omega t_0$  and  $\tau = \Omega t$ , the total energy emitted in a period can now be written

$$E_{\text{tot}} = f\frac{e\Omega\mu}{c^2}\mathcal{E} \quad (9.10)$$

where  $\mathcal{E}$  is a dimensionless function of the dipole inclination angle  $\chi$  alone:

$$\mathcal{E} = \int_{\Omega} \int_{\tau_0=0}^{2\pi} \int_{\tau=0}^{2\pi} \vec{E} \cdot (\vec{\beta}_e + \vec{\beta}_p) d\Omega d\tau_0 d\tau \quad (9.11)$$

For example,  $\mathcal{E} = 36$  for the orthogonal fields, and 6.8 for  $\chi = 11.25^\circ$ .

Since the total gamma-ray power output from the model (integrated over all emitting directions) must be constant with time, the total energy emitted in a period is equal to  $P_{\text{obs}}\frac{2\pi}{\Omega}$ , where  $P_{\text{obs}}$  is the observed gamma-ray power.

The value of  $f$  can then be related to the observed power output:

$$f = \frac{2\pi c^2 P_{\text{obs}}}{e\Omega^2 \mu \mathcal{E}} \quad (9.12)$$

The value of  $f$  sets the number density at the starting sphere required to produce the observed power output, since  $f = 4\pi c(0.2R_{\text{lc}})^2 n$ . Therefore,

$$n = \frac{25P_{\text{obs}}}{2ec\mu\mathcal{E}} \quad (9.13)$$

The number density can be described somewhat more meaningfully as a fraction of the Goldreich-Julian number density (equation (1.6)) at the starting sphere ( $\mathcal{E}$  is taken to be equal to 36, the value for the orthogonal fields).

$$\frac{n}{n_{GJ}} \simeq 4.7 \times 10^{-5} \text{cm}^{-3} \left(\frac{P_{\text{obs}}}{10^{34} \text{ergs/s}}\right) \left(\frac{\Omega}{100 \text{rad/s}}\right)^{-4} \left(\frac{\mu}{10^{30} \text{Gcm}^3}\right)^{-2} \quad (9.14)$$

Pulsar	$P$	$\dot{P}$	$\mu$	$P_{\text{tot}}$	$n/n_{\text{GJ}}$	Reference
Geminga	0.237	11.0	1.63	$5.7 \times 10^{33}$	$2.1 \times 10^{-3}$	Mayer-Hasselwander <i>et al</i> 1994
Vela	0.0893	125	3.4	$1.6 \times 10^{35}$	$2.7 \times 10^{-4}$	Kanbach <i>et al</i> 1994
Crab	0.0333	421	3.8	$3.7 \times 10^{35}$	$9.8 \times 10^{-6}$	Ulmer <i>et al</i> 1995
PSR1509-58	0.150	1540	15	$1.1 \times 10^{36}$	$7.3 \times 10^{-4}$	Laurent <i>et al</i> 1994
PSR1706-44	0.102	93.0	3.1	$1.6 \times 10^{35}$	$5.5 \times 10^{-4}$	Thompson <i>et al</i> 1992
PSR1055-52	0.197	5.8	1.1	$5.9 \times 10^{34}$	$2.4 \times 10^{-2}$	Fierro <i>et al</i> 1993
PSRB1951+32	0.0395	5.85	0.49	$7.9 \times 10^{34}$	$2.5 \times 10^{-4}$	Ramanamurthy <i>et al</i> 1995

Tab. 9.1: Number densities at the starting sphere required to give the observed power outputs for the known gamma-ray pulsars, as a fraction of the Goldreich-Julian number density. Periods  $P$  are given in seconds, period derivatives  $\dot{P}$  in  $10^{-15}$  s/s, dipole moments  $\mu$  in units of  $10^{30}$  G cm<sup>3</sup>, and gamma-ray power outputs  $P_{\text{tot}}$  in ergs/s. All known high-energy pulsars have  $n/n_{\text{GJ}} \ll 1$ , though PSR 1055-52 is somewhat marginal. All estimates of average power assume beaming into a solid angle of  $2\pi$ .

This quantity is tabulated in Table 9.1 for the known gamma-ray pulsars, and is less than unity, and therefore consistent with the model, in all cases. The values of  $\mu$  were calculated with equation (7.12) taking  $\sin \chi = 1$  (and are therefore a lower limit), and the average powers were calculated by estimating beaming into a solid angle of  $2\pi$  (this means power averaged over a period, which by definition is uniform in  $\phi$ ).

The most serious weakness of this model is the lack of a clear source for the charge on the starting sphere. This is a complicated problem related to the physics of the inner magnetosphere and to pair creation due to photon-photon interactions (while these have negligible effect on the shape of the spectrum, the small fraction of interactions may be enough to supply the charge).

To resolve this problem with the model, we present an outline of a possible source for the charges which is consistent with the observations.

The charges are presumed to be created due to photon-photon pair creation in the inner magnetosphere, preferentially at small radii due to larger charge (and therefore photon) density. To roughly quantify this model, an order of magnitude estimate of the charge density will be presented; however, to properly understand the physics of the process, a more complex calculation needs to be made. This is meant only as an illustration of a possible physical process.

The number density of charges created by photon-photon pair production is roughly

$$n_{e\pm} \simeq n_\gamma^2 \sigma_T R_{lc} \quad (9.15)$$

If the charges are the source of the high-energy photons, which pair-create on themselves,

$$n_\gamma \simeq \frac{P_\gamma}{\Omega E_\gamma} n_e \quad (9.16)$$

and  $n_{e\pm} \simeq n_e$ .

Using  $P_\gamma$  and  $E_\gamma$  as per equations 9.3 and 9.4, and assuming the particles to be radiation-reaction limited, this reduces to

$$n_e \simeq 4 \times 10^{18} \Omega^{0.5} \mu^{-0.5} \quad (9.17)$$

In terms of the Goldreich-Julian number density at the starting sphere,

$$\frac{n_e}{n_{GJ}} \simeq 7 \times 10^{-3} \left( \frac{\Omega}{100 \text{ rad/s}} \right)^{-3.5} \left( \frac{\mu}{10^{30} \text{ G} - \text{cm}^3} \right)^{-1.5} \quad (9.18)$$

This functional dependence on  $\Omega$  and  $\mu$  can be fit to the data from the observed pulsars to find a proportionality of best fit.

$$\frac{n_e}{n_{GJ}} \simeq 4.4 \times 10^{-4} \left( \frac{\Omega}{100 \text{ rad/s}} \right)^{-3.5} \left( \frac{\mu}{10^{30} \text{ G} - \text{cm}^3} \right)^{-1.5} \quad (9.19)$$

The normalisation is only off by a factor of 16 from the naive estimate of equation 9.18, and gives an excellent fit to the observations. The only observed pulsar which falls off the fit line is Geminga - this could be due to a beaming effect or to an underestimate for the distance to this object (157 pc is used throughout).

However, since the errors on the data points in the fit are fairly large (roughly a factor of six due to uncertainties in the stellar moment of inertia and the distance), there is quite a broad range of power law exponents that will fit the data well. Figure 9.2 shows a likelihood plot for a fit of the form

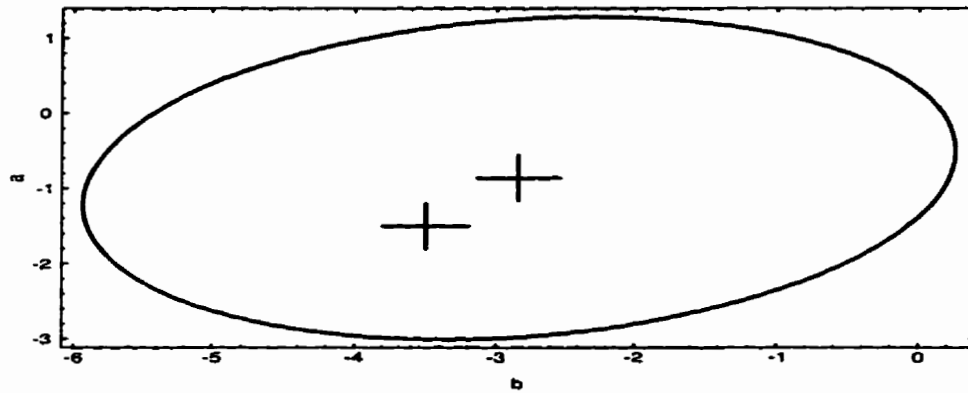


Fig. 9.2: Likelihood plot for the power-law exponents in the fit to the required number density at the starting sphere as a fraction of the Goldreich-Julian charge density. The curve encloses the  $1\sigma$  likelihood region; the extent of the region is quite broad, showing that the data do not significantly constrain the fit parameters. The two crosses show the best-fit point at ( $a = -0.86$ ,  $b = -2.84$ ) and the estimate from self-consistent pair creation through pair radiation at ( $a = -1.5$ ,  $b = -3.5$ ).



$$\frac{n_e}{n_{\text{GJ}}} = A \left( \frac{\mu}{10^{30} \text{G} - \text{cm}^3} \right)^a \left( \frac{\Omega}{100 \text{rad/s}} \right)^b \quad (9.20)$$

where the contour shows the  $1\sigma$  confidence level for the power-law exponents  $a$  and  $b$ . The best fit occurs at  $a = -0.86$ ,  $b = -2.84$ , but  $a = -1.5$  and  $b = -1.5$  is well within the bounds. The extent of the allowed region shows that the data do not constrain the fit to any real extent, which is not surprising with only seven points and relatively large uncertainties. However, the hypothesis that the number density is *equal* to the Goldreich-Julian charge density (corresponding to  $a = b = 0$ ) is somewhat unlikely (only a 30% chance that this is correct)

The extinction of gamma-ray emission occurs when the number density approaches the Goldreich-Julian number density, as the fields in the outer magnetosphere short out and charges are no longer accelerated to the required energies. For a pulsar with  $\mu = 10^{30} \text{ G cm}^3$ , using equation 9.19, this occurs as  $\Omega \rightarrow 11 \text{ rad/s}$ , or as the period approaches 0.57 sec. This suggests that a significant fraction (roughly half) of the population of ordinary pulsars can be gamma-ray emitters, though most at relatively low power.

### 9.5.2 The Gamma-Ray Efficiency

The gamma-ray efficiency of a pulsar is defined as the ratio of the power output in gamma-rays to the total energy loss. For the Deutsch field pulsar, the rate of rotational energy loss is

$$P_{\text{rot}} = \frac{2\Omega^4 \mu^2 \sin^2 \chi}{3c^3} \quad (9.21)$$

$$\simeq 2.5 \times 10^{-32} \Omega^4 \mu^2 \quad (9.22)$$

and the gamma-ray power emitted in our model is given by

$$P_\gamma = \frac{2\mathcal{E}}{25} e c \mu n \quad (9.23)$$

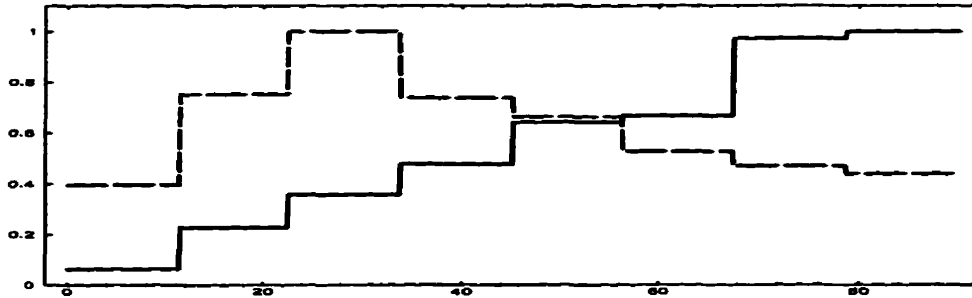


Fig. 9.3: Distribution of emitted power at 1 MeV with viewing angle for two Vela-like pulsars. The solid line shows the power emitted by a pulsar with orthogonal fields, and the dashed line shows the corresponding curve for a pulsar with a dipole axis inclined at  $11.25^\circ$  to the rotation axis. The axes show viewing angle in degrees on the horizontal and emitted power scaled to unity at the maxima on the vertical.

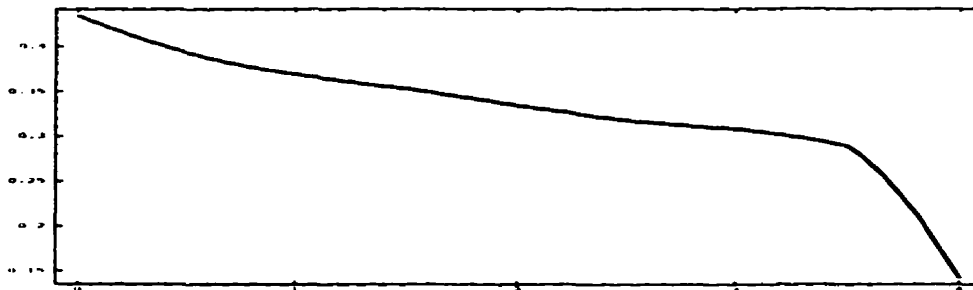


Fig. 9.4: The variation of  $\Omega_p$ , the fractional solid angle into which radiation is beamed, is shown for a Geminga-like pulsar with a dipole moment inclined at  $22.5^\circ$  to the rotation axis. The pulsar becomes significantly less observable at higher frequencies. Similar results are obtained for pulsars with different model parameters. The axes show the base-10 logarithm of the photon energy in MeV along the horizontal, and the value of  $\Omega_p$  along the vertical.

Setting  $\mathcal{E} = 36$  (orthogonal fields) and writing  $n$  in terms of the Goldreich-Julian number density  $n_{\text{GJ}}$ , the gamma-ray efficiency is

$$\eta_\gamma = \frac{P_\gamma}{P_{\text{rot}} + P_\gamma} \simeq \frac{83 \frac{n}{n_{\text{GJ}}}}{1 + 83 \frac{n}{n_{\text{GJ}}}} \quad (9.24)$$

Here, the number density has been written as a fraction of the Goldreich-Julian number density; the gamma-ray efficiency only depends on this ratio, not on the pulsar properties directly.

As  $n/n_{\text{GJ}}$  approaches unity, so does the gamma-ray efficiency. This is seen in the cases of Geminga and PSR1055-52, where the observations suggest that  $\eta_\gamma \simeq 1$  (Mayer-Hasselwander et al 1994, Fierro et al 1993).

### 9.5.3 The Distribution in Viewing Angle

The emission is not beamed equally into all directions. Figure 9.3 shows the emission (averaged over a period) at 1 MeV as a function of the viewing angle ( $\theta_v = 0$  to  $90^\circ$ ) for two Vela-like pulsars: one with orthogonal fields (solid line) and the other with a dipole inclination of  $11.25^\circ$  (dashed line). The power is scaled to unity at the maximum (again, this is power averaged over a period, which is uniform in  $\phi$ ).

The fraction of the total solid angle into which the power is beamed can be quantified in terms of a power-weighted average:

$$\Omega_p = \int_{\Omega} \frac{P(\Omega)}{P_{\text{max}}} d\Omega \quad (9.25)$$

where  $\Omega$  represents solid angle, not the angular velocity of the pulsar.

Figure 9.4 shows  $\Omega_p$  as a function of frequency for a Geminga-like pulsar with a dipole moment inclined at  $22.5^\circ$  to the rotation axis. A general trend to lower  $\Omega_p$  (and therefore less observable pulsars) is seen for increasing frequency, with a much faster dropoff above the break in the spectrum (near several hundred MeV). Similar results are obtained for pulsars with different model parameters.

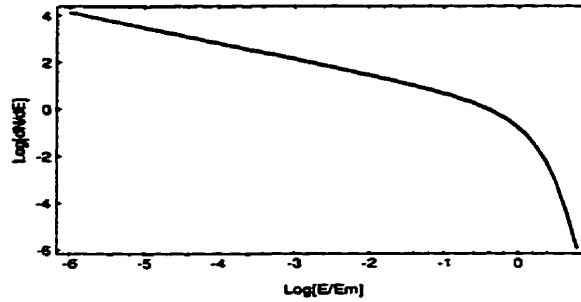


Fig. 9.5: The curvature photon number spectrum for a single particle in instantaneously circular motion. The photon energy is shown in units of the reference energy  $E_m = \hbar\gamma^3 c/\rho$ .

## 9.6 Spectra of Emitted Radiation

Since curvature radiation is the only contribution to the light curves, the frequency distribution of curvature emission by a single particle moving instantaneously in circular motion must be considered (see, for example, Jackson (1975)). The shape of the curve depends on only two parameters - the energy of maximum intensity ( $E_m = 0.14\hbar\gamma^3 c/\rho$ , where  $\gamma$  is the charge's Lorentz factor,  $c$  is the speed of light, and  $\rho$  is the radius of curvature of the particle's path), and the maximum intensity. For energies much less than  $E_m$ , the number distribution in frequency is proportional to  $E^{-2/3}$ ; above  $E_m$ , the curve drops off exponentially, and essentially disappears for  $E > 3E_m$ . This function is plotted in Figure 9.5.

At low frequencies, therefore, each part of the light curve will fall off in photon number like  $E^{-2/3}$ , and the shape of the light curve will remain essentially constant. At higher frequencies, the contributions from particles radiating with different  $E_m$ 's will result in a light curve which is variable with frequency. If several different locations in the magnetosphere make significant contributions to the power, the shape of the spectrum can deviate significantly from the single-particle spectrum.

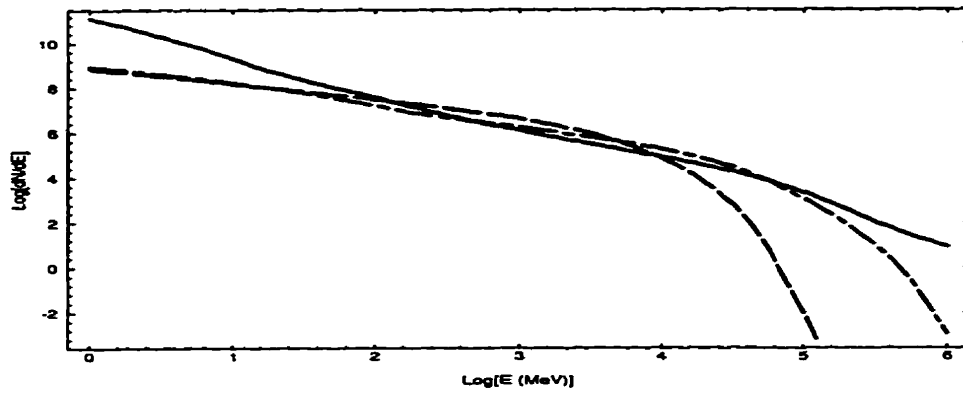


Fig. 9.6: Representative spectra for three model pulsars, all with  $\mu = 10^{31}$  G cm<sup>3</sup>,  $\chi = 90^\circ$ , and seen from a viewing angle of  $84.3^\circ$ . The solid line corresponds to a pulsar with  $\Omega = 150$  rad/s, the dashed-dotted line to one with  $\Omega = 75$  rad/s, and the dashed line to  $\Omega = 25$  rad/s. The faster pulsars show more spectral detail at low frequency.

Figure 9.6 shows several different time-averaged spectra from model pulsars, all with  $\mu = 10^{31} \text{ G cm}^3$ ,  $\chi = 90^\circ$ , and seen from a viewing angle of  $83.4^\circ$ . Spectra for pulsars with three different angular velocities are shown:  $\Omega = 25 \text{ rad/s}$ ,  $75 \text{ rad/s}$ , and  $150 \text{ rad/s}$ . The slow pulsar shows a very hard spectrum with an energy break near several GeV, but relatively featureless otherwise. The  $75 \text{ rad/s}$  pulsar shows a slight softening of the spectrum near a few hundred MeV, and then returning to a hard profile until an energy break near  $100 \text{ GeV}$ . The  $150 \text{ rad/s}$  pulsar has a significantly softer spectrum with no break even through the TeV region. It is interesting to note that the photon flux for all three pulsars is relatively constant in the  $100 \text{ MeV}$  range even though the total power outputs vary considerably.

The different regions of the light curve can have somewhat different spectral properties. Figure 9.7 shows the light curve (c) from Figure 9.1 separated into four components. The components correspond roughly to the peaks at low energy ( $1 \text{ MeV}$ ), shown in (a), and the high-energy ( $10 \text{ GeV}$ ) peaks, which fall at phases of zero and 0.5.

The phase of the gamma-ray peak tends to change with energy when the energies are close to the energy break if it is significantly different from the phase of the radio peak. This occurs because the emission of highest frequency comes from particles moving nearest to the star, where the fields are larger and the paths have a smaller radius of curvature. As the energy increases past the break, the peaks tend to move into phase with the radio peaks, since both are coming from relatively close to the star near the poles. This alignment of gamma-ray phase with radio phase at high frequencies is a provable prediction of the model, given the presumed location of radio emission. It is difficult to see this effect in the present observations, since the phase change only happens at very high frequencies (typically above  $10 \text{ GeV}$ ). However, if the low-energy gamma peaks are not aligned with the radio peaks, it does lead to the “interpulse” regions at low energy having harder spectra and higher energy breaks than the low-energy pulses, as is seen, for example, in the case of the Vela pulsar (Kanbach et al 1994).

Generally the low-energy spectral index of  $-2/3$  is harder than observed in the X-ray

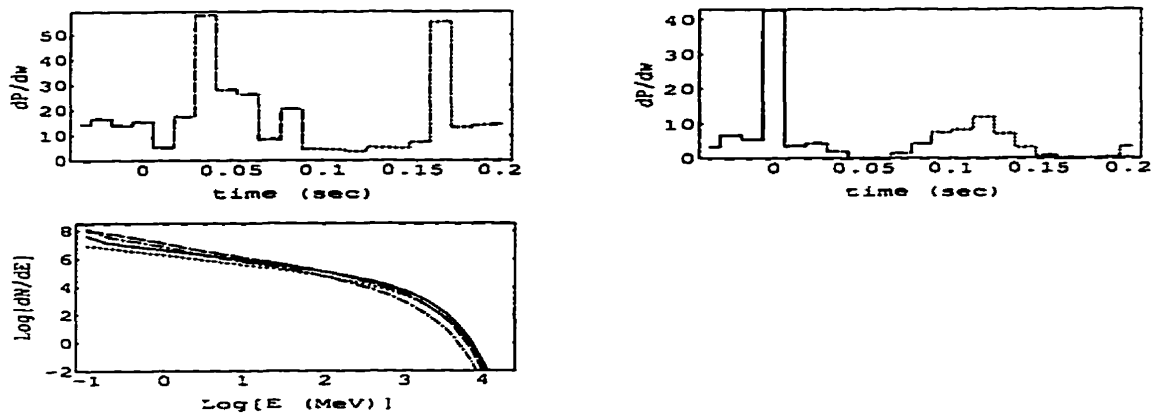


Fig. 9.7: The frequency dependence of the light curve (c) from Figure 4. (a) shows the light curve at 1 MeV, and (b) shows the emission at 10 GeV. (c) shows the spectra for four different components in the light curve. The line dashing of the components in the light curves corresponds to that of the lines in the spectral plot. The axes show the base-10 logarithm of energy in MeV along the horizontal and logarithm of arbitrary differential photon number along the vertical.

region for those pulsars where this has been measured. However, this is precisely the region where the model begins to break down, and radiation from other areas (such as the inner magnetosphere, where unperturbed curvature radiation likely is not the dominant contribution to the spectrum) becomes important.

## 9.7 Aging the Model Pulsar

With the number density at the starting sphere accounted for by equation 9.19, the emission from the model pulsar is fully characterised when the stellar angular velocity  $\Omega$ , the effective magnetic dipole moment  $\mu$ , the dipole inclination angle  $\chi$ , and the viewing angle  $\theta_v$  are given.

An important property to follow is how the properties of a model pulsar changes as it ages and spins down. Assuming that the spin-down is purely due to dipole radiation, the braking index for the pulsar is exactly 3. The age of the pulsar can then be estimated as

$$\tau = -\frac{\Omega}{2\dot{\Omega}} \left(1 - \left(\frac{\Omega}{\Omega_i}\right)^2\right) = \frac{P}{2\dot{P}} \left(1 - \left(\frac{P_i}{P}\right)^2\right) \quad (9.26)$$

where  $\Omega_i = 2\pi/P_i$  is the initial angular velocity of the star. For  $\Omega \ll \Omega_i$ , the characteristic age of the star is just  $\frac{P}{2\dot{P}}$ .

### 9.7.1 The Total Power

The total power emitted into all directions from the model pulsar is (c.f. Paper I, equation 26)

$$P_\gamma = \frac{2\mathcal{E}}{25} ec\mu n$$

Writing the number density as a fraction of the Goldreich-Julian number density, using  $\mathcal{E} = 36$  (orthogonal fields), and substituting equation 9.19 for  $n/n_{\text{GJ}}$ ,

$$P_\gamma = 5.8 \times 10^{34} \text{ergs/s} \left(\frac{\Omega}{100 \text{rad/s}}\right)^{0.5} \left(\frac{\mu}{10^{30} \text{G-cm}^3}\right)^{0.5} \quad (9.27)$$



For large values of  $\tau$  (when  $\Omega \ll \Omega_i$ ), the angular velocity drops off with time as  $\Omega = 1/\sqrt{2k\tau}$ , where

$$k = \frac{2\mu^2 \sin^2 \chi}{3c^3 I} \quad (9.28)$$

Here,  $I$  is the stellar moment of inertia, taken to be  $10^{45}$  g cm<sup>2</sup>. Using this relation, the total power output as a function of age and magnetic dipole moment can be written (setting  $\sin^2 \chi = 1$ )

$$P_\gamma = 1.0 \times 10^{35} \text{ ergs/s} \left( \frac{\tau}{10^5 \text{ yrs}} \right)^{-0.25} \quad (9.29)$$

The total power output is a relatively weak function of time; however, somewhat surprisingly, it does not depend on any other pulsar properties explicitly (as long as the angular velocity of the pulsar is much less than its value at birth, which is not necessarily true for the Crab pulsar or PSR 1951+32).

### 9.7.2 The Evolution of the Spectrum

The spectrum of radiation from the model pulsars can be fairly complex for young pulsars, though it generally shifts to a very hard spectrum for older pulsars like Geminga or PSR1055-52, breaking near a characteristic energy of

$$E_\gamma \simeq \hbar \gamma^3 \frac{c}{\rho} \simeq 8.9 \text{ GeV} \left( \frac{\Omega}{100 \text{ rad/s}} \right)^{1.75} \left( \frac{\mu}{10^{30} \text{ G} - \text{cm}^3} \right)^{0.75} \quad (9.30)$$

This can be re-written as a function of pulsar age:

$$E_\gamma \simeq 5.9 \text{ GeV} \left( \frac{\tau}{10^5 \text{ yrs}} \right)^{-0.875} \left( \frac{\mu}{10^{30} \text{ G} - \text{cm}^3} \right)^{-1} \quad (9.31)$$

The slowest pulsars show a slight softening of the spectrum again down to x-ray energies.

The spectra generated by the model for the very young pulsars (such as the Crab pulsar - see section 9.10.5) are generally harder than the observed spectra, suggesting that some

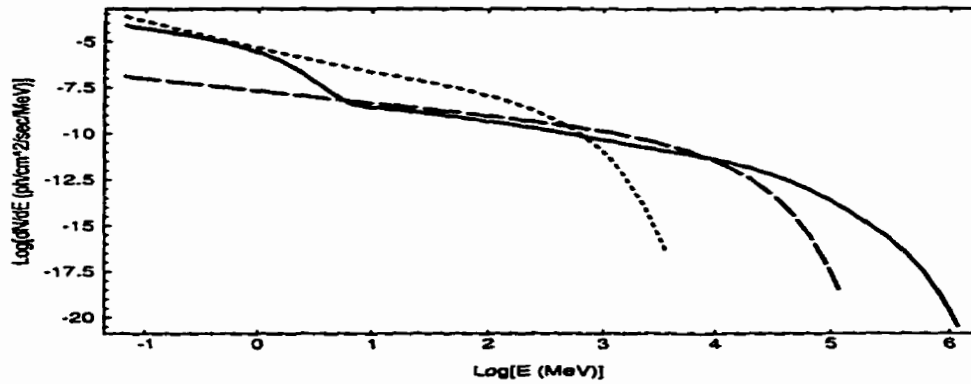


Fig. 9.8: Spectra for a model pulsar with  $\mu = 10^{30} \text{ G cm}^3$  at different times. The solid line shows the spectrum of the pulsar at  $t = 0$ , where the angular velocity is 200 rad/s. The dashed line shows the spectrum at  $t = 10^5$  years, when the pulsar has spun down to  $\Omega = 75$  rad/s. The dotted line corresponds to an age of  $1.6 \times 10^6$  years, when the angular velocity is 10 rad/s (near the extinction point for gamma radiation).

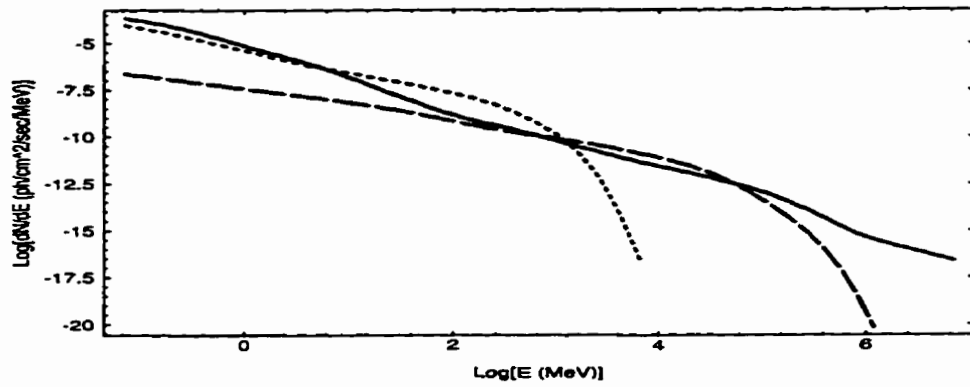


Fig. 9.9: Spectra for a model pulsar with  $\mu = 10^{31} \text{ G cm}^3$  at different times. The solid line shows the spectrum of the pulsar at  $t = 0$ , where the angular velocity is 200 rad/s. The dashed line shows the spectrum at  $t = 10^3$  years, when the pulsar has spun down to  $\Omega = 75$  rad/s. The dotted line corresponds to an age of  $2.5 \times 10^5$  years, when the angular velocity is 5 rad/s (near the extinction point for gamma radiation).

effect which we have not included is at work reprocessing the high energy photons to lower energies. However, the model predictions match the observations very well for the older (slower) pulsars.

Bearing this in mind, Figures 9.8 and 9.9 show the spectra for model pulsars with  $\mu = 10^{30}$  G cm<sup>3</sup> and  $\mu = 10^{31}$  G cm<sup>3</sup> as they age. Both pulsars were started with  $\Omega_i = 200$  rad/s and have orthogonal fields (the spectral shape does not vary much as the dipole inclination changes, as, to give the same period derivative for spin-down, the magnetic dipole moment must increase). The pulsars are set at a distance of 500 pc.

### 9.8 Candidates for Future Searches

With a fit describing the number density of charges at the starting sphere, the population of known pulsars can be examined for pulsars which might be candidates for future high-energy searches.

The catalog of pulsars presented in Taylor et al (1993) was examined for possible candidates. This catalog contains 558 pulsars; the important parameters for this survey were period, period derivative, and distance. The distance for most of the pulsars is only known approximately, as it relies on the model used for the electron column density along different lines of sight, which has significant uncertainties (see Taylor & Cordes 1993).

The pulsars which met the requirement  $n/n_{GJ} < 0.1$  were sorted by bolometric flux received at the Earth. Table 9.2 shows the first thirty pulsars in this category, with the model flux, characteristic photon energy ( $E_\gamma = 8.9$  GeV  $(\Omega/100 \text{ rad/s})^{1.75}(\mu/10^{30} \text{ G cm}^3)^{0.75}$ ), period, period derivative, distance, and notes about the pulsar. Those pulsars already observed in gamma-rays are noted, as well as those with poorly-constrained distances as defined by Taylor et al (1993).

The fluxes have significant uncertainties; this can be roughly estimated from the deviations from the fit to the starting sphere number density (equation 9.19). The actual power output can vary by up to a factor of ten, and the distances are often uncertain by a factor of

Pulsar	Model Flux	Char. Energy	$P$	$\dot{P}$	$D$	Notes
	ergs/cm <sup>2</sup> /sec	GeV	sec	10 <sup>-15</sup> sec/sec	kpc	
Geminga	$5.0 \times 10^{-8}$	1.3	0.237	11.0	0.157	known
Vela	$1.2 \times 10^{-8}$	12	0.0893	125	0.5	known
PSR 0656+14	$2.9 \times 10^{-9}$	1.2	0.385	55.0	0.76	
Crab	$1.3 \times 10^{-9}$	73	0.0333	421	2	known
PSR 1706-44	$7.9 \times 10^{-10}$	8.9	0.102	93.0	1.82	known
PSR 1055-52	$4.7 \times 10^{-10}$	1.3	0.197	5.83	1.53	known
PSR 0740-28	$4.2 \times 10^{-10}$	2.4	0.167	17.8	1.9	poor distance
PSR 2334+61	$3.5 \times 10^{-10}$	1.4	0.495	192	2.46	
PSR 0114+58	$2.9 \times 10^{-10}$	3.2	0.101	5.84	2.12	
PSR 1046-58	$2.8 \times 10^{-10}$	6.9	0.124	95.9	2.98	
PSR 1449-64	$2.7 \times 10^{-10}$	1.1	0.179	2.75	1.84	
PSR 1951+32	$2.7 \times 10^{-10}$	12	0.0395	5.85	2.5	known
PSR 0355+54	$2.6 \times 10^{-10}$	1.6	0.156	4.39	2.07	
PSR 1742-30	$2.5 \times 10^{-10}$	0.68	0.367	10.7	2.09	
PSR 1509-58	$2.5 \times 10^{-10}$	15	0.150	1540	4.4	known
PSR 1737-30	$2.3 \times 10^{-10}$	1.4	0.607	466	3.28	
PSR 1853+01	$2.3 \times 10^{-10}$	3.2	0.267	208	3.3	
PSR 1221-63	$2.0 \times 10^{-10}$	1.1	0.216	4.95	2.29	
PSR 1719-37	$2.0 \times 10^{-10}$	1.3	0.236	10.8	2.52	Geminga-like
PSR 1800-21	$1.7 \times 10^{-10}$	7.1	0.134	134	3.94	

Tab. 9.2: The twenty brightest (non-millisecond) pulsars as predicted by the model in terms of average bolometric flux. The characteristic energy of the emitted photons is given in GeV, along with the period, period derivative, and distance for each pulsar. The brightest pulsars are the known pulsars. The total flux is uncertain by up to a factor of ten due to uncertainties in the distance and beaming effects. The model prediction for Geminga is a factor of ten too high; it would actually place second after Vela were its real flux listed.

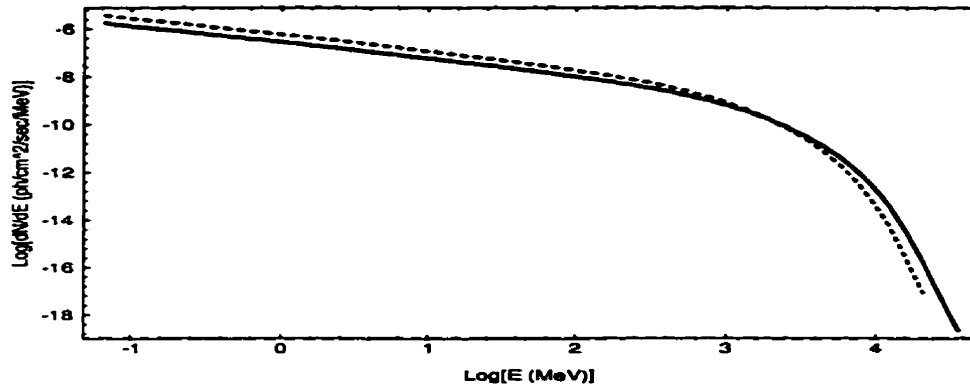


Fig. 9.10: Model spectrum for PSR 0656+14 (solid), with the model spectrum for Geminga (scaled to fit the observations) shown as reference (dotted).

two. Due to these uncertainties, all of the pulsars in Table 1 should be considered possible candidates for future sources.

Pulsar PSR 1719-37 is of particular interest, as it is almost identical to Geminga in angular velocity and magnetic dipole moment. Observing gamma radiation from this pulsar might help elucidate the lack of observed radio emission from Geminga. Its predicted flux is a factor of 250 less than the predicted flux of Geminga, though only smaller by a factor of 25 than Geminga's observed flux. If Geminga's anomalously low flux is due to beaming, the predicted flux for PSR 1719-37 might be measurable.

A candidate often mentioned in these surveys (REFS) is PSR 0656+14, which has been recently tentatively identified as a gamma-ray source (Ramanamurthy 1996). The emission from this source is predicted to be quite large from our model as well; it scores third in Table 1. The predicted spectrum is shown in Figure 9.10, with Geminga's spectrum shown for reference (dotted line).

### 9.8.1 *The INTEGRAL Telescope*

Since our model predicts very flat spectra at low energies, most of the power is emitted at higher frequencies than the 10 keV to 10 MeV range of the proposed INTEGRAL telescope. The spectra of the slowest pulsars can be significantly steeper than the  $E^{-2/3}$  required by the tail end of the curvature emission spectrum in the INTEGRAL energy range; however, these are generally the dimmest of the population.

### 9.8.2 *The GLAST Telescope*

The GLAST telescope is a high-energy gamma-ray telescope sensitive to photon energies between 10 MeV and 300 GeV, probing to higher energies than the CGRO instruments. These measurements will be crucial in determining why our model seems to fail with the fastest (and youngest) pulsars, as we predict significant very high-energy fluxes for some. If photons at these energies are observed, then the mechanism for reprocessing them to lower energies may become somewhat clearer.

### 9.8.3 *The CELESTE Telescope*

The proposed CELESTE telescope (Dumora *et al*) is a Čerenkov air-shower detector which is sensitive to photons with energies greater than approximately 30 GeV. As with the GLAST telescope, high-energy measurements of gamma-ray pulsars will be important in elucidating the mechanism of reprocessing high-energy photons to lower energies in our young model pulsars.

## 9.9 *Millisecond Pulsars*

The millisecond pulsars have always been a good testing ground for pulsar theories due to their relatively tiny magnetic fields ( $10^8$ – $10^9$  G at the stellar surface) and their short periods (tens of msec down to 1.5 msec), which allow observations of a rather separate region of parameter space.

All gamma-ray pulsar models predict luminosities from these objects too low to be observed (Sturmer & Durmer 1994) or non-existent (Chiang & Romani 1994). Our model predicts a relatively high luminosity; from equation 9.27,

$$P_\gamma = 1.1 \times 10^{34} \text{ergs/s} \left( \frac{\Omega}{1000 \text{rad/s}} \right)^{0.5} \left( \frac{\mu}{10^{27} \text{G} - \text{cm}^3} \right)^{0.5} \quad (9.32)$$

This power is high enough that nearby millisecond pulsars may be observable. In particular, PSR J0437-4715, PSR 1534+12 and PSR 1257+12, if included in Table 1, would rank 3, 6, and 8, and are therefore good candidates for observation. PSR J0437-4715 has already been observed as a pulsed X-ray source (Becker & Trumper 1993), so seems an especially good candidate.

In our model, PSR J0437-4715 would have an extremely high gamma-ray efficiency, approximately 0.6, an average bolometric flux at the Earth of  $5.9 \times 10^{-9}$  ergs/s/cm<sup>2</sup>, and a typical photon energy of 1.5 GeV.

Recent observations (Verbunt *et al* 1996) have suggested that the EGRET source 2EG J0220+4228 represents gamma-ray emission from the positionally coincident millisecond pulsar PSR J0218+4232, though the significance of pulsation in the data is only  $3.5 \sigma$ . If the association is valid, the flux from the pulsar is roughly  $5 \times 10^{-11}$  ergs/cm<sup>2</sup>/s, or about 10% of its spin-down luminosity (assuming a distance of 5.7 kpc, which is a lower limit).

For this pulsar, our model predicts a flux of approximately  $3 \times 10^{-12}$  ergs/cm<sup>2</sup>/s, significantly less than the observed luminosity, and much less than the predicted luminosity of other millisecond pulsars. This may suggest that the model used to generate the emitted gamma-ray power (based on the model for the number density at the starting sphere) needs modification.

### 9.9.1 *Gamma-ray Luminosity of Globular Clusters*

It has been suggested (Bhatia *et al* 1995) that the combined luminosity from millisecond pulsars in a globular cluster may be large enough to be observed. They use a model developed



by Scharlemann *et al* (1978) which is similar in many respects to the Deutsch field pulsar in its basic physics, though it assumes number densities of emitting electrons and positrons to be always on order of the Goldreich-Julian number density (a hypothesis that gives a poor fit to the data from the seven known gamma-ray pulsars).

Their estimate of the cluster luminosity, based on a rough distribution of millisecond pulsars in period ( $dN/dP \propto P^{-1.4}$ ) and a relation between the pulsar period and its magnetic dipole moment ( $\mu \propto P^{7/6}$ ), is

$$P_{GC} = 3.8 \times 10^{36} \text{ergs/s} \left( \frac{n}{500} \right) \quad (9.33)$$

where  $n$  is the number of millisecond pulsars in a globular cluster.

Using their distribution of millisecond pulsar periods and relationship between period and magnetic field, our estimate is

$$P_{GC} = 1.1 \times 10^{37} \text{ergs/s} \left( \frac{n}{500} \right) \quad (9.34)$$

which is of the same order, despite the different relationship of gamma-ray power to  $\Omega$  and  $\mu$ . Identification of gamma-rays from GC millisecond pulsars would strongly argue against the outer gap models and others which predict negligible emission from millisecond pulsars.

The spectral distribution of the emission from a GC is quite different from that of an individual pulsar due to the distribution of spin periods. The emission from an individual pulsar is fairly strongly peaked near the characteristic energy  $E_\gamma$ ; if we assume that the distribution of power from an individual pulsar is a delta function in energy, then the spectral distribution of flux from the globular cluster is given by

$$\frac{dN}{dE} = 3.5 \times 10^{-10} \text{photons/s/MeV/cm}^2 \left( \frac{n}{500} \right) \left( \frac{D}{\text{kpc}} \right)^{-2} E^{-1.45} \quad (9.35)$$

This is valid between a few hundred MeV and 10 GeV, assuming a minimum period of 1.6 ms and a maximum period of near 50 ms for the distribution in period; below a few

hundred MeV, this will fall off again like  $E^{-2/3}$ , and above 10 GeV the spectrum will break abruptly.

For 47 Tucanae, for example, which is approximately 4.6 kpc from Earth, this translates to an integrated photon flux above 100 MeV of  $1.8 \times 10^{-12}$  ph/s/cm<sup>2</sup>, which is too low to be observed by EGRET or the proposed GLAST telescope.

### 9.10 *The Seven Known Gamma-Ray Pulsars*

As of this writing, seven pulsars are known to emit in the gamma-ray region of the spectrum: the Geminga, Vela, and Crab pulsars, as well as PSR1055-52, PSR1706-44, PSR1509-58, and PSR1951+32. This relatively small statistical sample provides the data against which all gamma-ray pulsar models must be compared.

The parameters which can be adjusted to fit the spectrum and shape of the light curve are the effective magnetic dipole moment  $\mu$ , the inclination angle  $\chi$ , and the viewing angle  $\theta_v$ . The spin rate is not included as a free parameter, as observations fix this very closely. The allowed variation in  $\mu$  is relatively small, though uncertainties in the stellar moment of inertia allow approximately variations of up to a factor of three in its value. The value of  $\chi$  has been estimated for some pulsars (see section 3.2), but this is a model-dependent analysis and is therefore somewhat suspect. However, these values are used whenever available (for PSR1055-52 and the Crab and Vela pulsars).

Variation of the viewing angle do not change the spectra much, nor does changing  $\chi$  (as long as  $\mu$  scales as  $1/\sin^2 \chi$  to retain consistency with the spindown data). The values of  $\theta_v$  and  $\chi$  mainly affect the shape of the light curve: it is in general possible to roughly match the observed light curves by appropriate variation of these two parameters (see figure 9.1). Therefore, only the fits to the spectra of the known pulsars will be discussed, as these are much more sensitive to the known values of  $\Omega$  and  $\mu$ .

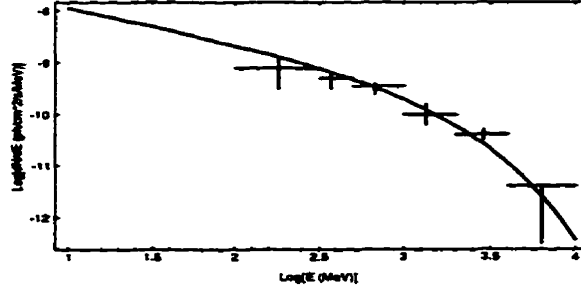


Fig. 9.11: The time-averaged model spectrum of PSR1055-52 with the EGRET observations. The model spectrum fits the data well. The magnetic dipole moment required for the best fit was  $1.8 \times 10^{30} \text{ G cm}^3$ , somewhat higher than the  $1.1 \times 10^{30} \text{ G cm}^3$  predicted by the pulsar spindown rate.

#### 9.10.1 PSR1055-52

PSR 1055-52 is the oldest of the known gamma-ray pulsars, with a characteristic age of  $5.4 \times 10^5$  years. Its spectrum is also the softest of the known pulsars. A fit to the EGRET data gives good agreement for  $\mu = 1.8 \times 10^{30} \text{ G cm}^3$  (somewhat higher than the  $1.1 \times 10^{30} \text{ G cm}^3$  predicted from the spindown data). Figure 9.11 shows the model spectrum with the EGRET data.

#### 9.10.2 The Geminga Pulsar

The Geminga pulsar is one of the closest to turnoff, with  $n/n_{\text{GJ}} = 2.1 \times 10^{-3}$ . A fit to EGRET data gives reasonable agreement when  $\mu = 10^{30} \text{ G cm}^3$ . Figure 9.12 shows the time-averaged spectrum for Geminga and a comparison to the observed data.

The characteristic age of the Geminga pulsar is  $\tau = \frac{P}{2\dot{P}} = 3.4 \times 10^5$  years.

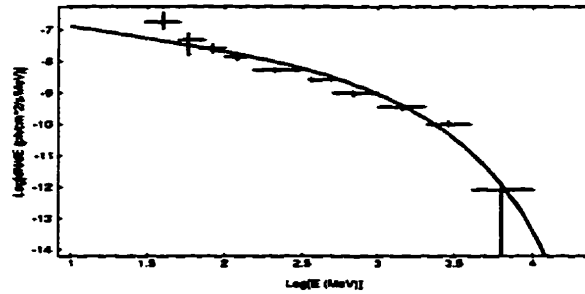


Fig. 9.12: The time-averaged model spectrum of Geminga with the EGRET observations. The model spectrum fits the data well. The magnetic dipole moment required for the best fit was  $1.1 \times 10^{30} \text{ G cm}^3$ , somewhat lower than the  $1.6 \times 10^{30} \text{ G cm}^3$  predicted by the pulsar spindown rate.

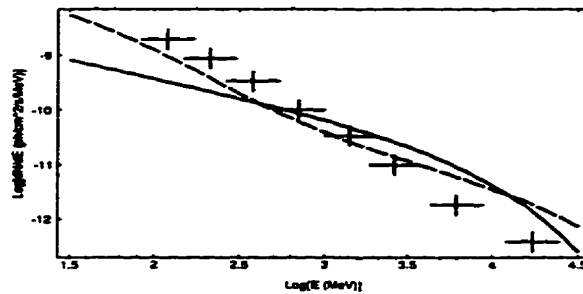


Fig. 9.13: The time-averaged model spectrum of PSR 1951+32 with EGRET observations. The solid line shows the model spectrum for  $\mu = 0.49 \times 10^{30} \text{ G cm}^3$ , the value derived from spindown data; this spectrum is significantly harder than the observations. The dashed line represents the spectrum of a model pulsar with  $\mu = 5 \times 10^{30} \text{ G cm}^3$ , a value too large to be acceptable, but even this spectrum does not fit the observations well.

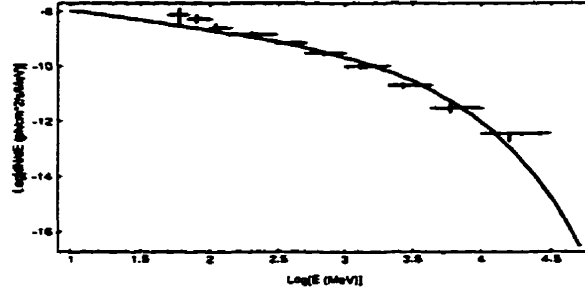


Fig. 9.14: The time-averaged model spectrum of PSR 1706-44 with the EGRET observations. The model spectrum fits the data well except for at the lowest photon energies. However, the magnetic dipole moment required for the fit was  $0.5 \times 10^{30} \text{ G cm}^3$ , significantly lower than the  $3.1 \times 10^{30} \text{ G cm}^3$  predicted by the pulsar spindown rate. This suggests that PSR 1706-44 may be an especially low-mass neutron star.

### 9.10.3 PSR1951+32

This pulsar is moderately young, with an age of  $1.1 \times 10^5$  years. Again, the model has difficulty matching the observed spectrum. Figure 9.13 shows the spectrum for  $\mu = 0.49 \times 10^{30} \text{ G cm}^3$  (derived from spindown data - solid line) and that for  $\mu = 5 \times 10^{30} \text{ G cm}^3$  (dashed), as well as the EGRET data. Neither of the spectra match the observations well.

### 9.10.4 PSR1706-44

PSR 1706-44 is a relatively young pulsar, with  $\tau = 1.7 \times 10^4$  years. A good fit is found with  $\mu = 0.5 \times 10^{30} \text{ G cm}^3$ ; this is significantly lower than that predicted by the spindown rate (this predicts  $\mu = 3.1 \times 10^{30} \text{ G cm}^3$ ), suggesting that this pulsar might be an object with an especially low moment of inertia. Figure 9.14 shows the time-averaged spectrum for this object.

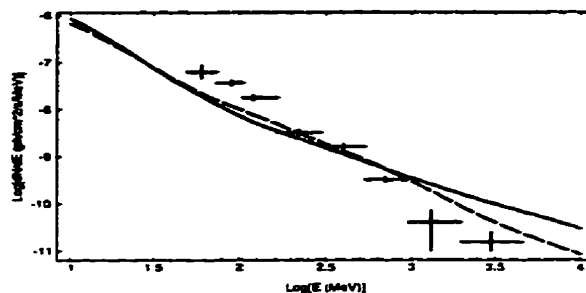


Fig. 9.15: The time-averaged model spectrum of the Crab pulsar with EGRET observations. The solid line shows the model spectrum for  $\mu = 3.8 \times 10^{30} \text{ G cm}^3$ , the value derived from spindown data; this spectrum is significantly harder than the observations. The dashed line represents the spectrum of a model pulsar with  $\mu = 50 \times 10^{30} \text{ G cm}^3$ , an absurdly large value, but even this spectrum is too hard.

#### 9.10.5 The Crab Pulsar

The Crab pulsar, with an age of only  $10^3$  years, is the youngest of the known gamma-ray pulsars, and the first to be detected at frequencies other than radio.

No variation of the parameters available could provide a fit to the Crab's spectrum. The model spectra are always much harder than the observations, even for absurdly high choices of  $\mu$ . Figure 9.15 shows the EGRET observations of the pulsar as well as two model spectra: the solid line shows the model spectrum for  $\mu = 3.8 \times 10^{30} \text{ G cm}^3$  (from the spindown rate), and the dashed line shows the spectrum for  $\mu = 50 \times 10^{30} \text{ G cm}^3$ . Both spectra are similar in the EGRET range.

The fact that the spectra was too hard suggests that, for the youngest pulsars, there may be a process (unaccounted for in our model) which reprocesses high-energy photons to lower energies.

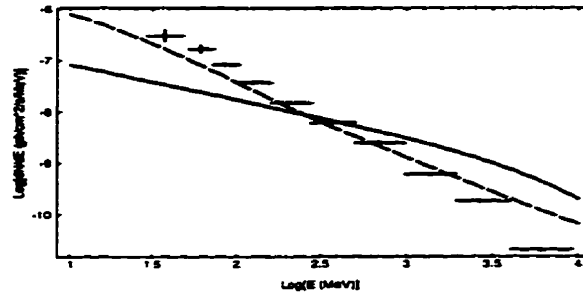


Fig. 9.16: The time-averaged model spectrum of the Vela pulsar with EGRET observations. The solid line shows the model spectrum for  $\mu = 3.4 \times 10^{30} \text{ G cm}^3$ , the value derived from spindown data; this spectrum is much harder than the observations. The dashed line represents the spectrum of a model pulsar with  $\mu = 100 \times 10^{30} \text{ G cm}^3$ , an absurdly large value, but even this spectrum is too hard.

#### 9.10.6 The Vela Pulsar

The Vela pulsar is also a young pulsar, with  $\tau = 1.1 \times 10^4$  years.

No variation of the parameters allowed a fit to the observed spectrum. Figure 9.16 shows the EGRET data as well as the model spectrum for  $\mu = 3.4 \times 10^{30} \text{ G cm}^3$  (solid line) and the model spectrum for  $\mu = 100 \times 10^{30} \text{ G cm}^3$ . The lower value of  $\mu$  is the one derived from the spindown data; its spectrum is much too hard. The second value of  $\mu$  is much too large, but even this spectrum is too hard and puts out too much energy at high photon energies.

#### 9.10.7 PSR1509-58

This is the second-youngest of the known pulsars, with  $\tau = 1.5 \times 10^3$  years. This is the only one of the gamma-ray pulsars not observed by EGRET; it has only been seen at frequencies below approximately 1 MeV.

The model predictions give photon energies much higher than those observed;  $E_\gamma = 15 \text{ GeV}$  is predicted. This should be easily observable in the EGRET range. The fact that it

is not suggests rather strongly that some sort of photon reprocessing is occurring in these youngest pulsars.



## 10. FUTURE WORK

As it stands, the Deutsch field gamma-ray pulsar model presented here is not entirely complete. While it can reproduce the spectra of the older pulsars quite accurately and generate light curves similar to those observed, the total power output for a model pulsar is difficult to determine. The solution of this problem involves charge creation in the outer magnetosphere.

### 10.1 *The Source for the Charge*

The simple estimate made in section 9.5.1 for the charge density generated through a process where the charges that emit gamma-rays are self-consistently created by the photons they emit suffers from many approximations which make it rather suspect.

A more detailed analysis of this problem would involve a global solution across the outer magnetosphere. The charge creation process is exclusively photon-photon pair creation (as the magnetic fields are too small to allow  $\gamma$ - $B$  pair creation), although in the more general problem, photons of quite different energies can be involved. If there is a relatively soft photon flux from the inner magnetosphere, the high-energy gamma rays can pair produce quite efficiently, as the cross-section is largest when the product of the two photon energies is slightly larger than the square of the rest mass energy of an electron.

To examine the possible construction of such a physical scenario, consider the number density of electrons (or positrons),  $n_e$ , and that of photons,  $n_\gamma$ , in the outer magnetosphere. Define  $f$  and  $g$  through

$$n_e = f \frac{\sqrt{1 + 3 \cos^2 \theta}}{r^3} \quad n_\gamma = \frac{g}{r^2} \quad (10.1)$$

so defined such that, with no charge creation, photon creation, or photon annihilation ( $f =$

$g = \text{constant}$ ), the charges will move parallel to the magnetic field lines with constant speed with a density proportional to the magnetic field and the photons will move radially outward with a density falling off like  $1/r^2$ . This can be seen from examining the continuity equations for electrons and photons: if we then assume a steady-state solution, that the charges move with speed  $c$ , and velocity always parallel to  $\vec{B}$ , and that photons move outward, then the continuity equations reduce to

$$2\frac{\partial f}{\partial r} \cos \theta + \frac{\partial f \sin \theta}{\partial \theta} \frac{1}{r} = \frac{\dot{n}_e}{c} r^3 \quad (10.2)$$

$$\frac{\partial g}{\partial r} = \frac{\dot{n}_\gamma}{c} r^2 \quad (10.3)$$

The charge and photon creation rates are given by

$$\dot{n}_\gamma = An_e - B\frac{n_\gamma}{r^2} - Cn_\gamma^2 \quad \dot{n}_e = B\frac{n_\gamma}{r^2} + Cn_\gamma^2 \quad (10.4)$$

The term proportional to  $A$  relates to photon creation by the charges (through, for example, curvature emission); if  $A$  is constant, then it is assumed that the rate of photon emission per charge is constant throughout the magnetosphere. For this to be the case for curvature emission, the charge energy and path radius of curvature would have to conspire such that  $\gamma/\rho$  is a constant.

The term including  $B$  gives the rate of pair creation through scattering of the photons off a low-energy bath of photons with a density which falls off like  $1/r^2$  (presumably created in the inner magnetosphere). If the energy of the gamma-ray photons is constant throughout the magnetosphere, then so is  $B$ .

The third contribution to  $\dot{n}_\gamma$  corresponds to pair creation by scattering of two gamma-ray photons, and is therefore proportional to  $n_\gamma^2$ . If the gamma-ray photon energy is the same everywhere,  $C$  will be constant.

The solution to this pair of equations is non-trivial, especially considering the need to include self-consistent boundary conditions at the inner magnetosphere. As well, in this

simple example the electrons only travel parallel to the magnetic field lines; a more complete solution would include those travelling anti-parallel as well and include possible variations of  $A$ ,  $B$ , and  $C$  throughout the magnetosphere.

Assuming the photons move radially outward is also somewhat suspect; this is valid far out in the magnetosphere, as most pair and photon creation occurs closer in. However, the most interesting physics occurs near the inner magnetosphere, and it may be more appropriate to assume that the photons are always travelling parallel to the magnetic field as well (a good approximation if the mean free path for pair or photon creation is small).

This analysis ignores a possible distribution in energy for charges or photons; including a spread complicates the analysis enormously, as the scattering rates involve integrations over these distributions. If the energies of both are relatively tightly constrained, or a simple model of the distribution can be applied everywhere to estimate the effect of these spreads, this somewhat approximate model should suffice.

The level of soft photon flux is difficult to determine in many cases, as observations in the interesting regime (low-energy x-rays) are scarce; the interstellar medium absorbs photons of this frequency through the photoelectric effect.

## *10.2 Synchrotron Radiation*

Created charges will radiate away perpendicular momentum through synchrotron radiation as soon as they are created; if charges are continuously created throughout the outer magnetosphere, this may be an important contribution to the overall emission. As well, the synchrotron emission is normally at a lower energy than curvature emission in the outer magnetosphere, and may help abate the deficit of low-energy photons in the models of young gamma-ray pulsars.

### *10.3 Refinements of the Numerical Modelling*

Currently the charges are started on a grid uniformly spaced around the starting sphere. A better choice would be to use a grid with varying spacing, where the grid is tighter near outgoing paths and ingoing paths which penetrate a significant distance into the outer magnetosphere, and wider in regions where most of the paths are both short and ingoing or stopped, to properly capture the paths which contribute most of the radiation to the light curves. Which paths are going to be important is not always obvious in advance of the path integration, and therefore the grid spacing algorithm would have to be somewhat iterative.

Also, given a model for charge creation, starting charges on a sphere of fixed radius might be too simple an approximation, especially if there is significant pair creation throughout the outer magnetosphere. The algorithm for starting path integrations would, in a more complete model, take this distribution into account as well.

This model also ignores the radiative contributions of charges which travel a significant distance the light cylinder on null surfaces. They are ejected into a relatively weak field, large radius of curvature region near the light cylinder, and therefore are not expected to radiate significantly; however, they might make up the low-energy deficit of photons in the observed spectra for the young pulsars.

### *10.4 Iterating the Solution to a Self-Consistent Magnetosphere*

The model thus far assumes that the charge and current densities in the outer magnetosphere are small enough to ensure the accuracy of vacuum fields. If the densities are large enough, this no longer holds. However, it may be possible to iterate to a global solution by initially assuming vacuum, determining the charge and current densities, and finding how they change the electromagnetic fields. This new solution for the fields could then be used to generate new charge and current densities, and the process repeated until a self-consistent solution is found.

The convergence of this sort of iterative solution of differential equations is by no means assured, however, so much work needs to be done to even examine the possibility of using this technique. It is also quite expensive computationally, though perhaps not as intensive as solving the set of partial differential equations using traditional techniques.

### *10.5 Applying the DFB Approximation to Global Modelling*

The pulsar problem as discussed in section 1.2 can be simplified by using the DFB approximation to describe the motion and energetics of charged particles in the pulsar magnetosphere. The general problem is still complex, but being able to write the charge velocity in terms of the fields at a particular point in space simplifies the analysis significantly.

Approximations similar to this have been used in the past, but the charge motion was generally assumed to flow with a component along  $\vec{B}$  and one equal to the corotation velocity. This is only true when the charge density is equal to the Goldreich-Julian charge density everywhere; in a less idealised magnetosphere, this assumption is no longer valid. However, due to the complex relationship between charge velocity and fields in the DFB approximation, it is expected that only a numerical treatment could be applied.

The DFB approximation works best when applied to faster pulsars, as the magnetic fields at the light cylinder of slower pulsars is not large enough to ensure that perpendicular momentum is radiated away at a high enough rate (condition 8.15). Therefore, it may have limited applicability in simulating charge motion near the light cylinder in older radio pulsars. However, since it is expected that the radio emission occurs near the star, where the fields are still very large and the DFB approximation is valid, it may be useful even for these slower objects.

### *10.6 The Inner Magnetosphere*

Understanding the physics of the inner magnetosphere may be important to the gamma-ray emission of the pulsar, as low-energy fluxes from this region may play a part in pair creation.

The full problem is complex one involving plasma physics, but a method which may have some success is similar to that used in the polar cap models of Daugherty & Harding (1996).

Monte Carlo-simulating charges as they move through the inner magnetosphere and pair create can give a better idea of the shape of the inner magnetosphere and the magnitude of fluxes of different photon energies. This will give very little information about the radio emission mechanism (almost certainly a coherent plasma process), but may give accurate results in photons energies at the optical level and higher. These are the photons which will be important for pair-creation and inverse Compton scattering processes. Understanding how to properly include plasma effects in the charge motion is non-trivial, however.

## 11. CONCLUSIONS

Two scenarios involving gamma-radiation from neutron stars have been examined in this thesis: first, in terms of sources for GRBs where neutron stars born in the disk interact with comets born in globular clusters, and second, as a model for gamma-ray emission from pulsars.

### *11.1 Distribution of GRBs in Halo Neutron Star-Comet Interactions*

This research involved simulating GRB distributions given a model framework of GRB creation: they are made in the interaction between a neutron star in a large Galactic halo and a comet, ejected from a globular cluster or a stellar system in the Galactic disk. The main criteria the model was tested against were the observed distribution on the sky, which, within statistical limits, is isotropic, and the distribution in burst flux, which looks like a homogeneous distribution of standard candles for the bright bursts, but shows a deficit in dim bursts, suggesting an edge to the distribution radially. Therefore, the observed GRB distribution is a roughly homogeneous sphere, with centre near the Sun, which is truncated at some maximum radius.

$4 \times 10^6$  neutron stars were born in the disk, where their spatial birth distribution was taken to be the same as the pulsar spatial distribution, and their velocity distribution was allowed to vary. Several birth velocity distributions were tested: one equal to the observed pulsar birth velocity distribution, and various high-speed distributions. There is evidence to suggest that some pulsars can be born with very high velocities indeed (one the order of 1000 km/s or larger), which would be completely unbound from the Galaxy's potential well. The neutron star motion was simulated for 5 billion simulation years.

Comets were created in two locations. The first was in stellar systems in globular clusters, where they are first ejected from the stellar system with low energy, and then scatter to high energies and are ejected into the Galactic halo.  $10^7$  of such comets were evolved for the 5 billion-year simulation period. The second location was in stellar systems in the disk, from which they are ejected with low energy. These comets were assumed to have a density distribution which followed the mass distribution of the disk component of the Galaxy.

The conclusion of this work was that models of GRBs as interactions between halo neutron stars and interstellar comets are rather untenable due to their distributions in space. The two basic criteria any GRB model must meet are the isotropic distribution on the sky and truncated uniform distribution in flux observed by BATSE. None of the models we tested could match the distribution on the sky; however, matching the distribution in flux did not prove difficult, as in some models the nearby bursts came from distances inside the typical width scale of the Galactic disk (and therefore looked uniform in flux). Fixing the maximum radius out to which the hypothetical telescope can observe by forcing the distribution in flux to match the observed  $\langle V/V_{\max} \rangle$  statistic (which is a measure of the deviation from uniformity in the flux distribution) generally makes the anisotropies spatially more prevalent.

In addition, there is a severe constraint on the rate of comet production in globular cluster stellar systems. These stellar system must be more than  $10^6$  times more efficient at making comets than disk comets (the rate for disk comet generation is taken to be equal to the Solar System's rate), otherwise the rate of GRB production drops below the observed one burst/day, and the anisotropy of the bursts toward the Galactic disk becomes extremely pronounced. This is due to the fact that there are many more stellar systems in the disk than in globular clusters. The requirement of this very high efficiency for comet production in globular cluster stellar systems is another compelling reason to dismiss this class of GRB model.

There are still several parameters which may be added to the model which might lessen the discrepancy with the data, such as introducing a "turn-on" time, before which neutron



stars may not burst, and beaming of the gamma-rays along the velocity vectors of the stars. However, the distribution of bursts derived from neutron stars with a birth velocity following the observed birth velocity distribution of pulsars was very strongly peaked toward the Galactic centre due to the bound pulsars which were born with velocities on the low end of the distribution. It is doubtful that any additional effects could completely eliminate this dominant anisotropy.

This work has been published as Higgins & Henriksen (1995) in a somewhat reduced format.

### *11.2 The Deutsch Field Gamma-Ray Pulsar Model*

A new model of high-energy pulsar emission has been presented, with the simplifying assumption that the charge densities and current densities are small enough that the electromagnetic fields can be represented by the Deutsch fields in the outer magnetosphere.

The assumption that the magnetosphere can remain evacuated is justified by recognising that charges created near the star either follow paths bound to small radii or are expelled from the magnetosphere on null surfaces, and cannot short out the fields farther out. We create an approximate self-consistent global solution to the electromagnetic fields and charge motions by extending the “stellar” radius (inside which the fields are frozen-in) to 0.1 of the light cylinder radius; charge created in the inner magnetosphere can flow out along null surfaces where the electric field is perpendicular to the magnetic field. This defines our “inner” and “outer” magnetosphere: the inner magnetosphere is the corotating region inside  $0.1R_{lc}$ . The outer magnetosphere is the location of particle acceleration and high-energy emission, and the inner, charge-filled, magnetosphere is the site of the radio emission (which was not simulated in our model).

An important approximation has been developed to chart particle motion in fields where the timescale required to radiate away the charge’s momentum perpendicular to the magnetic field is much smaller than other timescales in the problem (primarily the timescale to adjust

to any changes in the direction or magnitude of the electric and magnetic fields), called the drift frame bead-on-a-wire (DFB) approximation. This reduces the problem of particle motion to a simple first order, ordinary set of differential equations, reducing computation time enormously. This approximation could prove useful for developing global, self-consistent models of the pulsar magnetosphere, as it gives a relatively simple description of charge paths in terms of the electric and magnetic fields at every point in space where  $\vec{E}$  and  $\vec{B}$  are not perpendicular.

The case of orthogonal electric and magnetic fields was considered by developing the theory of “null surfaces” (surfaces where  $\vec{E} \cdot \vec{B} = 0$ ). Charges are often attracted to these surfaces. When a high-energy charge which is radiation-reaction limited as it travels (when the electric power input is roughly balanced by the radiative power output) hits one of these surfaces, it loses most of its energy very quickly, as there is no longer any energy input. It then travels along the null surface, following its drift velocity and being affected by “centrifugal force” if the null surface is rotating.

Two kinds of null surface exist: wired null surfaces, which contain the magnetic field lines everywhere, and pierced null surfaces, which do not. Charge motion on these different kinds of surface can be quite different. In general, wired null surfaces attract both signs of charge, whereas pierced null surfaces only attract one sign of charge at any particular location.

The Deutsch fields have several null surfaces; the most important is the surface in the limit of  $a \ll r \ll R_{lc}$ , where  $a$  is the stellar radius and  $R_{lc}$  is the light cylinder radius. This null surface is a plane inclined from the rotation axis with the same inclination angle as the effective magnetic dipole moment  $\mu$ , and is a wired null surface. Charges of both signs are attracted to this surface and flow out with equal velocities, making a low-energy neutral plasma which can escape the magnetosphere without significantly radiating or affecting the vacuum fields in the outer magnetosphere. This surface breaks up near the light cylinder where the field structure becomes more complex, but the charges do not emit significant amounts of radiation as they leave the magnetosphere due to the larger radii of curvature of

the charge paths and the weaker electric and magnetic fields.

Several constraints on the applicability of the vacuum approximation can be made, the most important of which is that the number density required to produce the observed power output must be much less than the Goldreich-Julian charge density. All observed gamma-ray pulsars satisfy this constraint, as well as that which maintains the dominance of curvature radiation to the high-energy spectrum in the model framework and that which maintains the applicability of the DFB approximation. As the pulsar ages, the number density in the outer magnetosphere approaches the Goldreich-Julian value; when it reaches this level, the electric fields parallel to the magnetic field lines are shorted out, and the pulsar stops radiating gamma-rays. This naturally explains the fact that only the youngest and fastest pulsars are observed to emit gamma-rays.

The light curves generated from the model match the general properties of the observed light curves quite well. When the magnetic dipole moment is orthogonal to the rotation axis, the light curves are mainly double-peaked; the second half of the light curve is identical to the first. Other inclinations can give single peaks, non-symmetric double peaks, and triple peaks, as well as practically unpulsed emission in some cases. They often show thin, tall peaks which are not observed in the data, but these are an artifact of the numerical procedure. A more complete simulation would show these peaks smeared out in phase and emitting direction.

The biggest weakness of the model is its present inability to predict the actual power output of the pulsars in gamma-rays: it does not assume any value for the number density at the starting sphere, only that it be much less than the Goldreich-Julian number density so that the electric fields are not shorted out. It also says nothing about any radiation produced in the inner, bound magnetosphere, where particle energies will be somewhat lower than those in the outer, evacuated magnetosphere. This might provide significant emission at lower energies. An outline of a possible charge creation model was suggested and somewhat elaborated in chapter 10, but is still rather unsatisfying due to the rough nature

of the approximations.

Our model compares quite favourably with the other popular models for pulsar gamma-ray emission in certain limits. The spectra predicted by our model match the observations in some cases better than those generated by the outer gap model of Chiang & Romani (1994), and as well as those presented for the extended polar cap model of Daugherty & Harding (1995). The model seems to work best for the oldest of the gamma-ray pulsars, which suggests that we have neglected an effect which may be important in the case of high rotational speeds. This may be related to the pair creation process which generates the charges that produce the gamma-rays.

The fact that our model has some success with older pulsars suggests that it may work well for predictions of new gamma-ray pulsars from the radio pulsar population, as these candidate pulsars are generally quite old with low luminosity. To build a convincing list of candidates, however, requires a well-defined total power output from the model pulsars, which is not yet available either on theoretical grounds or through a fit to the data.

When the model does not work (in the case of very young, fast pulsars), it generates too much of its power in the form of very high-energy photons, and the spectra are too hard. A process which scatters these high-energy photons to lower energies seems to be required; however, the scattering processes which are expected to work in the outer magnetosphere are generally less efficient as the photon energy increases (Compton scattering and photon-photon scattering).

Our model also has the potential to generate more complex light curves than either the outer gap or polar cap models, which can only produce single or double peaks. However, this is something of a double-edged sword, as a random sample of light curves would be somewhat less regular than is observed. In addition, the observed light curves are generally only singly or doubly peaked. This may be something of a selection effect, and some of the unidentified EGRET sources may be pulsars with complex light curves.

An appropriate testing ground for this theory, as well as the other gamma-ray pulsar

theories, is the group of millisecond pulsars. Since their fields are several orders of magnitude less than the observed gamma-ray pulsars (members of the regular pulsar population), and their angular velocities can be an order of magnitude larger than the gamma-ray pulsars, they probe a very different region of parameter space. Our model predicts that these objects can be gamma-ray emitters, unlike some other gamma-ray pulsar models. However, since these are very rapidly spinning objects, the effects that make our model spectra incorrect for the young gamma-ray pulsars may also make simulating the millisecond pulsar gamma-ray emission difficult.

This work has been submitted for publication as a pair of papers, Higgins & Henriksen (1996a), Higgins & Henriksen (1996b).

A technique to differentiate the outer gap models (to which our model is closest kin) from the polar cap models was also presented. Vacuum birefringence, an effect that causes a phase lag in photons travelling through powerfully magnetic fields with different orientations of their polarisation vector, will ensure that gamma-rays emitted from regions near the star (as with polar cap models) will *not* have any significant degree of bulk polarisation. Present gamma-ray detectors cannot measure photon polarisation, but the next generation of these telescopes may have this ability. A detection of significant polarisation in the pulsar gamma-ray spectra will effectively rule out the whole class of polar cap models.

## APPENDIX

## A. THE DEUTSCH FIELDS

The electromagnetic fields used for those around the pulsar in this work are the fields derived by Deutsch (1955) for a rigidly rotating, highly conducting and magnetic sphere in vacuum.

The internal fields are assumed to be frozen-in inside the star, since its conductivity is taken to be very large. In the limit that the radius  $a$  of the star is much less than the light cylinder radius  $R_{lc}$ , the electric and magnetic fields outside the star are given by:

$$E_r = -\frac{\mu a^2}{2r^2 R_{lc}} \left[ \frac{\cos \chi (3 \cos(2\theta) + 1)}{r^2} + \left( \frac{3}{r^2} - \frac{1}{R_{lc}^2} \right) \sin \chi \sin(2\theta) \cos \lambda + \frac{\sin \chi \sin(2\theta) \sin \lambda}{r R_{lc}} \right]$$

$$E_\theta = \frac{\mu}{R_{lc}} \left[ -\frac{a^2}{r^4} \cos \chi \sin(2\theta) + \left( \frac{a^2}{r^4} \left( -\frac{r^2}{2R_{lc}^2} + 1 \right) \cos(2\theta) - \frac{1}{r^2} \right) \sin \chi \cos \lambda \right. \\ \left. - \left( \frac{a^2}{r^3 R_{lc}} \left( \frac{r^2}{6R_{lc}^2} - 1 \right) \cos(2\theta) + \frac{1}{r R_{lc}} \right) \sin \chi \sin \lambda \right]$$

$$E_\phi = -\frac{\mu \sin \chi \cos \theta}{R_{lc}} \left[ \left( \frac{a^2}{r^3 R_{lc}} \left( \frac{r^2}{6R_{lc}^2} - 1 \right) + \frac{1}{r R_{lc}} \right) \cos \lambda + \left( \frac{a^2}{r^4} \left( -\frac{r^2}{2R_{lc}^2} + 1 \right) - \frac{1}{r^2} \right) \sin \lambda \right]$$

$$B_r = \frac{\mu}{r^2} \left[ \frac{2}{r} \cos \chi \cos \theta + \frac{2}{R_{lc}} \sin \chi \sin \theta \sin \lambda + \frac{2}{r} \sin \chi \sin \theta \cos \lambda \right]$$

$$B_\theta = \frac{\mu}{r} \left[ \frac{1}{r^2} \cos \chi \sin \theta + \frac{1}{R_{lc}^2} \left( 1 - \frac{R_{lc}^2}{r^2} \right) \sin \chi \cos \theta \cos \lambda - \frac{1}{r R_{lc}} \sin \chi \cos \theta \sin \lambda \right]$$

$$B_\phi = -\frac{\mu}{r R_{lc}^2} \left[ \left( 1 - \frac{R_{lc}^2}{r^2} \right) \sin \chi \sin \lambda + \frac{R_{lc}}{r} \sin \chi \cos \lambda \right]$$

The coordinate system used is the regular spherical coordinates, with  $\theta$  measured from the rotation axis.  $\chi$  is the angle between the rotation axis and the effective magnetic dipole moment  $\mu$ .

Far from the star these fields reduce to those of a point dipole spinning in vacuum, and most of the physics can be explained in terms of these simpler fields. However, since our model effectively extends the stellar radius to  $0.1R_{\text{ic}}$  by assuming an inner magnetosphere of frozen-in plasma, the boundary conditions at the edge of this corotating region can become important to the details of the radiation pattern.



## BIBLIOGRAPHY

- [1] Alexandreas, D.E., *et al*, 1994, ApJ, 426, L1.
- [2] Babul, A., Paczyński, B, Spergel, D., 1987, ApJ, 316, L49.
- [3] Band, D.L., *et al*, 1995, ApJ, 447, 289.
- [4] Barat, C., *et al*, 1979, A&A, 79, L24.
- [5] Barat, C., *et al*, 1991, Planet. Sp. Sci., 39, 67.
- [6] Barthelmy, S.D., *et al*, 1995, Astrop & Sp Sci, 231, 235.
- [7] Becker, W., Trumper, J., 1993, Nature, 365, 528.
- [8] Beskin, V.S., Gurevich, A.V., Istomin, Ya. N., 1993, *Physics of the Pulsar Magnetosphere*, Cambridge University Press.
- [9] Bhatia, V.S., Mishra, S., Panchapakesan, N., 1995, Supp. to J. Astrophys. Astr., 16, 235.
- [10] Boër, M., *et al*, 1993, A&A, 277, 503.
- [11] Bontekoe, T.R., Winkler, C., Stacy, J.G., Jackson, P.D., 1995, Astrop & Sp Sci, 231, 285.
- [12] Briggs, M.S., 1993, ApJ, 407, 126.
- [13] Briggs, M.S., *et al*, 1996, ApJ, 459, 40.
- [14] Cheng, K.S., Ho, C., Ruderman, M., 1988a, ApJ, 300, 500.

- [15] Cheng, K.S., Ho, C., Ruderman, M., 1988b, *ApJ*, 300, 522.
- [16] Chiang, J., Romani, R.W., 1994, *ApJ*, 436, 754.
- [17] Clark, G., *et al*, 1990, *ApJ*, 353, 274.
- [18] Clarke, T.E., Blaes, O., Tremaine, S., 1994, *AJ*, 107, 1873.
- [19] Colgate, S.A., Petschek, A.G., 1981, *ApJ*, 248, 771.
- [20] Connaughton, V., *et al*, 1994, *Gamma-Ray Bursts*, eds. G.J. Fishman *et al*, AIP 307, 470.
- [21] da Costa, A.A., Kahn, F.D., 1982, *MNRAS*, 199, 211.
- [22] Daugherty, J.K., Harding, A.K., 1986, *ApJ*, 309, 362.
- [23] Daugherty, J.K., Harding, A.K., 1991, *ApJ*, 374, 687.
- [24] Daugherty, J.K., Harding, A.K., 1996, *ApJ*, 458, 278.
- [25] DeMuth, D.M., *et al*, 1994, *Gamma-Ray Bursts*, eds. G.J. Fishman *et al*, AIP 307, 475.
- [26] Deutsch, A.J., 1955, *Annales d'Astrophysique*, 18, 18<sup>e</sup> Année, No. 1., 1.
- [27] Dumora, D., *et al*, 1996, *Čherenkov Low Energy Sampling & Timing Experiment - CELESTE experimental proposal*, Draft version 1.5.
- [28] Duncan, R.C., Li, H., Thompson, C., 1993, in *Compton Gamma-Ray Observatory*, AIP Conf. Proc. No. 280, ed. M. Friedlander, N. Gehrels, and D.J. Macomb (New York, AIP), p.1074.
- [29] Fenimore, E.E., Klebesadel, R.W., Laros, J.G., 1996, *ApJ*, 460, 964.
- [30] Fierro, J.M., *et al*, 1993, *ApJ*, 413, L27.
- [31] Frail, D.A., Kassim, N.E., Weiler, K.W., 1994, *AJ*, 107, 1120.

- [32] Frail, D.A., *et al*, 1994, ApJ, 437, L43.
- [33] Geppert, U., Wiebicke, H.-J., 1991, A&AS, 87, 217.
- [34] Goldreich, P., Julian, W.H., 1969, ApJ, 157, 869.
- [35] Gould, A., 1992, ApJ, 386, L5.
- [36] Greiner, J., *et al*, 1995, NATO ASI C450, *The Lives of the neutron stars*, eds. M.A. Alpar *et al*, Kluwer Acad. Pub., p. 519.
- [37] Greiner, J., *et al*, 1996, A&A, in press.
- [38] Grenier, I.A., Hermsen, W., Henriksen, R.N., 1993, A&A, 269, 209.
- [39] Gunji, S., *et al*, 1994, ApJ, 428, 284.
- [40] Harwit, M., Salpeter, E.E., 1973, ApJ, 186, L37.
- [41] Hartmann, D. Blumenthal, G.R., 1989, ApJ, 342, 521.
- [42] Higgins, M.G., Henriksen, R.N., 1995, *Astrop. & Sp. Sci.*, 231, 419.
- [43] Higgins, M.G., Henriksen, R.N., 1996a, MNRAS, submitted.
- [44] Higgins, M.G., Henriksen, R.N., 1996b, in preparation.
- [45] Hurley, K.A., *et al*, 1994, ApJ, 431, L13.
- [46] Hurley, K.C., *et al*, 1995, ApJ, 445, 348.
- [47] Hurley, K.C., *et al*, 1996, ApJ, 464, 342.
- [48] Jackson, J.D., 1975, *Classical Electrodynamics*, John Wiley & Sons.
- [49] Johnston, S., 1994, MNRAS, 268, 595.
- [50] Kanbach, G., *et al*, 1994, A&A, 289, 855.

- [51] Koranyi, D.M., *et al*, 1994, MNRAS, 271, 51.
- [52] Kulesa, A.S., Lynden-Bell, D., 1992, MNRAS, 255, 105.
- [53] Lamb, D.Q., 1995, PASP, 107, 1152.
- [54] Laurent, P.J., *et al*, 1994, A&A, 286, 838.
- [55] Li, H., Dermer, C., 1992, Nature, 359, 514.
- [56] Lieu, R., Axford, W.I., 1993, ApJ, 416, 700.
- [57] Lieu, R., Axford, W.I., 1995, ApJ, 447, 302.
- [58] LoSecco, J.M., 1994, ApJ, 425, 217.
- [59] Lund, N., 1995, Astrop & Sp Sci, 231, 217.
- [60] Lyne, A.G., Lorimer, D.R., 1994, 1994, Nature, 369, 127.
- [61] Manchester, R.N., Taylor, J.H., 1977, *Pulsars*, San Francisco: W.H. Freeman.
- [62] Maoz, E., 1993, ApJ, 414, 877.
- [63] Masnou, J.L., *et al*, 1994, A&A, 290, 503.
- [64] Mastichiadis, A., 1991, MNRAS, 253, 235.
- [65] Matz, S.M., *et al*, 1996, Third Huntsville GRB Workshop, ed C. Kouveliotou, M.S. Briggs, & G. Fishman, in press.
- [66] Mayer-Hasselwander, H.A., *et al*, 1994, ApJ, 421, 276.
- [67] Mazets, E.P., *et al*, 1981, Nature, 290, 378.
- [68] McNamara, B.J., *et al*, 1995, Astrop & Sp Sci, 231, 251.

- [69] Mészáros, P., 1992, *High Energy Radiation from Magnetised Neutron Stars*, University of Chicago Press.
- [70] Mészáros, P., Mészáros, A., 1995, *ApJ*, 449, 9.
- [71] Miller, G.S., Epstein, R.I., Nolta, J.P., Fenimore, E.E., 1991, *Phys Rev Ltrs*, 66, 1395.
- [72] Mitrofanov, I.G., 1990, *Astro & Sp Sci*, 165, 137.
- [73] Mitrofanov, I.G., Sagdeev, R.Z., 1990, *Nature*, 344, 313.
- [74] Murakami, T., *et al*, 1988, *Nature*, 335, 234.
- [75] Newman, M.J., Cox, A.N., 1980, *ApJ*, 242, 319.
- [76] Nolan, P.L., *et al*, 1993, *ApJ*, 409, 697.
- [77] Nolan, P.L., *et al*, 1996, *A&A*, in print.
- [78] Novick, R., *et al*, 1977, *ApJ*, 215, L117.
- [79] Ostriker, J.P, Gunn, J.E., 1969, *ApJ*, 157, 1395.
- [80] Ostrowski, M., Zdziarski, A.A., 1995, *Astrop & Sp Sci*, 231, 339.
- [81] Palmer, D.M., *et al*, 1995, *Astrop & Sp Sci*, 231, 315.
- [82] Paczyński, B., 1986, *ApJ*, 308, L43.
- [83] Paczyński, B., 1990, *ApJ*, 348, 485.
- [84] Paczyński, B., 1995, *PASP*, 107, 1167.
- [85] Peebles, P.J.E., 1993, *Principles of Physical Cosmology*, Princeton University Press, p 216.
- [86] Petrosian, V., Lee, T.T., 1996, *ApJL*, in print.

- [87] Pineault, S., Duquet, J.-R., 1993, MNRAS, 261, 246.
- [88] Pineault, S., Poisson, E., 1989, ApJ, 347, 1141.
- [89] Podsiadlowski, Ph., Rees, M.J., Ruderman, M., 1995, MNRAS, 273, 755.
- [90] Preece, R.D., Harding, A.K., 1992, ApJ, 386, 308.
- [91] Radhakrishnan, V., Cocke, D.J., 1969, *Astrop. Ltrs*, 3, 225.
- [92] Ramamamurthy, P.V., *et al*, 1995, ApJ, 447, L109.
- [93] Ramanamurthy *et al*, 1996, ApJ, in preparation.
- [94] Rankin, J.M., 1990, ApJ, 352, 247.
- [95] Robertson, H.P., Noonan, T.W., 1968, *Relativity and Cosmology*, W.B. Saunders Company.
- [96] Ruderman, M., Cheng, A., 1988, ApJ, 335, 306.
- [97] Schaefer, B.E., *et al*, 1987, ApJ, 313, 226.
- [98] Scharlemann, E.T., Arons, J., Fawley, W.M., 1978, ApJ, 222, 297.
- [99] Schmidt, M., 1968, ApJ, 151, 393.
- [100] Schmidt, M., Higdon, J.C., Huter, G., 1988, ApJ, 329, L85.
- [101] Shklovskii, I.S., 1974, *Soviet Astr.*, 18, 390.
- [102] Shrader, C.R., Gehrels, N., 1995, PASP, 107, 606.
- [103] Smith, A.G.K., *et al*, 1995, *Astrop & Sp Sci*, 231, 319.
- [104] Stanek, K.Z, Paczyński, B., Goodman, J., 1993, ApJ, 413, L7.
- [105] Stecker, F.W., De Jager, O.C., 1992, ApJ, 390, L49.

- [106] Stern, S.A., 1990, PASP, 102, 793.
- [107] Sturmer, S.J., 1995, ApJ, 446, 292.
- [108] Sturmer, S.J., Dermer, C.D., 1994, A&A, 281, L101.
- [109] Sturmer, S.J., Dermer, C.D., Michel, F.C., 1995, ApJ, 445, 736.
- [110] Taylor, J.H., Cordes, J.M., 1993, ApJ, 441, 674.
- [111] Taylor, J.H., Manchester, R.N., Lyne, A.G., 1993, ApJS, 88, 529.
- [112] Thompson, D.J., *et al*, 1992, Nature, 359, 615.
- [113] Thompson, D.J., *et al*, 1994, ApJ, 436, 229.
- [114] Thompson, D.J., *et al*, 1995a, in preparation.
- [115] Thompson, D.J.; *et al*, 1995b, ApJS, 101, 259.
- [116] Tsai, W., Erber, T., 1975, Phys. Rev. D, 12, 1132.
- [117] Ulmer, M.P., *et al*, 1995, ApJ, 448, 356.
- [118] Vanderspek, R.K., Krimm, H.A., Ricker, G.R., 1995, Astrop & Sp Sci, 231, 259.
- [119] Verbunt, F., *et al*, 1996, A&A, 311, L9.
- [120] Vernetto, S., *et al*, 1995, Astropart. Physics, Vol 3, Issue 4, 311.
- [121] Watson, G.S., 1956, Geophys. Suppl. MNRAS, 7, 160.
- [122] Watson, G.S., 1983, Statistics on Spheres (New York:Wiley).
- [123] Yoshida, A., *et al*, 1991, PASP, 43, L69.
- [124] Zampieri, L., Turolla, R., Zane, S., Treves, A., 1995, ApJ, 439, 849.